



Università degli Studi di Salerno
Facoltà di Scienze Matematiche Fisiche e Naturali

Philosophiæ Doctor Thesis
in
Chemistry

A Molecular Dynamics View of Structure and Reactivity

Supervisor

Prof. Dr. Luigi Cavallo

Co-supervisors

Dr. Giuseppe Milano

Dr. Marcella Iannuzzi

Candidate

Francesco Ragone

Anno Accademico 2009-2010

Suum cuique tribuere
(*Ulpiano – Digesta giustinianei*)

Table of Contents

List of Publications	v
Introduction	1
Objectives	7
1 Theoretical Background	9
1.1 Molecular Dynamics – A brief overview	10
1.1.1 Integration methods	12
1.1.2 Ensembles	14
1.2 <i>ab initio</i> molecular dynamics	15
1.2.1 The Born–Oppenheimer approximation	16
1.2.2 Density Functional Theory – The basics	19
1.2.3 Basis set expansions	21
1.3 Classical MD	27
1.3.1 Force field in formulas	29
1.3.2 Non–bonding interactions	30
1.3.3 Electrostatic term	31
1.4 What about Reactions?	32
1.5 Programs	34
1.5.1 CP2K	34
1.5.2 Gromacs	34

2	AIMD & Metathesis	37
2.1	Metathesis	38
2.1.1	Historical background	40
2.1.2	The Chauvin mechanism	42
2.2	N-heterocyclic Carbenes	44
2.2.1	NHCs in Organometallic Chemistry	45
2.3	Steric Parameter – % V_{Bur}	47
2.3.1	Web Application Implementation	49
2.4	Flexibility of NHCs	52
2.4.1	Computational details – Static calculations	52
2.4.2	Computational details – Dynamic calculations	53
2.4.3	Static analysis	53
2.4.4	Dynamics analysis	55
2.4.5	Buried volume analysis	59
2.4.6	Analysis of free NHCs	65
2.4.7	Summary	67
2.5	Deactivation of NHC bearing Ru Catalysts by Lewis acids	69
2.5.1	Computational details – Static calculations	70
2.5.2	Computational details – Dynamic calculations	72
2.5.3	Results	72
2.5.4	Results and Discussion	75
2.5.5	Summary	81
3	Gold NP/Polymer Interfaces	83
3.1	The “Experimental system”	86
3.1.1	Synthesis	87
3.1.2	Testing & Performances	87
3.2	Coarse-grained Approach	90
3.2.1	Mesoscale Models for Vinyl Polymers	91
3.2.2	Mesoscale Potentials and Force Field Parametrization	93
3.2.3	Reverse mapping	93
3.3	Simulations Strategy and Initial Configurations Setup	96
3.3.1	Simulation Details	98

3.4	Results & Discussion	99
3.4.1	Polymer Chains and 8-HQ diffusion	99
3.4.2	Radial Density Profiles	100
3.4.3	Polymer Chain Dimension	106
3.4.4	Orientation of 8-HQ molecules	107
3.5	Summary	111
	Conclusions	113
	References	115

List of Publications

“Mechanistic Insights on the Cis-Trans Isomerization of Ruthenium Complexes Relevant to Olefin Metathesis Catalysts” Poater, A.; Ragone, F.; Correa, A.; Szadkowska, A.; Barbasiewicz, M.; Grela, K.; Cavallo, L. *Chemistry: A European Journal*, **2010**, In press;

“Comparing the Enantioselective Power of Steric and Electrostatic Effects in Transition Metals Catalyzed Asymmetric Synthesis” Poater, A.; Ragone, F.; Mariz, R.; Dorta, R.; Cavallo, L. *Chemistry: A European Journal*, **2010**, In press;

“Flexibility of N-heterocyclic carbene ligands in ruthenium complexes relevant to olefin metathesis and their impact in the first coordination sphere of the metal” Ragone, F.; Poater, A.; Cavallo, L. *Journal of the American Chemical Society*, **2010**, 132, 4249-4258.

“A Comparison of the Performance of the Semiempirical PM6 Method Versus DFT Methods in Ru-Catalyzed Olefin Metathesis” Correa, A.; Poater, A.; Ragone, F.; Cavallo, L. *Green Metathesis Chemistry; NATO Science for Peace and Security Series A: Chemistry and Biology; Springer Netherlands: Dordrecht*, **2010**; pp. 281-292.

“Exploring the reactivity of Ru-based metathesis catalysts with a pi-acid ligand trans to the Ru-ylidene bond” Poater, A.; Ragone, F.; Correa, A.; Cavallo, L. *Journal of the American Chemical Society*, **2009**, 131, 9000-9006.

“SambVca: A Web Application for the Calculation of the Buried Volume of N-Heterocyclic Carbene Ligands” Poater, A.; Cosenza, B.; Correa, A.; Giudice, S.; Ragone, F.; Scarano, V.; Cavallo, L. *European Journal of Inorganic Chemistry*,

2009, 1759-1766.

“Thermodynamics of N-Heterocyclic Carbene Dimerization: The Balance of Sterics and Electronics” Poater, A.; Ragone, F.; Giudice, S.; Costabile, C.; Dorta, R.; Nolan, S. P.; Cavallo, L. *Organometallics*, **2008**, 27, 2679-2681.

Introduction

The field of computer simulations has developed into a very important branch of science, which on the one hand helps theorists and experimentalists to go beyond their inherent limitations and on the other hand is a scientific field on its own. Therefore, simulation science has often been called the third pillar of science, complementing theory and experiment.

Modern theoretical methodology, aided not only by the advent of high speed computing but also by the impressive efforts in massive parallel processing, are enabling direct calculation of mechanical properties of novel materials, dynamics of reaction processes on surfaces and in aqueous solution, the conformational sampling of crucial parts of biomolecular landscapes, and more. This makes computer science somehow eclectic, *i.e.* it draws upon multiple theories, instead to be hold just to one paradigm or a set of assumptions and allows a net gain of complementary insights into a subject.

Computer simulations connect microscopic length and time scales of the *in silico* experiments to the macroscopic world of the laboratory: theoreticians could provide a guess at the interactions between molecules, and obtain predictions of properties as accurate as required, subject to the limitations imposed by the computer power (and budget) and of the chosen and feasible theory level.

The link between theories and experiments is profitable even in another standpoint: a theory could be tested by conducting a simulation and comparing with experimental results at “normal” conditions; afterwards, if the model works, it is also possible to guess the behaviour of the systems at severe conditions, carrying out simulations in conditions that are difficult or impossible in the laboratory, *i.e.* at extremes of temperature or pressure.

When a desired property of a material can be connected to quantities on the atomic or molecular scale, quantum chemistry could be a useful tool in the process of improving such materials. Typical examples are dyes and pigments, for which color and brilliance depend on the energies and nature of electronic excitations. Organic dyes typically have delocalized π -systems and functional groups chosen appropriately to tune the optical properties.

The up to date computational power allow to treat even very big molecule (in

the order of $\sim 10^2$ atoms) with the desired accuracy to calculate the excited states and not just with semi-empirical methods used until few years ago. It has to point out that quantum chemical methods are predominantly applied to isolated molecules, which corresponds to the state of an ideal gas. Most chemical processes, however, take place in condensed phase, and the interaction of a molecule with its environment. By the way, solvent molecules can directly interact with the reacting species, *e.g.* by coordination to a metal center or by formation of hydrogen bonds. In such cases it is necessary to explicitly include solvent molecules in the calculation. Depending on the size of the solvent molecules and their number needed to get the calculated properties converged, the overall size of the molecular system and the resulting computational effort can significantly be increased. Currently, only semi-empirical and classical molecular mechanics methods are able to handle several hundred atoms and to follow them for a “long-enough” time, but the developments towards linear scaling approaches in DFT are very promising. An alternative could be a mixed quantum mechanical (QM) and molecular mechanical (MM) treatment, that give the QM/MM method.

Nevertheless, if there are no specific solute-solvent interactions, the main effect of the solvent is electrostatic screening, depending on its dielectric constant. This can be described very efficiently by continuum solvation models, like polarizable continuum model (PCM) implemented in the Gaussian suite program.

Theoretical excursus

The traditional simulation methods for many-body systems can be divided into two main classes:

- stochastic simulations, which are largely represented by the Monte Carlo (MC) method;
- molecular dynamics (MD) method.

MC simulations probe the configuration space by trial moves of particles. The so-called Metropolis algorithm uses the energy change from step n to $n+1$ as a trigger to accept or reject a new generated configuration. Paths towards lower energy are always accepted, those to higher energy are accepted with a probability governed by Boltzmann statistics. This algorithm ensures that the correct limiting distribution and properties of a given system can be calculated by averaging over all MC moves within a given statistical ensemble (where one move means that every degree of freedom is probed once on average) – no other details will be give in this thesis.

MD methods, instead, are governed by the system Hamiltonian and consequently Newton's or more frequently Hamilton's or Lagrangian's equations of motion are solved numerically, to move particles to new positions and to assign new velocities at these new positions, starting from a pre-specified initial state and subject to a set of boundary conditions appropriate to the problem. This is an advantage of MD simulations with respect to MC, since not only the configuration space is probed but the whole phase space, which gives additional information about the dynamics of the system.

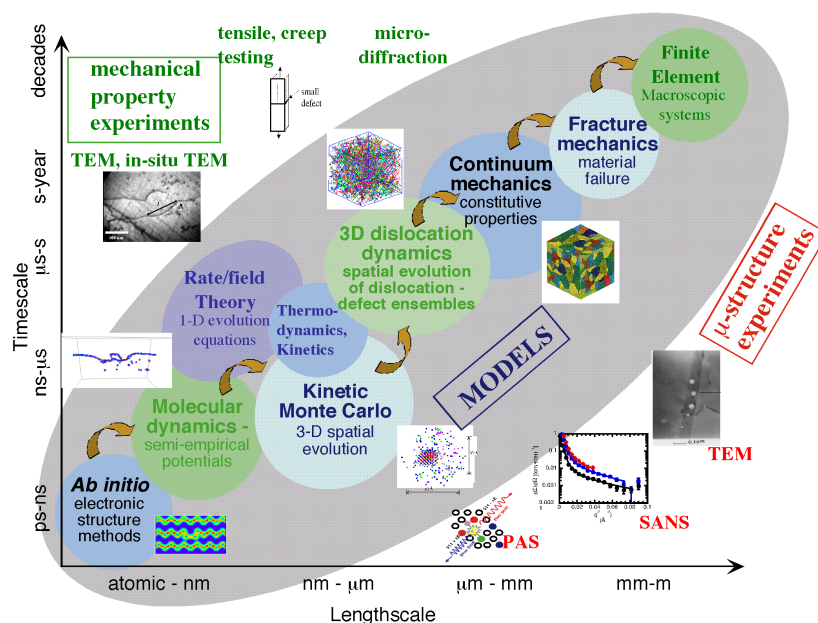
Both methods are complementary in nature but they lead to the same averages of statistic quantities, given that the system under consideration is ergodic and the same statistical ensemble is used. MD methodology allows both equilibrium thermodynamic and dynamical properties of a system at finite temperature to be computed, while simultaneously providing a "window" onto the microscopic motion of individual atoms (or superatoms, see later) in the system.

In order to characterise a given system and to simulate its complex behavior, a model for interactions between system constituents is required. This model has to be tested against experimental results, *i.e.* it should reproduce or approximate experimental findings like distribution functions or phase diagrams, and theoretical constraints, *i.e.* it should obey certain fundamental or limiting laws like energy or momentum conservation. If the simulation results differ from real system properties or if they are incompatible with solid theoretical manifestations, the model has to be refined. This procedure can be understood as an adaptive refinement which leads at the end to an approximation of a model of the real world at least for certain properties. The model itself may be constructed from plausible considerations, result from first principle *ab initio* calculations. Although the electronic distribution of the particles is calculated very accurately, this type of model building contains also some approximations, since many-body interactions are mostly neglected (this would increase the parameter space in the model calculation enormously). However, it often provides a good starting point for a realistic model.

One of the most challenging aspects of an MD calculation is the specification of the forces. In many applications, these are computed from an empirical model or *force field*, in which simple mathematical forms are employed to describe bond, bend and dihedral angle potentials as well as van der Waals and electrostatic interactions between atoms; the model is parametrized by fitting to experimental data or high level *ab initio* calculations on small clusters or fragments. This approach has enjoyed tremendous success in the treatment of systems ranging from simple liquids and solids to polymers and biological systems such as proteins and nucleic acids.

Computational techniques span in the whole realm of molecular sciences, covering much of those parts of physics, chemistry and biology that deal with

molecules, are well established in terms of extremely powerful but highly specialized approaches. An important issue of simulation studies is the accessible time- and length-scale which can be covered by microscopic simulations. Scheme 0.1 shows a schematic representation for different types of simulations. It is clear that the more detailed a simulation technique operates, the smaller is the accessibility of long times and large length scales. The challenge is to push up the timescale of simulation and the sizes of systems treated, while not sacrificing essential features of the molecular landscape. The field of *ab initio*



Scheme 0.1

molecular dynamics (AIMD), in which finite temperature MD trajectories are generated with forces obtained from accurate “on-the-fly” electronic structure calculations, is a rapidly evolving and growing technology that allows chemical processes in condensed phases to be studied in an accurate and unbiased way. *Ab initio* molecular dynamics revolutionized the field of realistic computer simulation of complex molecular systems and processes, including chemical reactions, by unifying molecular dynamics and electronic structure theory. Quantum simulations, where electronic fluctuations are taken into account, allow to study very short time and length scales which are typically in the order of $\sim 10^1 \text{ \AA}$ and 10^2 ps .

Classical molecular dynamics approximates electronic distributions in a rather “coarse-grained” fashion by putting either fixed partial charges on interaction sites or by adding an approximate model for polarization effects. In both cases,

the time scale of the system is not dominated by the motion of electrons, instead by the time of intermolecular collision events, rotational motions or intramolecular vibrations, which are orders of magnitude slower than those of electron motions. Consequently, the time step of integration is larger and trajectory lengths are of order $\sim 10^2$ ns and accessible lengths of order 10–100 nm.

“Coarser” grained models have proven quite useful for obtaining data on the behavior of systems where the relevant time or length scales (or both) are inaccessible to all-atom MD. However, even heavier use of Coarse grained (CG) simulations could be made if coarse graining could be used as an accelerator, with atomic detail either maintained in regions of interest or recoverable from snapshots in the CG trajectory. Recent progress has been made along both these fronts recently, in the form of mixed CG-all atom simulations and simulations involving dynamic switching of components between CG and all-atom descriptions.

For further information, on MD techniques see Section 1.5.2

Theory in practice

Many of the industrial chemical processes involve catalysts and most of them are in the solid state (heterogeneous catalysis), but, with the extensive developments in organometallic chemistry in the last decades, catalytic processes in the liquid phase become more and more important (homogeneous catalysis) – even to understand some results of heterogeneous catalyst. For the development of a catalyst, besides economic and environmental considerations, three issues are of central importance:

- Activity: The catalyst must be efficient (high turnover numbers).
- Selectivity: By-products should be avoided.
- Stability: Deactivation or decomposition of the catalyst must be slow.

To improve a catalyst with respect to these criteria, a detailed insights of the reaction pathways and/or behaviour of the catalyst itself is mandatory: in this field, quantum chemical methods can be of enormous value, since the experimental investigation of steps in a complicated mechanism is rather difficult. Once the crucial parameters are found, new guesses for better performing catalysts can be deduced and immediately be tested in the calculations. Thus, when theory is used for a rough screening and only the most promising candidates have to be tested in experiments, the development process for new catalysts can

be shortened significantly. DFT is used almost exclusively for both homogeneous and heterogeneous applications. In the latter case, solids are treated with periodic boundary conditions or QM/MM approaches.

Two examples about the use of *ab initio* molecular dynamics applied to the study of catalytic behaviour will be given in Section 2.4 and in Section 2.5, where, respectively, the flexibility of N-heterocyclic carbenes, a class of very important ligands, and the deactivation pathways of the same kind by π -donor molecules will be treated.



Chart 0.1

However as depicted above, the design of chemical catalytic processes and the study of structures of materials are intrinsically two different scale (in time and in length) problems. For this reason, a CG-all atom treatment example applied to hybrid polymer-gold nanoparticle system will be explained in Chapter 3.

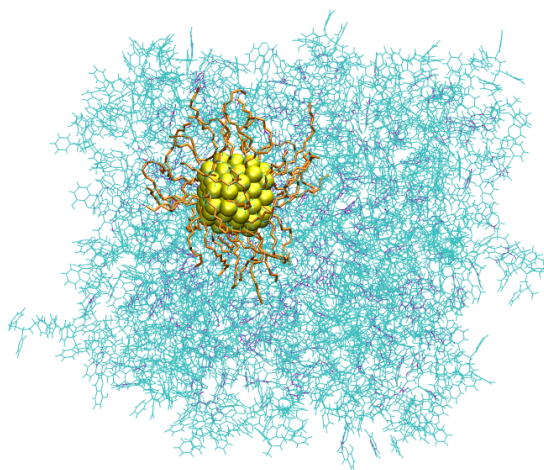


Figure 1: Snapshot of the system presented in Chapter 3.

For the sake of simplicity, every chapter has its own structures numbering.

Objectives

The main aim of this Ph.D. project is to understand and apply dynamic computational methods & tools to study reactivity and structural problems, in particular for the issues listed below.

- Chapter 2 is focused on the metathesis of alkenes, catalyzed by Ruthenium complexes; in particular, two different argumentation are pursued:
 - (a) In Section 2.4, the flexibility of N-heterocyclic carbene ligands in Ru complexes of the general formula $(\text{NHC})\text{Cl}_2\text{Ru}=\text{CH}_2$, as a key feature that allows NHCs to modulate their encumbrance around the metal. This is fundamental to the rational design of more active and, in the broadest sense, better performing new catalysts.
 - (b) In Section 2.5 one pathways for the deactivation of this kind of catalysts induced by coordination of a CO molecule trans olefin metathesis catalyst bearing the NHC ligand SIMes is investigated.
- In Chapter 3, a Coarse-grain/all atom approach is used to achieve information about the interface between gold nanoparticles and a polymer matrix. Specifically, for the relevance of these systems in organic memory technology, the attention is focused on programmable devices made of polystyrene containing gold nanoparticles and 8-hydroxyquinoline. A characterization at molecular level of the interface can help to understand the behavior of this class of devices.

Chapter 1

Theoretical Background

Computer modeling and simulation are widely accepted as a tool that can help to generate new scientific understandings on effective design of catalysts and nanomaterials on molecular scale, to study properties of them and of biological systems and so on. Most important is the possibility to do feasibility tests of a synthesis, rationalize experimental results, and even more, that allow gains in terms of human time, money (saving on reagents, solvent and disposals) and environmental care.

At the beginning of the latest Century, experiments like black body radiation, photovoltaic effect, low temperature thermal capability, and photons let the Classical Physics in crisis; till that moment it was able to rationalize all the experimental observables: contemporaneously quantum mechanics born. This “recent” science has a lot of applications resolving chemical problems in particular regarding the reactivity.

By the way quantum mechanics, both for limitation on computational power and for equilibration issue is not the only way to describe those kinds of systems; indeed computational prediction of material properties is of great advantages in achieving rational and cost effective design: a reliable prediction is promoted by a systematic consideration of the intrinsic multiscale hierarchical structure. Most importantly, an effective integration of different methods and theories at individual scales offers unique opportunities for gaining in depth scientific understandings on the molecular structural origin of macroscopic property enhancement.

In general with the quantum chemistry it is possible to study the relative stability of molecules, characterize the species along reactive paths, the thermodynamics and the kinetic of the reactions, the bonds strengths, rationalize and

predict behaviour of some class of complexes, spectroscopic information, intra- and inter-molecular forces and more, while classical mechanics is better suited for non-interacting systems, biological macromolecules, materials, and any systems in which the electrons motion could be disregarded.

1.1 Molecular Dynamics – A brief overview

The first paper reporting a molecular dynamics simulation was written by Alder and Wainwright in 1957.[1] The purpose of the paper was to investigate the phase diagram of a hard sphere system, and in particular the solid and liquid regions. In a hard sphere system, particles interact via instantaneous collisions, and travel as free particles between collisions. More details could be find in a subsequent paper, published in 1959:[2]

“In order to follow the dynamics of a many-particle system with any sort of interaction potential, one could at any instant calculate the force on each particle by considering the influence of each of its neighbors. The trajectories could then be traced by allowing the particles to move under a constant force for a short-time interval and then by recalculating a new force to apply for the next short-time interval, and so on . . .”

with the hard sphere square well potential:

$$\begin{cases} V = \infty, & r < \sigma_1 \\ V = V_0, & \sigma_1 < r < \sigma_2 \\ V = 0, & r \end{cases} \quad (1.1)$$

in which r is the “*magnitude of the separation*” of the centers of a pair of molecule and σ_1 , σ_2 and V_0 are constants.

“The calculation can also be monitored by means of a cathode-ray tube which is attached to the computer and which form a picture of the system after each time step”

In fifty years both the hardware and the theoretical apparatus evolved drastically and a lot of problems can now be treated by computer simulation.

In general, the dynamics of molecular systems can be explored *in silico* with molecular dynamics simulation (MD), a method in which the equations of motion are solved in small time steps. In such simulations the size of the time step must be shorter than the shortest characteristic time scale in the system. Thus, many molecular dynamics steps must be carried out to explore the dynamics of a molecular system for times that are long compared with the basic time scale

of molecular vibrations. Depending on specific system and the available computer equipment, one can carry out from ten thousands to millions of such steps. There are many strategies that sometimes allow to use higher time step; a common strategy is to use a constraint algorithm, like SETTLE,[3] SHAKE (*e.g.* its extension like RATTLE)[4] and LINCS[5]. An alternative is the multiple time step method.

In molecular dynamics, atoms interact with each other. These interaction originate forces which act upon atoms, furthermore atoms move under the action of these instantaneous forces. As the atoms move, their relative positions change and forces change as well: this is in brief what happen many times in a molecular dynamics simulation.

A simulation is “safe” when the simulation time is much longer than the relaxation time of the quantities one is interested in. However, different properties have different relaxation times. The main ingredient of a simulation is a model for the physical system. For a molecular dynamics simulation this amounts to choosing the potential: a function $V(\mathbf{r}_1, \dots, \mathbf{r}_N)$ of the positions of the N nuclei, representing the potential energy of the system when the atoms are arranged in that specific configuration. This function is translationally and rotationally invariant, and is usually constructed from the relative positions of the atoms with respect to each other, rather than from the absolute positions. Forces are then derived as the gradients of the potential with respect to atomic displacements: $\mathbf{F}_i = -\nabla V(\mathbf{r}_1, \dots, \mathbf{r}_N)$ This form implies the presence of a conservation law of the total energy $E = K + V$, where K is the instantaneous kinetic energy.

The main issue remains how to obtain the right potential, to understand how it is related with the behavior of the real system, and the main question is if it is required a quantum mechanics approach or a classical treatment is enough. Classical mechanics works properly, even at coarser-grained level, for nanomaterials, liquids, ion pairs and similar. By the way, when a reaction occurs is mandatory to study the system with quantummechanics. Of course, the choice of the method is also strictly related to the number of particle necessary to study the system in exam.

In *ab initio* simulations, where interatomic forces are determined by solving the electronic structure problem (usually) “on the fly”, total simulation times typically do not exceed the order of 10^2 picoseconds. Longer simulations of nanosecond, or, in some rare cases, microsecond length can be achieved if forces are determined from computationally less expensive empirical force fields often used to simulate biological systems.

The realism of the simulation therefore depends on the ability of the potential chosen to reproduce the behavior of the material under the conditions at which the simulation is run.

After a brief foreword, in section 1.2 will be introduced the the *ab initio* molecular dynamics, subsequently in section 1.3 will be given an excursus on classical molecular dynamics.

1.1.1 Integration methods

The “engine” of a molecular dynamics program is its time integration algorithm, required to integrate the equation of motion of the interacting particles and follow their trajectory. Time integration algorithms are based on finite difference methods, where time is discretized on a finite grid, the time step Δt being the distance between consecutive points on the grid. Knowing the positions and some of their time derivatives at time t (the exact details depend on the type of algorithm), the integration scheme gives the same quantities at a later time $t + \Delta t$. By iterating the procedure, the time evolution of the system can be followed for long times.

Of course, these schemes are approximate and there are errors associated with them. In particular, one can distinguish between

- Truncation errors, related to the accuracy of the finite difference method with respect to the true solution. Finite difference methods are usually based on a Taylor expansion truncated at some term, hence the name. These errors do not depend on the implementation, they are intrinsic to the algorithm. In molecular dynamics simulation, generally, the Taylor expansion is truncated to the third term, since it has been observed that low order algorithm lack in accuracy, while higher order are too expensive.
- Round-off errors, related to errors associated to a particular implementation of the algorithm. For instance, to the finite number of digits used in computer arithmetic.

Of course, both errors can be reduced by decreasing Δt : for large Δt , truncation errors dominate, but they decrease quickly as Δt is decreased.

Two popular integration methods for MD calculations are the Verlet algorithm and predictor–corrector algorithms. In molecular dynamics, the most commonly used time integration algorithm is Verlet algorithm.[6, 7] The basic idea is to write two third–order Taylor expansions for the positions $\mathbf{r}(t)$, one forward and one backward in time:

$$\mathbf{r}(t + \Delta t) = \mathbf{r}(t) + \frac{d\mathbf{r}}{dt}\Delta t + \frac{1}{2}\frac{d^2\mathbf{r}}{dt^2}\Delta t^2 + \frac{1}{3!}\frac{d^3\mathbf{r}}{dt^3}\Delta t^3 + \mathcal{O}(\Delta t^4) \quad (1.2)$$

but

$$\frac{d\mathbf{r}}{dt} = \boldsymbol{\nu}(t), \quad \frac{d\mathbf{r}^2}{dt^2} = \mathbf{a}(t) = \frac{\mathbf{F}(t)}{m} = -\frac{1}{m}\nabla V[\mathbf{r}(t)] \quad (1.3)$$

where $\boldsymbol{\nu}(t)$ represents the velocities, \mathbf{a} for the accelerations, $\mathbf{F}(t)$ stands for the forces, m for the masses and $\nabla V[\mathbf{r}(t)]$ that is the gradient of the potential that depends on the positions. Said that it is possible to write:

$$\mathbf{r}(t + \Delta t) = \mathbf{r}(t) + \boldsymbol{\nu}(t)\Delta t + \frac{1}{2} \frac{\mathbf{F}(t)}{m} \Delta t^2 + \frac{1}{3!} \frac{d\mathbf{r}^3}{dt^3} \Delta t^3 + \mathcal{O}(\Delta t^4) \quad (1.4)$$

By the way it is also true that

$$\mathbf{r}(t - \Delta t) = \mathbf{r}(t) - \boldsymbol{\nu}\Delta t + \frac{1}{2} \frac{\mathbf{F}(t)}{m} \Delta t^2 - \frac{1}{3!} \frac{d\mathbf{r}^3}{dt^3} \Delta t^3 + \mathcal{O}(\Delta t^4) \quad (1.5)$$

Doing the sum of equations 1.4 and 1.5 it is possible to obtain

$$\mathbf{r}(t + \Delta t) + \mathbf{r}(t - \Delta t) = 2\mathbf{r}(t) + \frac{\mathbf{F}(t)}{m} \Delta t^2 + \mathcal{O}(\Delta t^4) \quad (1.6)$$

the truncation error of the algorithm when evolving the system by Δt is of the order of Δt^4 , and so

$$\mathbf{r}(t + \Delta t) \approx 2\mathbf{r}(t) - \mathbf{r}(t - \Delta t) + \frac{\mathbf{F}(t)}{m} \Delta t^2 \quad (1.7)$$

This algorithm is at the same time simple to implement, accurate and stable, explaining its large popularity among molecular dynamics simulators.

A problem with this version of the Verlet algorithm is that velocities are not directly generated. While they are not needed for the time evolution, their knowledge is sometimes necessary. Moreover, they are required to compute the kinetic energy K , whose evaluation is necessary to test the conservation of the total energy $E = K + V$. This is one of the most important tests to verify that a MD simulation is proceeding correctly. One could compute the velocities from the positions by using

$$\boldsymbol{\nu}(t) = \frac{\mathbf{r}(t + \Delta t) - \mathbf{r}(t - \Delta t)}{2\Delta t} \quad (1.8)$$

However, the error associated to this expression is of order $\Delta^2 t$. To overcome this difficulty, some variants of the Verlet algorithm have been developed. They give rise to exactly the same trajectory, and differ in what variables are stored in memory and at what times.

The leap-frog algorithm is one of such variants[8] where velocities are handled somehow better:

$$\boldsymbol{\nu}(t + \frac{\Delta t}{2}) = \frac{\mathbf{r}(t + \Delta t) - \mathbf{r}(t)}{\Delta t} \quad (1.9)$$

and so

$$\mathbf{r}(t + \Delta t) = \mathbf{r}(t) + \boldsymbol{\nu}(t + \frac{\Delta t}{2})\Delta t \quad (1.10)$$

An even better implementation of the same basic algorithm is the so-called velocity Verlet scheme, where positions, velocities and accelerations at time $t + \Delta t$ are obtained from the same quantities at time t in the following way:

$$\begin{aligned} \mathbf{r}(t + \Delta t) &= \mathbf{r}(t) + \boldsymbol{\nu}(t)\Delta t + \frac{1}{2} \frac{\mathbf{F}(t)}{m} \Delta t^2 \\ \boldsymbol{\nu}(t + \frac{\Delta t}{2}) &= \boldsymbol{\nu}(t) + \frac{1}{2} \frac{\mathbf{F}(t)}{m} \Delta t \\ \mathbf{F}(t + \Delta t) &= -\nabla V[\mathbf{r}(t + \Delta t)] \\ \boldsymbol{\nu}(t + \Delta t) &= \boldsymbol{\nu}(t + \frac{\Delta t}{2}) + \frac{1}{2} \frac{\mathbf{F}(t + \Delta t)}{m} \Delta t \end{aligned} \quad (1.11)$$

1.1.2 Ensembles

Most experimental observations are performed at constant number of particles (N) pressure (P) and temperature (T); sometimes at constant chemical potential μ , volume (V), and occasionally at constant N, V, T . Experiments at constant N, V, E are very rare, to say the least.

In the same way, a statistical ensemble has to be chosen even for *in silico* experiments, where thermodynamic quantities like pressure, temperature or the number of particles are controlled. The natural choice of an ensemble in MD simulations is the microcanonical ensemble NVE , since the system's Hamiltonian without external potentials is a conserved quantity. Nevertheless, there are extensions to the Hamiltonian which also allow to simulate different statistical ensembles. Several ensembles allow to obtain different thermodynamic quantities according to statistical mechanics.

In a computer simulation this theoretical condition is generally violated, due to limited accuracy in integrating the equations of motion showed before. This is, however, often not a too serious restriction, since correlation functions drop to zero on a much shorter time scale. Only for the case where long time correlations are expected one has to be very careful in generating trajectories.

The simplest extension to the NVE ensemble is the canonical ensemble, NVT , where the number of particles, the volume and the temperature are fixed to prescribed values. In order to control such variables, some external tricks are needed, like barostats and thermostats.

The temperature T , in contrast to N and V , is an intensive property. The extensive counterpart would be the kinetic energy of the system; several control

mechanism of this quantity are available: differential, proportional, stochastic and integral thermostats. It is evident that also within molecular dynamics the possibility of controlling the average temperature (as obtained from the average kinetic energy of the nuclei and the energy equipartition theorem) is welcome for physical reasons.

For the Constant–Pressure Constant–Enthalpy ensemble, *NPT*, in order to control the pressure, it is necessary to allow for volume variations in a molecular dynamics simulation cell. Keeping the pressure, P , constant is a desirable feature for many applications of molecular dynamics simulations. The concept of barostats and thus constant–pressure molecular dynamics was introduced in the framework of extended system dynamics by Hans Andersen.[9]

A simple picture for a constant pressure system is a box, with the walls of which are coupled to a piston which controls the pressure. In contrast to the case where the temperature is controlled, no coupling to the dynamics of the particles (timescales) is performed but the length scales of the system will be modified. Even in this case, several algorithms are described for a constant pressure ensemble. The conserved quantity will not be the system’s energy, since there will be an energy transfer to or from the external system, but the enthalpy H will be constant. In line with the constant temperature methods there are also differential, proportional, integral and stochastic methods to achieve a constant pressure situation in simulations.

1.2 *ab initio* molecular dynamics

The basic idea underlying every *ab initio* molecular dynamics method is to compute the forces acting on the nuclei from electronic structure calculations that are performed “on the fly” as the molecular dynamics trajectory is generated. *Ab initio* molecular dynamics unifies approximate *ab initio* electronic structure theory – *i.e.* solving Schrödinger’s wave equation numerically – and classical molecular dynamics, *i.e.* solving Newton’s equation of motion, or even with more elegant and useful Hamilton’s or Lagrange’s formalism.

With the improvement of both the methodology and the algorithms of density functional theory (DFT) in the last decades, new functionals with improved description of non–uniform electron distributions in molecules or on surfaces, paved the way for a qualitative or even quantitative quantum chemical treatment of a large variety of transition metal compounds and their reactions. When functionals without partial inclusion of Hartree–Fock (HF) exchange contributions are used, an approximate treatment of the Coulomb interaction of the electrons (density fitting, resolution of identity approach) allows for a very efficient

treatment of large systems. Therefore, with efficiently parallelized programs of this kind, it is routinely possible today to calculate the structure of molecules with the order of $\sim 10^2$ atoms.

Born–Oppenheimer (BO) molecular dynamics is a commonly used form of *ab initio* molecular dynamics simulations, in which the atomic coordinates are treated as classical coordinates, and the ions are propagated in time using classical equations of motion with the electronic ground state energy as the potential energy surface. This simple form of the equations of motion introduces a clear separation between the ionic propagation and electronic configuration as stated in the Born–Oppenheimer approximation.

1.2.1 The Born–Oppenheimer approximation

The non-relativistic Hamiltonian of a system of N nuclei described by coordinates $\mathbf{R}_1, \dots, \mathbf{R}_N \equiv \mathbf{R}$, momenta $\mathbf{P}_1, \dots, \mathbf{P}_N \equiv \mathbf{P}$, and masses M_1, \dots, M_N , and N_e electrons described by coordinates $\mathbf{r}_1, \dots, \mathbf{r}_{N_e}$, momenta $\mathbf{p}_1, \dots, \mathbf{p}_{N_e} \equiv \mathbf{p}$, and spin variables $s_1, \dots, s_{N_e} \equiv s$ – Nuclear spin is ignored in the present discussion – is given by

$$\begin{aligned}
 H &= \sum_{I=1}^N \frac{\mathbf{P}_I^2}{2M_I} + \sum_{i=1}^{N_e} \frac{\mathbf{p}_i^2}{2m_i} + \sum_{i>j} \frac{e^2}{|r_i - r_j|} + \sum_{I>J} \frac{Z_I Z_J e^2}{|\mathbf{R}_I - \mathbf{R}_J|} - \sum_{i,I} \frac{Z_I e^2}{|\mathbf{R}_I - \mathbf{r}_i|} \\
 &\equiv T_N + T_e + V_{ee}(\mathbf{r}) + V_{NN}(\mathbf{R}) + V_{eN}(\mathbf{r}, \mathbf{R}) \quad (1.12)
 \end{aligned}$$

where m is the mass of the electron and $Z_I e$ is the charge on the I^{th} nucleus. In the second line, T_N , T_e , V_{ee} , V_{NN} and V_{eN} represent the nuclear and electron kinetic energy operators and electron–electron, nuclear–nuclear and electron–nuclear interaction potential operators, respectively. In order to solve the complete quantum mechanical problem, the eigenfunctions and eigenvalues of this Hamiltonian have to be sought, which will be given by solution of the time-independent Schrödinger equation

$$[T_N + T_e + V_{ee}(\mathbf{r}) + V_{NN}(\mathbf{R}) + V_{eN}(\mathbf{r}, \mathbf{R})] \Psi(\mathbf{x}, \mathbf{R}) = E(\mathbf{x}, \mathbf{R}) \Psi(\mathbf{x}, \mathbf{R}) \quad (1.13)$$

where $\mathbf{x} \equiv (\mathbf{r}, \mathbf{s})$ denotes the full collection of electron position and spin variables, and $\Psi(\mathbf{x}, \mathbf{r})$ is an eigenfunction of H with eigenvalue E . Clearly, an exact solution of equation 1.13 is not possible and approximations must be made. The Born–Oppenheimer approximation has to be invoked, recognizing that, in a dynamical sense, there is a strong separation of timescales between the electronic and nuclear motion, since the electrons are lighter than the nuclei by three orders of magnitude. In terms of equation 1.13, this can be exploited by assuming

a quasi-separable ansatz of the form

$$\Psi(\mathbf{x}, \mathbf{R}) = \phi(\mathbf{x}, \mathbf{R})\chi(\mathbf{R}) \quad (1.14)$$

where $\chi(\mathbf{R})$ is a nuclear wavefunction and $\phi(\mathbf{x}, \mathbf{R})$ is an electronic wavefunction that depends parametrically on the nuclear positions. At this point it should be noted that an alternative derivation using a fully separable ansatz to the time-dependent Schrödinger equation was presented by Marx and Hutter in [10]. Substitution of equation 1.14 into 1.13 and recognizing that the nuclear wavefunction $\chi(\mathbf{R})$ is more localized than the electronic wavefunction, *i.e.* $\nabla_I \chi \mathbf{R} \gg \nabla_I \phi(\mathbf{x}, \mathbf{R})$, yields

$$\frac{[T_e + V_{ee}(\mathbf{r}) + V_{eN}(\mathbf{r}, \mathbf{R})]\phi(\mathbf{x}, \mathbf{R})}{\phi(\mathbf{x}, \mathbf{R})} = E - \frac{[T_N + V_{NN}(\mathbf{R})]\chi(\mathbf{R})}{\chi(\mathbf{R})} \quad (1.15)$$

From the above, it is clear that the left-hand side can only be a function of \mathbf{R} alone. Let this function be denoted $\varepsilon(\mathbf{R})$. Thus,

$$\frac{[T_e + V_{ee}(\mathbf{r}) + V_{eN}(\mathbf{r}, \mathbf{R})]\phi(\mathbf{x}, \mathbf{R})}{\phi(\mathbf{x}, \mathbf{R})} = \varepsilon(\mathbf{R}) \quad (1.16)$$

$$[T_e + V_{ee}(\mathbf{r}) + V_{eN}(\mathbf{r}, \mathbf{R})]\phi(\mathbf{x}, \mathbf{R}) = \varepsilon(\mathbf{R})\phi(\mathbf{x}, \mathbf{R})$$

Equation 1.16 is an electronic eigenvalue equation for an electronic Hamiltonian, $H_e(\mathbf{R}) = T_e + V_{ee}(\mathbf{r}) + V_{eN}(\mathbf{r}, \mathbf{R})$ which will yield a set of normalized eigenfunctions $\phi_n(\mathbf{x}, \mathbf{R})$ and eigenvalues $\varepsilon_n(\mathbf{R})$, which depend parametrically on the nuclear positions, \mathbf{R} . For each solution, there will be a nuclear eigenvalue equation:

$$[T_N + V_{NN}(\mathbf{R} + \varepsilon_n(\mathbf{R}))]\chi(\mathbf{R}) = E\chi(\mathbf{R}) \quad (1.17)$$

Moreover, each electronic eigenvalue, $\varepsilon_n(\mathbf{R})$, will give rise to an electronic surface on which the nuclear dynamics is determined by a time-dependent Schrödinger equation for the time-dependent nuclear wavefunction $X(\mathbf{R}, t)$

$$[T_N + V_{NN}(\mathbf{R} + \varepsilon_n(\mathbf{R}))]X(\mathbf{R}, t) = i\hbar \frac{\partial}{\partial t} X(\mathbf{R}, t) \quad (1.18)$$

The physical interpretation of equation 1.18 is that the electrons respond instantaneously to the nuclear motion; therefore, it is sufficient to obtain a set of instantaneous electronic eigenvalues and eigenfunctions at each nuclear configuration, \mathbf{R} (hence the parametric dependence of $\phi_n(\mathbf{x}, \mathbf{R})$ and $\varepsilon_n(\mathbf{R})$ on \mathbf{R}). The eigenvalues, in turn, give a family of (uncoupled) potential surfaces on which the nuclear wavefunction can evolve. Of course, these surfaces can (and often do) become coupled by so-called non-adiabatic effects, contained in the terms that have been neglected in the above derivation. In many cases, non-adiabatic

effects can be neglected, and it is possible to consider motion only on the ground electronic surface described by

$$[T_e + V_{ee}(\mathbf{r}) + V_{eN}(\mathbf{r}, \mathbf{R})]\phi_0(\mathbf{x}, \mathbf{R}) = \varepsilon_0(\mathbf{R})\phi_0(\mathbf{x}, \mathbf{R}) \quad (1.19)$$

$$[T_N + V_{NN}(\mathbf{R} + \varepsilon_0(\mathbf{R}))]X(\mathbf{R}, t) = i\hbar \frac{\partial}{\partial t} X(\mathbf{R}, t)$$

Moreover, if nuclear quantum effects can be neglected, then it is possible to get the classical nuclear evolution by assuming $X(\mathbf{R}, t)$ is of the form

$$X(\mathbf{R}, t) = A(\mathbf{R}, t)e^{iS(\mathbf{R}, t)/\hbar} \quad (1.20)$$

and neglecting all terms involving \hbar , which yields an approximate equation for $S(\mathbf{R}, t)$

$$H_N(\nabla_1 S, \dots, \nabla_N S, \mathbf{R}_1, \dots, \mathbf{R}_N) + \frac{\partial S}{\partial t} = 0 \quad (1.21)$$

This is just the classical Hamiltonian–Jacobi equation with

$$H_N(\mathbf{P}_1, \dots, \mathbf{P}_N, \mathbf{R}_1, \dots, \mathbf{R}_N) = \sum_{I=1}^N \frac{\mathbf{P}_I^2}{2M_I} + V_{NN}(\mathbf{R}) + \varepsilon_0(\mathbf{R}) \quad (1.22)$$

denoting the classical nuclear Hamiltonian. The Hamilton–Jacobi equation is equivalent to classical motion on the ground–state surface, $E_0(\mathbf{R}) = \varepsilon_0(\mathbf{R}) + V_{NN}(\mathbf{R})$, given by

$$\dot{\mathbf{R}}_I = \frac{\mathbf{P}_I}{M_I}, \quad \dot{\mathbf{P}}_I = -\nabla_I E_0 \mathbf{R} \quad (1.23)$$

Note that the force $-\nabla_I E_0 \mathbf{R}$ contains a term from the nuclear–nuclear repulsion and a term from the derivative of the electronic eigenvalue, $\varepsilon_0(\mathbf{R})$. Because of the Hellman–Feynman theorem, the latter can be expressed as

$$\nabla_I \varepsilon_0(\mathbf{R}) = \langle \phi_0(\mathbf{R}) | \nabla_I H_e(\mathbf{R}) | \phi_0(\mathbf{R}) \rangle \quad (1.24)$$

Equations 1.23 and 1.24 form the theoretical basis of the AIMD approach. The practical implementation of the AIMD method requires an algorithm for the numerical solution of equation 1.23 with forces obtained from equation 1.24 at each step of the calculation. Moreover, since an exact solution for the ground–state electronic wavefunction, $\phi_0(\mathbf{R})$, and eigenvalue, $\varepsilon_0(\mathbf{R})$, are not available, in general, it is necessary to introduce an approximation scheme for obtaining these quantities.

At this point, a simple form for $E_0(\mathbf{R})$ could be introduced, giving rise to a force field based approach. Such a form would necessarily be specific to a particular system and, therefore, not be transferable to other situations. If, on the other hand, one derives forces directly from very accurate electronic structure

calculations, the computational overhead associated with the method will be enormous. It is clear, therefore, that the practical utility of the AIMD approach relies on a compromise between accuracy and efficiency of the electronic structure representation based on available computing resources. The most common approaches are Hartree-Fock and density functional theory (DFT), that proved to be particularly successful in this regard.

1.2.2 Density Functional Theory – The basics

DFT is based on a one-to-one mapping exists between ground-state electronic densities and external potentials, as stated by the Hohenberg–Kohn theorems. The ground-state density, $n_0(\mathbf{r})$, is given in terms of the ground-state wavefunction by

$$n_0(\mathbf{r}) = \sum_{\mathbf{s}_1, \dots, \mathbf{s}_{N_e}} \int d\mathbf{r}_2 \dots d\mathbf{r}_{N_e} |\phi_0(\mathbf{r}, \mathbf{s}, \mathbf{r}_2, \mathbf{s}_2, \dots, \mathbf{r}_{N_e}, \mathbf{s}_{N_e})|^2 \quad (1.25)$$

(Here, \mathbf{r} and \mathbf{s} represent a single position and spin variable, respectively.) A consequence of the Hohenberg–Kohn theorems is that the exact ground-state energy, $\varepsilon_0(\mathbf{R})$, can be obtained by minimizing a certain functional, $\varepsilon[n]$, over all electronic densities $n(\mathbf{r})$ that can be associated with an antisymmetric ground-state wavefunction, $|\psi_0\rangle$, of a Hamiltonian H_e for some potential V_{eN} (the so called v -representability condition) subject to the restriction that $\int d\mathbf{r} n(\mathbf{r}) = N_e$. The theorem can also be extended to the so called N -representable densities (obtained from any antisymmetric wavefunction) via the Levy prescription.[11, 12] The functional $\varepsilon[n]$ is given as a sum, $T[n] + W[n] + V[n]$, where $T[n]$ and $W[n]$ represent the kinetic energy and Coulomb repulsion energies, respectively, and $V[n] = \int d(\mathbf{r}) V_{eN}(\mathbf{r}) n(\mathbf{r})$. Although the functional $T[n] + W[n]$ is universal for all systems of N_e electrons, its form is not known. Thus, in order that DFT be of practical utility, Kohn and Sham (KS) introduced the idea of a non-interacting reference system with a potential $V_{KS}(\mathbf{r}, \mathbf{R})$, such that the ground-state energy and density of the non-interacting system equal those of the true interacting system.[13] Within the KS formulation of DFT, a set of n_{occ} orthonormal single-particle orbitals, $\psi_i(\mathbf{r})$, $i = 1, \dots, n_{occ}$, with occupation numbers f_i , where $\sum_{i=1}^{n_{occ}} f_i = N_e$, is introduced. These are known as the KS orbitals. In terms of the KS orbitals, the density is given by

$$n(\mathbf{r}) = \sum_{i=1}^{n_{occ}} f_i |\psi_i(\mathbf{r})|^2 \quad (1.26)$$

and the functional takes the form

$$\begin{aligned} \varepsilon[\{\psi_i\}] &= -\frac{\hbar^2}{2m} \sum_{i=1}^{n_{occ}} f_i \langle \psi_i | \nabla^2 | \psi_i \rangle + \frac{e^2}{2} \int d\mathbf{r} d\mathbf{r}' \frac{n(\mathbf{r})n(\mathbf{r}')}{|\mathbf{r} - \mathbf{r}'|} + \varepsilon_{XC}[n] \\ &\quad + \int d\mathbf{r} n(\mathbf{r}) V_{eN}(\mathbf{r}, \mathbf{R}) \\ &\equiv T_{nonint}[\{\psi\}] + J[n] + \varepsilon_{XC}[n] + V[n] \end{aligned} \quad (1.27)$$

The first term in the functional represents the quantum kinetic energy, the second is the direct Coulomb term from Hartree–Fock theory, the third term is the exact exchange–correlation energy, whose form is unknown, and the fourth term is the interaction of the electron density with the external potential due to the nuclei. Thus, the KS potential is given by

$$V_{KS}(\mathbf{r}, \mathbf{R}) = \frac{e^2}{2} \int d\mathbf{r}' + V_{eN}(\mathbf{r}, \mathbf{R}) \quad (1.28)$$

and the Hamiltonian of the non-interacting system is, therefore,

$$H_{KS} = -\frac{\hbar^2}{2m} \nabla^2 + V_{KS}(\mathbf{r}, \mathbf{R}) \quad (1.29)$$

The KS orbitals will be the solutions of a set of self-consistent equations known as the Kohn–Sham equations

$$H_{KS}\psi_i(\mathbf{r}) = \varepsilon_i\psi_i(\mathbf{r}) \quad (1.30)$$

where ε_i are the KS energies. Equation 1.30 constitutes a self-consistent problem because the KS orbitals are needed to compute the density, which is needed, in turn, to specify the KS Hamiltonian. However, the latter must be specified in order to determine the orbitals and orbital energies. The preceding discussion makes clear the fact that DFT is, in principle, an exact theory for the ground state of a system. However, because the exchange–correlation functional, defined to be $\varepsilon_{XC}[n] = T[n] - T_{nonint}[\{\psi\}] + W[n] - J[n]$, is unknown, in practice, approximations must be made. One of the most successful approximations is the so called local density approximation (LDA), in which the functional is taken as the spatial integral over a local function that depends only on the density:

$$\varepsilon_{XC}[n] \approx \int d\mathbf{r} f_{LDA}(n(\mathbf{r})) \quad (1.31)$$

The LDA is physically motivated by the notion that the interaction between the electrons and the nuclei creates only weak inhomogeneities in the electron density. Therefore, the form of LDA is obtained by evaluating the exact ex-

pressions for the exchange and correlation energies of a homogeneous electron gas of uniform density n at the inhomogeneous density $n(\mathbf{r})$. The LDA has been successfully used in numerous applications of importance in solid state physics, including studies of semiconductors and metals. In many instances of importance in chemistry, however, the electron density possesses sufficient inhomogeneities that the LDA breaks down. It could be improved by adding an additional dependence on the lowest order gradients of the density:

$$\varepsilon_{\text{XC}}[n] \approx \int d\mathbf{r} f_{\text{GGA}}(n(\mathbf{r}), |\nabla^2 n(\mathbf{r})|) \quad (1.32)$$

which is known as the generalized gradient approximation (GGA). Among the most widely used GGAs are those of Becke[14], Lee and Parr[15], Perdew and Wang,[16] Perdew, Becke and Ernzerhof,[17] and Cohen and Handy.[18, 19, 20] Typically, these can be calibrated to reproduce some subset of the known properties satisfied by the exact exchange–correlation functional. However, GGAs are also known to underestimate transition state barriers and cannot adequately treat dispersion forces. Attempts to incorporate dispersion interactions in an empirical way have recently been proposed.[21] In order to improve reaction barriers, new approximation schemes such as Becke’s 1992 functional,[22] which incorporates exact exchange, and the so-called meta-GGA functionals,[23, 24, 25, 26] which include an additional dependence on the electron kinetic energy density

$$\tau(\mathbf{r}) = \sum_{i=1}^{n_{\text{occ}}} f_i |\nabla \phi_i(\mathbf{r})|^2 \quad (1.33)$$

have been proposed with reasonable success. However, the problem of designing accurate approximate exchange–correlation functionals remains one of the greatest challenges in DFT. Finally, in order to overcome the limitations of DFT in the context of AIMD, it is, of course, possible to employ, thanks also to the more powerful computing platform available, a more accurate electronic structure method, and approaches using full configuration–interaction representations have been proposed.[27] Typically, these have a higher computational overhead and, therefore, can only be used to study smaller systems such as very small clusters.

1.2.3 Basis set expansions

The more traditional and highly successful way to calculate the electronic properties of large system based on DFT theory uses atom-localised functions expanded in Gaussians as their basis set. This approach can optimally exploit the properties of Gaussians, but finds a bottleneck in the calculation of the Hartree and exchange–correlation (XC) potentials.

Hutter *et al.* presented a DFT-based algorithm for periodic and non-periodic *ab initio* calculations. This scheme uses pseudopotentials in order to integrate out the core electrons from the problem. The valence pseudo-wavefunctions are expanded in Gaussian-type orbitals and the density is represented in a plane-wave auxiliary basis.

The Kohn-Sham orbitals are expanded in Gaussian-type functions and a plane-wave-type approach is used to represent the electronic density.

1.2.3.1 Plane-wave basis sets

In MD calculations, the most commonly employed boundary conditions are periodic boundary conditions, in which the system is replicated infinitely in space. This is clearly a natural choice for solids and is particularly convenient for liquids. In an infinite periodic system, the KS orbitals become Bloch functions of the form

$$\psi_{ik}(\mathbf{r}) = \exp^{i\mathbf{k}\cdot\mathbf{r}} u_{ik}(\mathbf{r}) \quad (1.34)$$

where \mathbf{k} is a vector in the first Brillouin zone and $u_{ik}(\mathbf{r})$ is a periodic function. A natural basis set for expanding a periodic function is the plane-wave basis set, in which $u_{ik}(\mathbf{r})$ is expanded according to

$$u_{ik}(\mathbf{r}) = \frac{1}{\Omega} \sum_g c_{i,g}^k \exp^{ig\cdot\mathbf{r}} \quad (1.35)$$

where Ω is the volume of the cell, $\mathbf{g} = 2\pi\mathbf{h}^{-1}\hat{\mathbf{g}}$ is a reciprocal lattice vector, \mathbf{h} is the cell matrix, whose columns are the cell vectors ($\Omega = \det(\mathbf{h})$), $\hat{\mathbf{g}}$ is a vector of integers and $\{c_{i,g}^k\}$ are the expansion coefficients. An advantage of plane-waves is that the sums needed to go back and forth between reciprocal space and real space can be performed efficiently using fast Fourier transforms (FFTs). In general, the properties of a periodic system are only correctly described if a sufficient number of \mathbf{k} -vectors are sampled from the Brillouin zone. However, for the applications to be considered herein, which are largely concerned with nonmetallic systems, it is generally sufficient to consider a single \mathbf{k} point, ($\mathbf{k} = (0, 0, 0)$) known as the Γ -point, so that the plane-wave expansion reduces to

$$\psi_i(\mathbf{r}) = \frac{1}{\Omega} \sum_g c_{i,g}^k \exp^{i\mathbf{g}\cdot\mathbf{r}} \quad (1.36)$$

At the Γ -point, the orbitals can always be chosen to be real functions. Therefore, the plane-wave expansion coefficients satisfy the following property:

$$c_{i,g}^* = c_{i,g} \quad (1.37)$$

which requires keeping only half of the full set of plane-wave expansion coefficients. In actual applications, only plane-waves up to a given cutoff, $\hbar^2|g|^2/2m > E_{cut}$, are kept. Similarly, the density $n(\mathbf{r})$ given by equation 1.26 can also be expanded in a plane-wave basis as

$$n(\mathbf{r}) = \frac{1}{\Omega} \sum_g n_g \exp^{ig \cdot \mathbf{r}} \quad (1.38)$$

Using the equations 1.36 and 1.38 is then possible to calculate the various energy contributions, kinetic, Hartree, exchange and correlation energies in terms of plane-waves. Therefore, core electrons are often replaced by atomic pseudopotentials,[28, 29, 30, 31] or treated via augmented plane-wave techniques,[32] (the last allow all-electron calculation).

In the atomic pseudopotential scheme, the nucleus plus the core electrons are treated in a frozen core type approximation as an “ion” carrying only the valence charge. In order to make this approximation, the valence orbitals, which, in principle, must be orthogonal to the core orbitals, must see a different pseudopotential for each angular momentum component in the core, which means that the pseudopotential must generally be non-local. For further details see section 1.2.3.4

PWs have a series of advantages that are at the heart of their success. PWs are atomic position independent; this makes the calculation of the Hellmann-Feynman forces very simple. PWs are totally unbiased and do not lead to basis set superposition errors. The calculation of the Hartree potential is very simple and checking the convergence of the calculation is trivial. Furthermore, the use of the fast Fourier transform technique considerably simplifies many manipulations. There are, however, significant disadvantages in using PWs. Most noticeably, a large number of PWs is needed to reproduce the rapid variations of the wavefunctions close to the nuclei. This is alleviated by the use of pseudopotentials, but for several elements unreasonably large basis sets are still needed. Even more paradoxical is the fact that with PWs empty regions of space need to be represented with the same accuracy as the atom-filled regions, leading to further waste. This makes PW based algorithms very demanding in terms of memory, which at present is probably the major bottleneck for these calculations. Another problem with PWs is that they are not the natural language of chemistry. The interpretation of the results is not straightforward and PW results need to be projected into a localized basis set in order to extract the relevant chemistry. There was therefore a definite need to find alternatives to the PW approach so as to remove its main defects while at the same time preserving most of the advantages: *e.g.* it is a good choice to use Gaussians to represent the KS orbitals.

1.2.3.2 Gaussian basis sets

There is a great advantage to be gained by the use of localized basis sets over a delocalized basis like plane-waves. In particular, the computations scale better for well localized orbitals. One of the most widely used localized basis sets is the Gaussian basis. In a Gaussian basis, the KS orbitals are expanded according to

$$\psi_i(\mathbf{r}) = \sum_{\alpha,\beta,\gamma} C_{\alpha\beta\gamma}^i G_{\alpha\beta\gamma}(\mathbf{r}; \mathbf{R}) \quad (1.39)$$

where the basis functions, $G_{\alpha\beta\gamma}(\mathbf{r}; \mathbf{R})$, are centred on atoms and, therefore, are dependent on the positions of the atoms. The basis functions generally take the form

$$G_{\alpha\beta\gamma}(\mathbf{r}; \mathbf{R}) = N_{\alpha\beta\gamma} x^\alpha y^\beta z^\gamma \exp^{-|\mathbf{r}-\mathbf{R}_I|^2/2\sigma_{\alpha\beta\gamma}^2} \quad (1.40)$$

with integer α , β and γ for the Gaussian centred on atom I . The advantage of Gaussians is that many of the integrals appearing in the DFT functional (and in other electronic structure methods) can be done analytically. The main disadvantage, however, is that Gaussian basis sets are non-orthogonal and, hence, the overlap matrix between basis functions needs to be included in the various energy terms. Moreover, being dependent on atomic positions, the derivatives of the basis functions with respect to positions need to be computed. This leads to a considerable degree of complication for MD. Finally, with Gaussian bases, it is difficult to reproduce the correct asymptotic behaviour of the density, and one must always be aware of the effects of basis set superposition errors. Many of these problems can be eliminated by choosing to work with a simpler localized orthonormal basis set

1.2.3.3 Gaussian and plane-waves methods

The standard computational approach to DFT is already efficient and thus appropriate for fairly large systems, currently about $\sim 10^2$ atoms. Nevertheless, the computation of the Hartree (Coulomb) energy and the orthogonalisation of the wave functions are not scaling linearly with system size, and these terms therefore dominate the computational cost for larger systems.[33] The hybrid Gaussian and plane-waves (GPW) method provides an efficient way to treat these terms accurately at a significantly reduced cost.[34] The method uses an atom-centred Gaussian-type basis to describe the wave functions, but uses an auxiliary plane wave basis to describe the density. With a density represented as plane-waves or on a regular grid, the efficiency of Fast Fourier Transforms (FFT) can be exploited to solve the Poisson equation and to obtain the Hartree energy in a time that scales linearly with the system size. Fast Fourier Transforms and regular grids are well established in plane wave codes.[10]

Periodic boundary conditions follow naturally from the FFT based treatment of the Poisson equation, and the GPW method scales linearly for three-dimensional systems with a small prefactor and an early onset. The GPW method seems therefore best suited for the simulation of large and dense systems, such as liquids and solids. The extensive experience with Gaussian-type basis sets shows that basis set sequences that increase rapidly in accuracy can be constructed in a systematic way. At the same time, a compact description of the wave functions is maintained, and this opens the way for efficient methods to solve for the self-consistent field (SCF) equations. Furthermore, as Gaussian functions are localised, the representations of the Kohn–Sham, overlap and density matrix in this basis become sparse with increasing system size. This eventually allows for solving the Kohn–Sham (KS) equations using computational resources that scale linearly with system size. In particular it is possible to evaluate analytically in a fairly straightforward and efficient way all the density independent terms of the KS Hamiltonian.

Central in the Gaussian and plane-wave (GPW) method is the use of two representations of the electron density.[34] Such a dual representation allows for an efficient treatment of the electrostatic interactions, and leads to a scheme that has a linear scaling cost for the computation of the total energy and Kohn–Sham matrix with respect to the system size. The first representation of the electron density $n(\mathbf{r})$ is based on an expansion in atom centred, contracted Gaussian functions

$$n(\mathbf{r}) = \sum_{\mu\nu} P^{\mu\nu} \varphi_{\mu}(\mathbf{r}) \varphi_{\nu}(\mathbf{r}) \quad (1.41)$$

where $P^{\mu\nu}$ is a density matrix element, and $\varphi_{\mu}(\mathbf{r}) = \sum_{i\mu} d_{i\mu} G_i(\mathbf{r})$ with primitive Gaussian functions $G_i(\mathbf{r})$ and corresponding contraction coefficients $d_{i\mu}$. The second representation employs an auxiliary basis of plane-waves, and, as presented in equation 1.38, is given by

$$\tilde{n}(\mathbf{r}) = \frac{1}{\Omega} \sum_{\mathbf{g}} \tilde{n}(\mathbf{g}) \exp(i\mathbf{g}\cdot\mathbf{r}) \quad (1.42)$$

where Ω is the volume of the unit cell, and \mathbf{g} are the reciprocal lattice vectors. The expansion coefficients $\tilde{n}(\mathbf{g})$ are such that $\tilde{n}(\mathbf{r})$ is equal to $n(\mathbf{r})$ on a regular grid in the unit cell. This choice allows for a rapid conversion between $n(\mathbf{r})$, $\tilde{n}(\mathbf{r})$, $\tilde{n}(\mathbf{g})$ using an efficient mapping procedure and fast Fourier transforms (FFT). Using this dual representation, the Kohn–Sham DFT energy expression as employed within the GPW framework is defined as depicted in equation 1.43, where $E^T[n]$ is the electronic kinetic energy, $E^V[n]$ is the electronic interaction with the ionic cores, $E^H[n]$ is the electronic Hartree energy and $E^{XC}[n]$ is the exchange–correlation energy. The interaction energies of the ionic cores with charges Z_A and positions \mathbf{R}_A is denoted by E^{II} . $E^V[n]$ is described by norm–

conserving pseudopotentials with a potential split in a local part $V_{\text{loc}}^{\text{PP}}(r)$ and a fully non-local part $V_{\text{nl}}^{\text{PP}}(\mathbf{r}, \mathbf{r}')$.

$$\begin{aligned}
E[n] &= E^T[n] + E^V[n] + E^H[n] + E^{XC}[n] + E^{\text{II}} \\
&= \sum_{\mu\nu} P^{\mu\nu} \langle \varphi_\mu(\mathbf{r}) | -\frac{1}{2} \nabla^2 | \varphi_\nu(\mathbf{r}) \rangle \\
&\quad + \sum_{\mu\nu} P^{\mu\nu} \langle \varphi_\mu(\mathbf{r}) | V_{\text{loc}}^{\text{PP}}(r) | \varphi_\nu(\mathbf{r}) \rangle \\
&\quad + \sum_{\mu\nu} P^{\mu\nu} \langle \varphi_\mu(\mathbf{r}) | V_{\text{nl}}^{\text{PP}}(\mathbf{r}, \mathbf{r}') | \varphi_\nu(\mathbf{r}') \rangle \\
&\quad + 2\pi\Omega \sum_{\mathbf{g}} \frac{\tilde{n}^*(\mathbf{g})\tilde{n}(\mathbf{g})}{\mathbf{g}^2} + \int e^{XC}(\mathbf{r}) d\mathbf{r} \\
&\quad + \frac{1}{2} \sum_{I \neq J} \frac{Z_I Z_J}{|\mathbf{R}_I - \mathbf{R}_J|}
\end{aligned} \tag{1.43}$$

1.2.3.4 Pseudopotentials

An expansion of an atomic all-electron density or wave function in plane-waves is computationally inefficient. However, to describe a wide range of chemically interesting events, such as bond breaking and formation, an accurate description is required only for the valence electrons. Such an accurate description can be obtained using a pseudopotential description of the nuclei.

The Goedecker–Teter–Hutter (GTH) pseudopotentials, as implemented in CP2K will be discussed: this norm-conserving, separable, dual-space pseudopotentials consist of a local part including a long-ranged (LR) and a short-ranged (SR) term

$$\begin{aligned}
V_{\text{loc}}^{\text{PP}}(r) &= V_{\text{loc}}^{\text{LR}}(r) + V_{\text{loc}}^{\text{SR}}(r) \\
&\quad - \frac{Z_{\text{ion}}}{r} \text{erf}(\alpha^{\text{PP}} r)^2 + \sum_{i=1}^4 C_i^{\text{PP}} (\sqrt{2}\alpha^{\text{PP}} r)^{2i-2} \times \exp^{-(\alpha^{\text{PP}} r)^2}
\end{aligned} \tag{1.44}$$

* with $\alpha^{\text{PP}} = 1/(\sqrt{2}r_{\text{loc}}^{\text{PP}})$ and a non-local part

$$V_{\text{nl}}^{\text{PP}}(\mathbf{r}, \mathbf{r}') = \sum_{lm} \sum_{ij} \langle \mathbf{r} | p_i^{lm} \rangle h_{ij}^l \langle p_j^{lm} | \mathbf{r}' \rangle \tag{1.45}$$

with the Gaussian-type projectors

$$\langle \mathbf{r} | p_i^{lm} \rangle = N_i^l Y^{lm}(\hat{r}) r^{l+2i-2} \exp\left[-\frac{1}{2}\left(\frac{r}{r_l}\right)^2\right] \tag{1.46}$$

*erf stands for the error function (also called the Gauss error function or probability integral): it is a special function (non-elementary) of sigmoid shape which occurs in probability, statistics, materials science, and partial differential equations.

where N_i^l are normalisation constants and $Y^{lm}(\hat{r})$ spherical harmonics. The small set of GTH pseudopotential parameters ($r_{\text{loc}}^{\text{PP}}$, C_i^{PP} , r_l and h_{ij}^l) optimised with respect to atomic all-electron wave functions as obtained from fully relativistic density functional calculations using a numerical atomic program. The optimised pseudopotentials include all scalar relativistic corrections via an averaged potential [35] and improve therefore the accuracy for applications involving heavier elements. The emphasis in the construction of these pseudopotentials has been on accuracy, and hence these pseudopotentials are computationally more demanding for plane-wave methods, as a large plane-wave basis typically is required. The GPW method is less sensitive to the hardness of the pseudopotential since the kinetic energy as in equation 1.43 and the short range pseudopotential terms are computed analytically in the Gaussian basis. The long range term can be efficiently treated as part of the electrostatic energy, whereas the short range terms can be easily computed as two and three centre overlap integrals.

The electrostatic energy in a periodic system is defined by a conditionally converging sum in which the separate contributions of ions and electrons are infinite. All terms of the electrostatic energy are therefore treated simultaneously using the Ewald sum method

$$E^{ES} = \int V_{\text{loc}}^{\text{PP}}(\mathbf{r})n(\mathbf{r})d\mathbf{r} + 2\pi\Omega \sum_{\mathbf{g}} \frac{\tilde{n}^*(\mathbf{g})\tilde{n}(\mathbf{g})}{g^2} + \frac{1}{2} \sum_{I \neq J} \frac{Z_I Z_J}{|\mathbf{R}_I \mathbf{R}_J|} \quad (1.47)$$

At the basics of the DFT techniques is the introduction of an approximate exchange and correlation functional E^{XC} . These functionals have the common general form †

$$E^{\text{XC}}[n] = \int e^{\text{XC}}(n_{\uparrow}(\mathbf{r}), n_{\downarrow}(\mathbf{r}), \nabla n_{\uparrow}(\mathbf{r}), \nabla n_{\downarrow}(\mathbf{r}), \tau_{\uparrow}, \tau_{\downarrow})d\mathbf{r} \quad (1.48)$$

used for generalised gradient approximations (GGA) and meta-GGAs based on the kinetic energy density τ .

1.3 Classical MD

Classical molecular mechanics uses Newtonian mechanics to model molecular systems. The potential energy of all systems in molecular mechanics is calculated using force fields. Molecular mechanics can be used to study small molecules as well as large biological systems or material assemblies with many

†This formulation does not cover functional where the Hartree-Fock exchange term is explicitly introduced, such as B3LYP functional.

thousands to millions of atoms. A force field is built fitting data from both experimental work and high-level quantum mechanical calculations, therefore they are called empirical. The most common force fields could be divided in three classes

- *All-atom*, provide parameters for every atom in a system, including hydrogen;
- *united-atom*, treat the hydrogen and carbon atoms in methyl and methylene groups as a single interaction center;
- *Coarse-grained*, which are frequently used in long-time simulations of proteins, provide even more abstracted representations for increased computational efficiency.

All-atomistic molecular mechanics methods have the following properties: each atom is simulated as a single particle, each particle is assigned a radius (typically the van der Waals radius), polarizability, and a constant net charge (generally derived from quantum calculations and/or experiments) and bonded interactions are treated as “springs” with an equilibrium distance equal to the experimental or calculated bond length. Variations on this theme are possible; for example, many simulations have historically used a “united-atom” representation in which methyl and methylene groups were represented as a single particle, as depicted above. The force field refers to the functional form and parameter sets used to describe the potential energy of a system of particles – atoms or superatoms.

Some existing force fields do not account for electronic polarization of the environment, an effect that can significantly reduce electrostatic interactions of partial atomic charges. This problem was addressed by developing “polarizable force fields” or using macroscopic dielectric constant. However, application of a single value of dielectric constant is questionable in any highly heterogeneous environments and the nature of the dielectric depends on the model used.

Most current force fields use a “fixed-charge” model by which each atom is assigned a single value for the atomic charge that is not affected by the local electrostatic environment; proposed developments in next-generation force fields incorporate models for polarizability, in which a particle’s charge is influenced by electrostatic interactions with its neighbors. For example, polarizability can be approximated by the introduction of induced dipoles; it can also be represented by Drude particles, or massless, charge-carrying virtual sites attached by a springlike harmonic potential to each polarizable atom. The introduction of polarizability into force fields in common use has been inhibited by the high computational expense associated with calculating the local electrostatic field.

1.3.1 Force field in formulas

$$V(\mathbf{r}, s) = \overbrace{\sum_{i,j} V^{(2)}(\mathbf{r}_i, \mathbf{r}_j; s)}^{\text{2 atoms interaction}} + \cdots + \overbrace{\sum_N V^N(\mathbf{r}; s)}^{\text{N atoms interaction}} \quad (1.49)$$

$$V(\mathbf{r}_1, \mathbf{r}_2, \dots, \mathbf{r}_N; s) =$$

Bond Interactions	{	$\sum_{\text{bonds}} \frac{1}{2} K_b (b - b_0)^2$	+
		$\sum_{\text{angles}} \frac{1}{2} K_\theta (\theta - \theta_0)^2$	+
		$\sum_{\text{improper dihedrals}} \frac{1}{2} K_\xi (\xi - \xi_0)^2$	+
		$\sum_{\text{dihedrals}} K_\phi [1 + \cos(n\phi - \delta)]$	+
V_b			
V_θ			
V_ξ			
V_ϕ			
non-Bonding Interactions	{	$\sum_{i,j \text{ pairs}} \left(\frac{C_{ij}^{12}}{r_{ij}^{12}} - \frac{C_{ij}^6}{r_{ij}^6} \right)$	+
		$\sum_{i,j \text{ pairs}} \left(\frac{V_{vdw} q_i q_j}{4\pi\epsilon_0 \epsilon_r r_{ij}} \right)$	+
		Specials terms	
V_{vdw}			
V_{ei}			

1.3.1.1 Two bodies interactions

Generally, the interactions V_b are harmonic and the constants K_b and the equilibrium values (depicted with a “0” subscript) could be calculated from experiments (crystallographic or spectroscopic) or even theoretically.

Some force fields use the Morse function instead to the harmonic potential for the bonds vibrations

$$V_b = \sum_{\text{bonds}} \mathcal{D}_e \{ \exp[-k_b(b - b_0)] - 1 \}^2 \quad (1.50)$$

where \mathcal{D}_e is the dissociation energy of the bond and $k_b = \omega \sqrt{\mu/2\mathcal{D}_e}$ the force constant, in which ω is the vibrational frequencies and μ the reduced mass. This potential allow a better description of the vibration spanning on a bigger range

of b values.

1.3.1.2 Three bodies interactions

The term V_θ refer to the deformation of the valence angle from the equilibrium value: even in this case the potential is in the harmonic form. However, some force fields allow for a mixed terms that match changes in bond length and angle, like $K_{b\theta}[b - b_0][\theta - \theta_0]$.

1.3.1.3 Four bodies interactions

In the case of four bodies, two terms are used in order to describe:

- Improper dihedral angle, used to correct the deformation of tetrahedral and planar structures;
- Proper dihedral angle, that is a sinusoidal function, where K_ϕ is the force constant, n the number of oscillation occur in the unit time interval and δ the phase.

1.3.2 Non-bonding interactions

These terms concern the interaction between non-bonded couple of atoms: van der Waals & Coulomb interaction.

1.3.2.1 van der Waals

All types of van der Waals forces are strongly environment-dependent, because these forces originate from interactions of induced and “instantaneous” dipoles. The original Fritz-London theory of these forces can only be applied in vacuum. Among the most used formulation to describe non-bonding interaction Buckingham potential (equation 1.51) and Lennard-Jones potential (equation 1.52) are remarkable.

$$V_{ij}^B = A_{ij} \exp[-B_{ij}r_{ij}] - \frac{D_{ij}}{r_{ij}^6} \quad (1.51)$$

The Lennard-Jones potential is given by a sum of two terms describing attractive and repulsive contributions

$$V_{ij}^{LJ} = \overbrace{\frac{C_{ij}^{12}}{r_{ij}^{12}}}^{\text{repulsive term}} - \underbrace{\frac{C_{ij}^6}{r_{ij}^6}}_{\text{attractive term}} \quad (1.52)$$

in which C_{ij}^{12} (that account for short-range repulsive interaction) and C_{ij}^6 (that represents London's forces), are constants that can be obtained from experimental or theoretical data; in particular C_{ij}^{12} could be obtained from the second term of the virial, while the C_{ij}^6 could be obtained from the Slater–Kirkwood equation

$$C_{ij}^6 = \frac{3}{2} \frac{\alpha_i \alpha_j}{\sqrt{\alpha_i/N_i} + \sqrt{\alpha_j/N_j}} = \frac{\alpha_i \alpha_j}{\alpha_i^2 C_{ii}^6 + \alpha_j^2 C_{jj}^6} \quad (1.53)$$

in which $N_i = 16(C_{ii}^6)^2/9\alpha_i^3$ is the number of electrons and α the atomic polarizability. One of the most used Lennard–Jones potential forms is represented by the equation 1.54.

$$V_{ij}^{LJ} = 4\epsilon_{ij} \left[\left(\frac{\sigma_{ij}}{r_{ij}} \right)^{12} - \left(\frac{\sigma_{ij}}{r_{ij}} \right)^6 \right] \quad (1.54)$$

The parameters in this case have a simple physical interpretation: ϵ is the minimum potential energy, located at $r = 2^{1/6}\sigma$, and σ is the diameter of the particle, since for $r < \sigma$ the potential becomes repulsive. A very great advantage choosing the Lennard–Jones potential has to be addressed to the existence of “combinatorial rules”. The Lorentz–Berelot rules state that the interaction energy of two dissimilar atoms (*e.g.* C··N) is an average of the interaction energies of corresponding identical atom pairs (*i.e.* C··C and N··N), as in equation 1.55, but other approaches are available.

$$\begin{aligned} \sigma_{ij} &= \frac{\sigma_{ii} + \sigma_{jj}}{2} \\ \epsilon_{ij} &= \sqrt{\epsilon_{ii} \cdot \epsilon_{jj}} \end{aligned} \quad (1.55)$$

1.3.3 Electrostatic term

The electrostatic interaction is generally described by Coulombic term:

$$\sum_{\text{non bonded pairs}} = -\frac{q_i q_j}{4\pi\epsilon_r r_{ij}} \quad (1.56)$$

Each atom has a partial charge, calculated with a quantummechanics method. Different values have been used for the relative dielectric constant ϵ_r spanning from 1 to 8 and even proportional to the distance r_{ij} . However, to overcome the lack in the description of the physics of the problem, a way is to include the atomic polarizability: in order to do that the equation of the electric field accounting about the induce dipole has to be introduced, like Ewald sum, especially for periodic system. The simulation “cell” is effectively replicated in all spatial directions, so that particles leaving the cell reappear at the opposite boundary. For systems governed by a short-ranged potential it is sufficient

to take just the neighbouring simulation volumes into account, leading to the “minimum-image” configuration. For long-range potentials, this arrangement is inadequate because the contributions from more distant images at 2L, 3L and so on, are no longer negligible and other methods are used.

1.4 What about Reactions?

Many interesting and important processes still lay beyond the time scale accessible with MD simulations even on today’s fastest computers. Indeed, an *ab initio* molecular dynamics simulation of liquid water long enough to observe few dissociations of water molecules would require a multiple of the age of the universe of computing time even on state-of-the-art parallel high performance computers. The computational effort needed to study many other interesting processes, ranging from protein folding to the nucleation of phase transitions and transport in and on solids, in molecular dynamics simulations with atomistic resolution may be less extreme, but still surpasses the capabilities of current computer technology. Fortunately, many processes occurring on long time scale are *rare events*[‡] rather than slow. Consider, for instance, a chemical reaction during which the system has to overcome a large energy barrier on its way from reactants to products. Before the reaction occurs, the system typically spends a long time in the reactant state and only a rare fluctuation can drive the system over the barrier. If this fluctuation happens, however, the barrier is crossed rapidly.

In order to study rare events there are two main approaches. The first one is to renounce the all-atom description and use instead a coarse-grained model (an extensive example will be given in Chapter 3). This would retain only those characteristics which are essential but would require a detailed knowledge of the systems that is often unavailable. If one does not want to renounce to the atomistic description, methodologies aimed at accelerating rare events using the available computer time with improved efficiency are available.

Broadly speaking these methods can be classified in four categories, according to their scope and range of applicability:

- Methods aimed at reconstructing the probability distribution or enhancing the sampling as a function of one or a few predefined collective variables

[‡]Rare events are processes that occur infrequently due to dynamical bottlenecks that separate stable states. Once this threshold is crossed, however, a trajectory will move quickly to the reaction products. This phenomena are of high interest, by the way take place on time scales that are orders of magnitude larger, and are, therefore, rare events on the currently accessible simulation time. Examples of rare events are chemical reactions and structural phase transitions and, in biophysics, protein folding, protein-protein interactions and molecular recognition.

(CVs) – *i.e.* any variable that allows to follow the system along the reactive path.

These approaches are very powerful but require a careful choice of the CVs that must provide a satisfactory description of the reaction coordinate. If an important variable is forgotten they suffer from hysteresis and lack of convergence. Moreover, when more than a few CVs are used, the computational performance rapidly degrades as a function of the number of variables. For instance, in a chemical reaction one would choose the distance between two atoms that have to form a bond. Examples of these methods include thermodynamic integration,[36] free energy perturbation,[37] umbrella sampling,[38] adiabatic molecular dynamics,[39] and metadynamics [40, 41, 42, 43, 44, 45, 46, 47]

- Methods in which the phase space is explored simultaneously at different values of the temperature, such as parallel tempering [48] and replica exchange,[49] or as a function of the potential energy, such as multicanonical MD [50] and Wang–Landau [51] . These approaches are very general and powerful; however, they are not immune from some of the limitations listed in the previous point.

- Methods aimed at exploring the transition mechanism and constructing reactive trajectories. These methods do not require in most of the cases the explicit definition of a reaction coordinate, but require an *a priori* knowledge of the initial and final states of the process that has to be simulated. Examples are nudged elastic band,[52] string method [53, 54, 55] and transition path sampling [56, 56, 57]

- Methods for exploring the potential energy surface and localizing the saddle points that correspond to the transition states such as eigenvalue following, the dimer method,[58] hyperdynamics[59]. These approaches are extremely powerful for exploring potential energy surfaces of low dimensionality, but their reliability degrades with the complexity of the system. Indeed, for very large or complex systems the number of possible transition states surrounding a minimum becomes rapidly too large for a deterministic search. However, in solvated systems the concept of saddle point on the potential energy surface becomes fuzzy, and these approaches cannot easily be applied.

1.5 Programs

1.5.1 CP2K

In this thesis the CP2K suite program have been widely used.

CP2K is a freely available (GPL) program, written in Fortran 95/2003, to perform atomistic and molecular simulations of solid state, liquid, molecular and biological systems. It gives to the user the possibility to choose through a variety of molecular simulation methods at different levels of accuracy, from *ab initio* DFT to classical Hamiltonians, passing through semi-empirical NDDO approximation, Minimum Energy Path techniques, biased methods like Metadynamics and so on.

In particular, among the several methods available to perform the AIMD studies presented in this work the Quickstep one has been chosen. With this module, CP2K provides a way to perform accurate and efficient DFT calculations on large, complex systems such as *e.g.* liquids, crystals, proteins and interfaces. Both static property calculations (such as spectra computed with time dependent-DFT or as derivative properties of the total energy) and dynamical properties are possible. Quickstep is based on the Gaussian and plane-waves method (GPW) and its augmented extension (GAPW). As explained above, central in this approach is a dual basis of atom centred Gaussian orbitals and plane-waves (regular grids). The former is used to represent the wave functions and the Kohn-Sham matrix, whereas the latter is used to represent the electronic density. The key advantages are a compact representation of the wave function, only relatively few basis functions per atom are needed as compared to plane-wave representations. This allows for memory friendly and efficient algorithms. The matrix representation of the Kohn-Sham matrix and density matrix become sparse with increasing system size, allowing for linear scaling methods to perform the density matrix optimisation. Linear scaling computation of the Kohn-Sham energy and matrix is readily achieved using screening techniques and Fast Fourier Transforms to compute the Hartree energy.

The code can be freely downloaded at cp2k.berlios.de/download.html

1.5.2 Gromacs

GROMACS is a versatile package to perform molecular dynamics, that allows to solve the equations of motion for systems of several complexity, spanning from hundreds to millions of particles. It is primarily designed to perform classical molecular dynamics simulation of biochemical molecules like proteins, lipids and

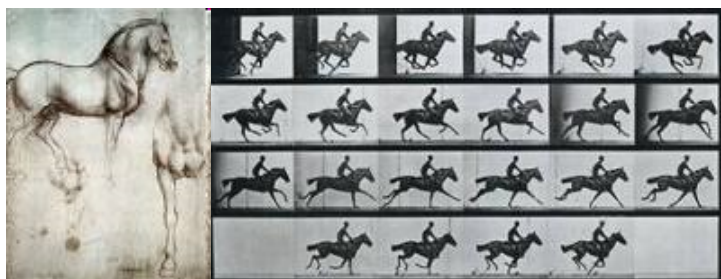
nucleic acids that have a lot of complicated bonded interactions, but since GROMACS is extremely fast at calculating the non-bonded interactions – the common bottleneck of classical molecular dynamics simulation – many groups are also using it for research on non-biological systems, *e.g.* polymers. GROMACS is user-friendly, with topologies and parameter files written in clear text format. Both run input files and trajectories are independent of the available hardware and can thus be read by any version GROMACS, even if it was compiled using a different floating-point precision. GROMACS comes with a large selection of flexible tools for trajectory analysis. The output is further provided in the form of finished Xmgr/Grace graphs, with axis labels, legends, etc. already in place. GROMACS can be run in parallel, using standard MPI communication. The package includes a fully automated topology builder for proteins, even multi-meric structures. Building blocks are available for the 20 standard aminoacid residues as well as some modified ones, the 4 nucleotide and 4 deoxynucleotide residues, several sugars and lipids, and some special groups like hemes and several small molecules. There is ongoing development to extend GROMACS with interfaces both to quantum chemistry and bioinformatics/databases.

GROMACS is a free software, available under the GNU General Public License at www.gromacs.org

Chapter 2

AIMD & Metathesis

The reason to integrate standard static DFT calculations with a dynamics approach lies in the intrinsic different options that the two methods offer. A comparison between a picture and a movie should point out the meaning of the last sentence: with a picture, it is possible to capture any single detail with high resolution, while with a movie it is possible, instead, to follow the dynamics of the system in examination.



(a) Horse drawing – Leonardo da Vinci 1492

(b) The Galloping Horse – Muybridge 1882

Figure 2.1: Statics and Dynamics comparison.

In the same way, to explore the ensemble of accessible conformations or a reaction, static DFT approaches – or analysis of X-ray structures – are useful for the characterization of the species involved but at the same time poorly effective since they freeze the system to a minimum of the potential energy surface. A dynamic approach, instead, is better suited since it allows to follow the real dynamic behavior of the system with time. Said that the two

methods are not exclusive instead complementary. After a preface, in this chapter two examples regarding the catalytic systems with the general formula $[\text{NHC-Ru}(\text{CH}_2)(\text{Cl}_2)(\text{PR}_3)]$ – where NHC stands for N-heterocyclic carbene – widely used in metathesis reaction, will be given:

- in Section 2.4 an accurate comparative analysis of the flexibility of the NHC precatalysts shown in Chart 2.2 will be reported using a combined static and dynamic DFT approach integrated by an analysis of the systems based on the buried volume $\%V_{Bur}$, descriptor presented in details in Section 2.3.
- in Section 2.5 one of the possible pathways for the deactivation of this kind of catalysts induced by coordination of a CO molecule trans olefin metathesis catalyst bearing the NHC ligand SIMes will be explored.

The treatment of them with *ab initio* techniques is mandatory, due first of all to the presence of a transition-metal and, furthermore and especially for the reaction case to the bond breaking/formation, in which the electrons play the most important role and cannot be “coarse-grained” in any way.

2.1 Metathesis

Broadly speaking, metathesis is a molecular process involving the exchange of bonds between the two reacting chemical species, which results in the creation of products with similar or identical bonding affiliations,* besides, the etymology of the word metathesis comes from the Greek $\mu\epsilon\tau\alpha\theta\alpha\epsilon\sigma\iota\zeta$ (metathesis) that means transposition. The chemical species involved can either be ionic or covalent: a general scheme of the metathesis reaction can be represented by the equation $\text{AX} + \text{BY} \rightarrow \text{BX} + \text{AY}$.

Due to its enormous impact on chemistry, with the term metathesis is commonly identified a class of reaction involved in the formation of C–C bonds: in this field, with the exception of Pd-catalyzed cross-couplings, no other group of reactions has had such a profound impact in the last quarter of a century than the metathesis reactions of enynes, alkynes and, by far, the most widely utilized, olefins. The only disadvantage of the most metathesis reaction (the ones that involve terminal π -bonds) is the release of an ethylene molecule, that is against the “atom-economy” approaches. Instead, unlike the corresponding alkene-metathesis reactions, enyne metatheses are wholly atom economical (that is, no olefin-containing by-product is released during the process)[60] and

*International Union of Pure and Applied Chemistry, 2006. IUPAC Gold Book, Compendium of Chemical Terminology IUPAC Publications.

are therefore driven by enthalpic rather than entropic factors, principally the stability of the conjugated diene system thus produced. The enyne–metathesis reaction, involves an alkene with an alkyne to form a 1,3–diene system.[61, 62] Since is off topic to this thesis no more insight will be give.

The alkene–metathesis, could be classified depending on the transformation in all its various *modus operandi* listed here and presented schematically in Figure 2.2:

- *cross–metathesis* – CM, involves the transalkylidenation of two terminal alkenes under release of ethene. Statistically, the reaction can lead to three possible pairs of geometric isomers, *i.e.* *E/Z* pairs for two homocouplings and the cross–coupling ($R-CH=CH-R$, $R'-CH=CH-R'$, and $R-CH=CH-R'$), for a total of 6 products.
- *ring–closing metathesis* – RCM, starting from $\alpha - \omega$ dienes gives rings: has developed into one of the most powerful and reliable methods for ring formation, used also in the syntesis of supramolecular structures, *i.e.* rotaxanes, catenanes, etc.
- *ring–opening metathesis* – ROM, allows to obtain linear dienes starting from cyclic systems; strained rings may be opened by a reaction with a second alkene following the mechanism of the CM. The driving force is the relief of ring strain. As the products contain terminal vinyl groups, further reactions of the Cross Metathesis variety may occur. Therefore, the reaction conditions (time, concentrations, etc.) must be optimized in order to favor the desired product.
- *ring–opening metathesis polymerization* – ROMP, allows the polymerization of cyclic olefins and the synthesis of functionalized polimers; the concept is the same of ROM, but in absence of a second reaction partner in excess;
- *acyclic diene metathesis polymerization* – ADMET, giving the polymerization of acyclic $\alpha - \omega$ dienes. The reaction is driven by the removal of ethylene from the system, which can be accomplished with a nitrogen purge.

For further resumed examples browse the internet site www.organic-chemistry.org. The success of the alkene–metathesis reaction is due to the fact that most catalysts allow to work at room temperature, even in water solvent, and are tolerant to a large variety of functional group; furthermore, these catalysts are commercially available for the synthesis of rather complicated organic molecules and polymers, both in laboratory and industrial scale. The giant step was possible

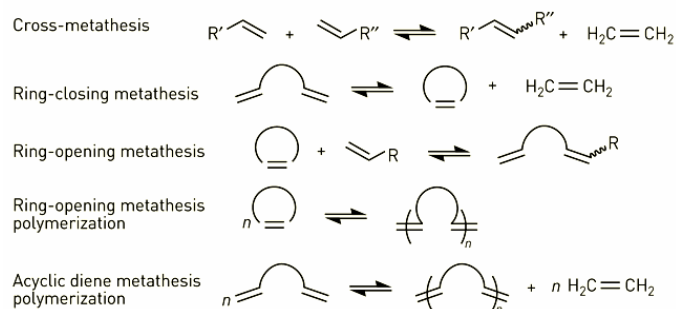


Figure 2.2: Scheme of the metathesis guises. All the reactions are reversible!

when a detailed comprehension of the chemical mechanics at work with these systems was achieved. This understanding was key to the rational design of a large number of more active and, in the broadest sense, better performing catalysts.

2.1.1 Historical background

The history of alkene metathesis is fascinating, beginning with its serendipitous discovery at the end of the 1960's, and the mechanism was really mysterious and a challenge for the science community. The name metathesis was given for the first time to this reaction by Calderon in 1967,[63, 64] but the first observation of the metathesis of propene at high temperature was reported in 1931. The first catalyzed metathesis reactions were found in the 1950's when industrial chemists at Du Pont, Standard Oil and Phillips Petroleum (H. S. Eleuterio, E. F. Peters, B. L. Evering, R. L. Banks and G. C. Bailey) reported that propene led to ethylene and 2-butenes when it was heated with molybdenum, in the form of the metal, oxide or $[Mo(CO)_6]$ on alumina.[65, 66, 67]

Catalytic systems were either oxides such as WO_3/SiO_2 used in industry for the transformation of propene to ethylene and butenes, or Ziegler–Natta derived systems such as WCl_6 (or $MoCl_5$) + AlX_nR_{3-n} or (SnR_4) . Early mechanistic ideas had appeared (Figure 2.3), but they did not match the results of some metathesis experiments. For instance, Calderon had suggested a mechanism involving an intermediate π -cyclobutane–metal species,[64] but the metathesis reaction does not give cyclobutane and metathesis catalysts do not lead to olefins by reaction with cyclobutane derivatives. Y. Chauvin, from the Institut Français du Pétrole, had taken into account the report of E. O. Fischer on the synthesis of a tungsten–carbene complex,[68] that of Natta on the polymerization of cyclopentene by ring-opening catalyzed by a mixture of WCl_6 and $AlEt_3$,[69] and that of R. L. Banks and G. C. Bailey on the formation of ethy-

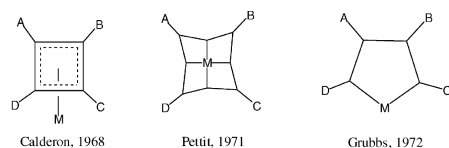


Figure 2.3: Intermediate proposed in the earlier time.

lene and 2-butene from propene catalyzed by $[\text{W}(\text{CO})_6]$ on alumina.[63, 64] Consequently, Y. Chauvin and J.-L. Hérisson published their proposition of metathesis mechanism in 1971,17 Section 2.1.2 with key experimental evidence for its validity subsequently being provided by the Casey,[70] Katz,[71] and Grubbs groups,[72, 73] and invokes metal carbene intermediates as key propagating species in the catalytic cycle. From a practical point of view, a key milestone in the evolution of alkene metathesis was the demonstration by Katz and co-workers in 1976 that single-component, well-defined tungsten carbenes, for example $\text{Ph}_2\text{C}=\text{W}(\text{CO})_5$, could initiate alkene metathesis without added coactivators.[74, 75] This discovery opened the modern era of rational catalyst design, and after further development, the alkene-metathesis reaction has developed into one of the most powerful carbon-carbon bond-forming reactions currently available to the synthetic chemist.

Schrock's work, published in 1980 on the catalysis of the metathesis reaction using non-stabilized transition-metal-alkylidene complexes, that is those really involved in metathesis catalysis, has clearly established the validity of the Chauvin mechanism; since then, this mechanism is universally recognized and accepted.

The evolution of the catalysts continued on and on: up to now is possible to distinguish three main classes of such catalysts most routinely used, showed in Figure 2.4, that came out subsequently in time. Catalyst **a** introduced by Schrock's group in 1990 represents the first real groundbreaking advance in catalyst design, since the tungsten carbenes initially used by Katz and co-workers. It displays a superb metathesis activity with a wide variety of alkene substrates,

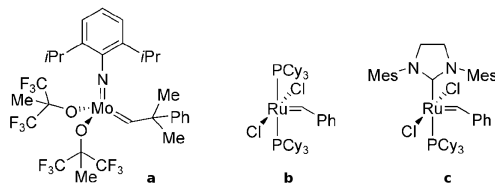


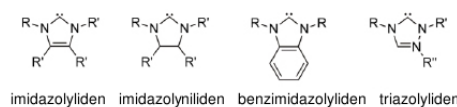
Figure 2.4: The three main classes of metathesis catalysts.

and is particularly useful for the formation of sterically crowded systems. By the way, the main (and basically the only one) drawback of catalyst **a** is its pronounced sensitivity to oxygen, moisture, and certain polar or protic functional

groups owing to the electrophilicity of the high-oxidation-state transition-metal center.

Afterwards, Grubbs and co-workers subsequently introduced ruthenium-based carbene complexes, initially optimized as represented by system **b**, known as “first-generation” Grubbs (pre)catalyst; although less active than the Schrock molybdenum-based systems **a**, it exhibits much greater functional-group tolerance most notably in the total synthesis of complex products, both natural and designed. The use of phosphine ligands PR_3 is ubiquitous in organo-metallic chemistry and homogeneous catalysis,[76] yet these ligands suffer from significant P–C bond degradation at elevated temperatures. Furthermore, specific applications benefit from or require the use of sterically demanding phosphine ligation in order to stabilize reactive intermediates.[78]

Almost simultaneously, Nolan[79] and Grubbs[80] reported the synthesis of related ruthenium alkylidene complexes, with the replacement of one of the phosphine ligands in **b** with an N-heterocyclic carbene ligand, for example, the 1,3-dimesitylimidazolin-2-ylidene complex **12** and its 4,5-dihydroimidazolin-2-ylidene analogues **13** and **14**, using different nucleophilic N-heterocyclic ligands of the Arduengo type,[81, 82] leading the class of system **c**. It is worth emphasising



Scheme 2.1

that the metathesis activity of these new ruthenium complexes is strongly dependent on the nature of the N-heterocyclic ligand, solvent and substrate; the saturated complex is more active with some substrates than the unsaturated one. increases the catalytic activity, thermal stability, and functional-group tolerance of the complex; now they are addressed as the “second-generation” catalyst

Despite these advances, the search for increasingly efficient and selective metathesis catalysts continues unabated. A rapid historical excursus resume of metathesis reaction is reported in Figure 2.5

2.1.2 The Chauvin mechanism

As explained above, the elucidation of the mechanistic pathway took two decades of extensive research by numerous groups, and was the subject of lively debate in the literature during that period, and debate that is still active about the fine details. The Chauvin mechanism, depicted in Figure 2.6 requires the coordination of the olefin onto the metal atom of the metal-alkylidene species, followed

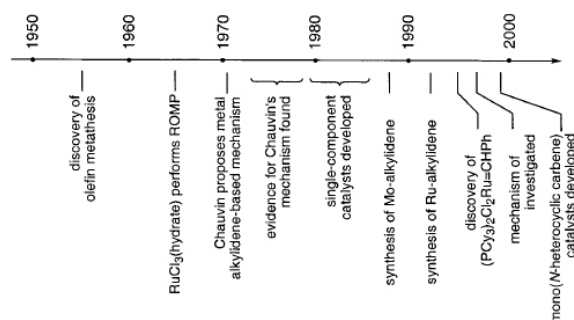


Figure 2.5: Metathesis Vs. Time.

by the shift of the coordinated olefin to form the metallocyclobutane intermediate, and finally the topologically identical shift of the new coordinated olefin in the metallocyclobutane. Since every step of the metathesis reaction is reversible, this shift could give the same starting olefin and catalyst or a new olefin containing a carbene from the catalyst and the other carbene from the starting olefin; in this case the new metal-alkylidene contains one of the two carbenes of the starting olefin and it can re-enter into a catalytic cycle of the same type. Afterwards the olefin is released. In principle, depending on the orientation of

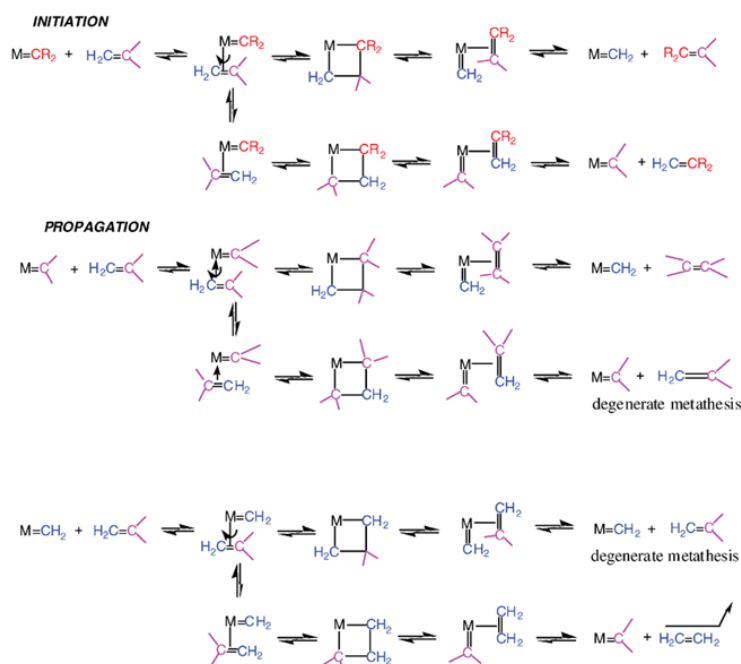


Figure 2.6: The Chauvin Mechanism.

the coordinated olefin, the new catalytic cycle can give two different metallocyclobutenes, one leading to the symmetrical olefin and the other one leading

the starting olefin. This latter cycle is said to be degenerate olefin metathesis. Thus, the catalytic cycles alternatively involve both metal–alkylidene species resulting from the combination of the metal with each of the two carbenes of the starting olefin.

Just for the sake of completeness, such metallocyclobutane complexes are sometimes stable: early elegant studies by Grubbs' group showed that Tebbe's complex $[\text{Cp}_2\text{Ti}(\text{CH}_2)(\text{ClAlMe}_2)]$ [83] reacts with olefins in the presence of dimethylaminopyridine to give titanacyclobutanes that slowly catalyze metathesis and could be used to identify all the intermediates in olefin metathesis.

2.2 N–heterocyclic Carbenes

The first studies on N–heterocyclic carbenes (NHC) compounds has to be addressed to the Wanzlick's work in 1960: he could not isolate any carbenes in a stable form, but he postulated the existence of them, assuming that a C–carbenic center, located in the position 2 in a imidazole ring, could be stabilized. This provided the basis for developing the chemistry of these species. The main impetus to research efforts on the chemistry of NHCs is attributed mainly to the work of Arduengo and co-workers in 1991, they were able to isolate a first stable NHC. The isolated carbene proved to be a solid compound in crystalline form, thermally stable, the structure of which was experimentally confirmed by crystallographic analysis. It has been estimated that 90% of the studies on diamino–carbenes are focused on the five–member cyclic compounds, in which the carbene center is linked to two nitrogen atoms; this is based on the versatility of these species, with respect to carbenes from other N–heterocycles or acyclic diamino carbenes form. NHCs are stable singlet carbenes that can act as excellent two electron donor ligands towards almost any element in the periodic table. They coordinate strongly to late transition metals and heavy main group elements, but are also known to bind to early transition metals and the lanthanoids. NHC derive their excellent stability from their unique electronic structure. The carbene carbon atom is sp^2 –hybridised featuring two σ –bonds to the adjacent nitrogen atoms (“pull” stabilisation due to large electronegativity of nitrogen) and an electron lone pair in the remaining sp^2 –hybrid orbital. Two $\pi \text{ N} \rightarrow \pi \text{ C}$ donor interactions from the electron lone pairs on nitrogen into the “empty” p–orbital of the carbene carbon atom complete the electron configuration on the carbene carbon atom (“push” stabilisation) and gives the NHC its stability.

NHCs are always referred as mimes of phosphanes, in particular the electron–rich trialkyl–phosphane, but they NHCs are strong σ –donor and only weak π –acceptor ligands: these two features makes them, usually, better donor lig-

ands than phosphanes and bind stronger to many transition metals than those. The best known NHC possess an imidazole framework with two wingtip groups, one on either nitrogen atom. However, other representatives are known and enjoy rising popularity. Most NHCs are planar, wedge shaped ligands compared to the cone shaped phosphanes. Steric shielding of the metal immediately above and below the ligand plane is somewhat inadequate, but bulky substituents on the imidazole ring can increase the steric bulk of the NHC significantly. The introduction of efficient chirality on the NHC is hampered by the basic structure of the carbene. The necessity of stabilising flanking nitrogen atoms on the carbene centre causes the asymmetric carbon atom on the NHC ligand to be at least three bonds away from the metal compared to just two bonds in the case of phosphanes. Thus, the development of efficient chiral NHC ligands for asymmetric catalysis remains a major challenge.

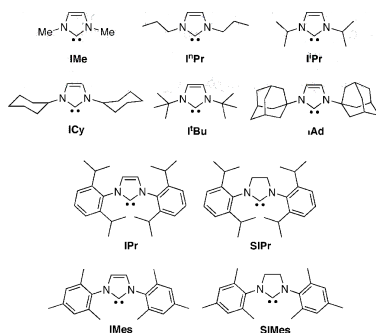


Figure 2.7: Most common NHCs and their abbreviations.

2.2.1 NHCs in Organometallic Chemistry

It is difficult to overemphasize the impact that NHC ligands have had in organic and organometallic chemistry. Less than twenty years have passed since the first report of a stable NHC ligand,[84] and already catalysts containing them can be purchased in industrial scale for a number of rather different chemical transformations such as Pd-catalyzed cross-coupling reactions of various types,[85, 86, 87, 88, 89] hydrosilylation,[89, 90] C-H activation[89, 91, 92] and hydrogenations,[93, 94] Au-catalyzed cyclization of polyunsaturated substrates,[95, 96] Cu-catalyzed borylation reactions,[97, 98] and finally in the Ni-catalyzed dehydrogenation of ammonia-borane H₂. [99] However, Ru-catalyzed metathesis of olefins and alkynes remains the field where the largest impact in the forthcoming years is expected,[79, 100, 101, 102, 103, 104] with applications that span from basic transformations of raw materials in oil refinery and polymer chemistry,[105, 106] as well as from renewable resources,[107, 108] to sophisticated synthesis in the pharmaceutical industry.[109, 110, 111]

This impressive number of applications is possible because NHC ligands are rather flexible architectures whose stereoelectronics can be modified to a large extent, thus giving the chance of an accurate tuning of the catalytic activity. This explains why several groups have dedicated remarkable efforts to their characterization.[112, 113, 114, 115, 116, 117, 118, 119, 120, 121, 122] Focusing on the steric properties, the group of L. Cavallo developed the percent of buried volume, $\%V_{Bur}$, for further informations see Section 2.3, which is the amount of volume in the first coordination sphere of a metal occupied by a given ligand,[123] and several groups have used it to quantify differences between a large series of NHC ligands and even to compare them to classical phosphines.[112, 115, 124, 125, 126] However, all the steric analyses of NHC ligands have been performed on X-ray structures or DFT optimized geometries and, although useful, this approach offers a somewhat limited perspective of the differences between different NHC ligands. Indeed, a series of studies clearly indicated that NHC ligands, due to an intrinsic flexibility around the N-substituent bond, are rather flexible entities and this flexibility can be exploited to achieve better or new performances in catalysis. For example, Cavallo *et al.* related the efficiency in the desymmetrization of achiral trienes of the asymmetric (pre)catalyst **1** of Chart 2.1, developed by Grubbs,[127, 128] to a peculiar folding of the NHC ligand.[129] Based on DFT calculations Cavallo *et al.* proposed that the unsubstituted side of the NHC ligand could be bent toward the halide–Ru–halide plane, and this bending is at the origin of the stereoselective ability of **1**.[129] A conceptually similar strategy was followed by Blechert, that tethered the aromatic N-substituents to the bridge, see (pre)catalyst **2** in Chart 2.1, to impose a folding to the N-substituents with the aim of achieving high diastereoselectivity in ring rearrangement metathesis.[130] Although this strategy showed promising, **2** is of limited stability probably due to C–H activation of the folded down ortho C–H bonds of the N-substituents. A folding of the

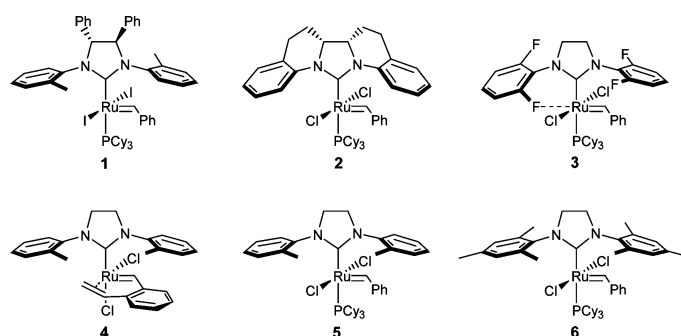


Chart 2.1

N-substituent, not imposed by features of the NHC skeleton as in **1** and **2**, was observed by Grubbs in the X-ray structure of **3** and in the NMR structure of **4**.

In complex 3 the folding of the N-substituent allows one of the ortho-F atom of the NHC ligand to engage in an interaction with the Ru atom, and this interaction was hypothesized to be connected to the higher activity of 3 in a series of metathesis reactions.[131] The folding of the N-tolyl rings in complex 4, instead, allows it to host the bulky C=C moiety cis to the NHC ligand.[132] Interestingly, Grubbs and Goddard proved unambiguously that the substituted side of the o-tolyl rings of 4 is rotated away from the bound olefin (*i.e.* it appears smaller to the substrate). This surprising finding led the authors to suggest that the increased reactivity and ability to react with bulky substrates of (pre)catalysts containing o-tolyl rings, such as 5, with respect to those containing the classical mesityl ring, such as 6, could be due to an increased flexibility around the N-aromatic bond in 5 relative to 6, which provides the substrate an increased accessibility to the metal.[133] These results clearly indicate that the flexibility of NHC ligands around the N-substituent bond is a key parameter that can be used to shape appropriately the space in the first coordination sphere around the metal with practical consequences in terms of catalytic performances (both activity and selectivity).

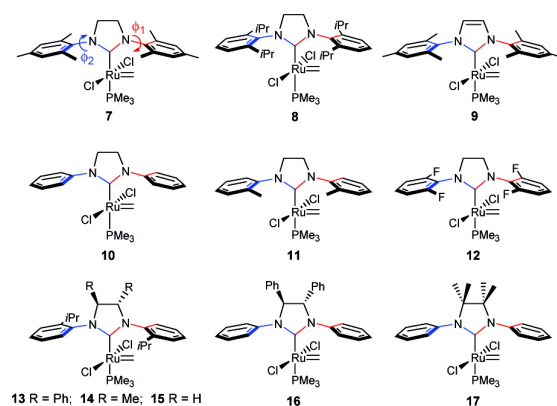
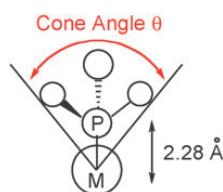


Chart 2.2

2.3 Steric Parameter – % V_{Bur}

Electronic and steric ligand effects both play major roles in organometallic chemistry and consequently in metal-mediated catalysis. Quantifying such parameters is of interest to better understand not only the parameters governing catalyst performance but also reaction mechanisms and also to rationalize experimental results in order to predict future reactivities. The steric parameters, in general, represent the result of changes in molecular properties caused by repulsive forces (usually of the van der Waals type) between parts of a molecule.

As explained above, the NHCs mimic the electron-rich trialkylphosphane. Tolman proposed to measure the size of a ligand by the cone angle θ defined with the metal at the vertex and the atoms at the perimeter of the cone, see Scheme 2.2. For the Tolman's descriptor CPK models can be used with a metal to phosphorus distance of 2.28 Å, the standard Ni–P bond length in $[\text{Ni}(\text{CO})_3(\text{L})]$ complexes. Tertiary phosphine ligands are commonly classified using this parameter, but the method could be applied in principle to any ligand. Nowadays,



Scheme 2.2

ligand molecular architectures are becoming significantly more elaborate – *i.e.* biarylphosphines (Buchwald ligands), bidentate ligands and NHCs – and existing models like the Tolman one have proven difficult and sometimes meaningless. In order to better define the steric pressure brought about by the use of NHC ligands, Nolan and Cavallo proposed an alternate model to measure the NHC steric bulk: the “percent buried volume” ($\%V_{Bur}$) defined as the percent of the total volume of a sphere occupied by a ligand. The sphere has a defined radius and has the metal center at the core.[124, 134] $\%V_{Bur}$ could be calculated using both crystallographic data and optimized structures.

The volume of this sphere represents the first coordination sphere space around the metal occupied by a ligand/ligand fragment. The spatial occupation values of the ligands are obtained using the SambVca (Salerno molecular buried volume calculation) software developed by Cavallo and co-workers that is now available on-line, see below Section 2.3.1. Originally developed to be applied to NHC ligands with examples of ruthenium-, [124] iridium-, [115] palladium-, [135] rhodium-, nickel-, [112] gold-, and silver-NHC complexes, [136] the “percent buried volume” model can be extended to numerous other types of coordination chemistry ligands in order to check the steric hindrance in the first coordination sphere. This descriptor is now well-known in literature and has proven its usefulness in several works.[126, 135, 104, 123, 137, 138, 139]

Calculation of $\%V_{Bur}$ values requires the definition of the metal centre (M) to which the ligand is coordinated. If the structure to be examined is a transition metal complex, it might be natural to use the coordinates of the metal centre as in the structure. In contrast, if the structure of the ligand alone is available, a putative metal centre (M below) to which the NHC ligand is coordinated through the carbene C atom must be defined (Figure 2.8).

Similarly, in the case of phosphanes it is the P atom that is coordinated to the putative metal centre. This descriptor can be also used for a classical η^5 -coordinated Cp-based – in this case it is the centroid of the Cp ring that is coordinated to the putative metal centre – and for polydentate ligands. Looking

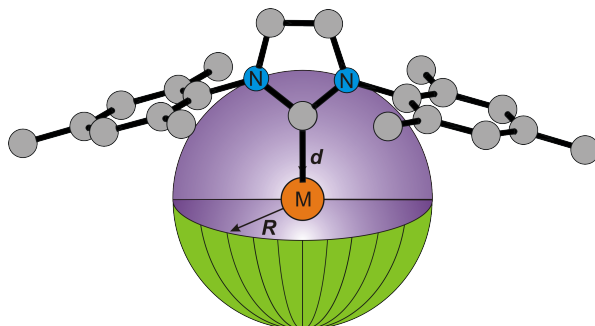


Figure 2.8: % V_{Bur} picture.

at Chart 2.3, the % V_{Bur} increases as a function of the N-substituents bulk (entries a-i). Nonetheless the influence is limited to the close area around the nitrogen. Thus *i*-Pr groups give a similar % V_{Bur} value as cyclohexyl (entries c and f) showing that only the first 2 or 3 atoms connected to the nitrogen atom influence the buried volume of the NHC. According to these values, IPr and SIPr are significantly bigger than IAd (entry i), this could explain why such NHCs usually lead to good results in transition metal catalysis. These results also support literature statements mentioning that the nature (substitution and (un)saturation) of the NHC backbone has a minor impact on its steric properties (entries a-e).[135]

		NHC	Unsaturated	Aromatic	Saturated
	unsaturated	a	18.8	18.9	19.0
	aromatic	b	24.9	25.1	25.4
	saturated	c	26.0	26.4	25.9
R		d	31.1	30.4	31.8
	a	e	35.5	38.9	36.2
	b	f	36.1	40.8	36.6
	c	g	30.5	30.2	31.6
	d	h	30.5	30.2	32.4
	e	i	31.3	30.9	32.3
	f				
	g				
	h				
	i				

Chart 2.3: % V_{Bur} for selected systems.

2.3.1 Web Application Implementation

To measure % V_{Bur} the The SambVca program has been made freely available to the chemical community through a graphical interface on a web application at

the URL <http://www.molnac.unisa.it/OMtools.php>. The application has been developed in a three-layer architecture. The user interface combines several client-side technologies such as HTML, CSS and JavaScript. The web application is PHP script running on Apache web server. Finally, the underlying program logic has been implemented in Fortran and compiled with the Intel Fortran Compiler version 10.1. The main interface is shown in Figure 2.9. Following the 2.9, the user can upload the NHC structure as classical *xyz* for-

SambVca @ MoINaC
A tool to calculate the buried volume of OM ligands

SambVca Manual

Insert your input file

select a demo
simes

upload your file
c3d1 - Chem3D Cartesian 1 format

Browse...

Parameters

Index of the atom coordinated at the center of the sphere

Number of atoms for axis definition

Atom indexes (space separated list)

Sphere radius

Distance from the center of the sphere

Mesh spacing

Include H atoms

Choose radii

Bondi radii

Bondi radii scaled by 1.17

Old set of radii, to be used for backward compatibility

user defined radii

Run SambVca



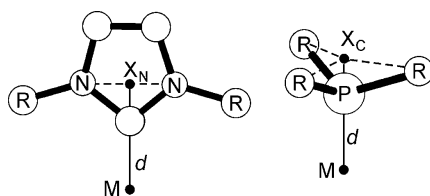
Implementation of this server has received funding from the European Community's Seventh Framework Programme (FP7/2007-2013) under grant agreement No. CP-FP 211468-2 EUMET.

Figure 2.9: Sambuca web page.

mat, CIF and Chem3D Cartesian formats, which are transformed automatically to *xyz* format with the Open Babel 2.1.1 program, openbabel.sourceforge.net. The user needs to provide only the coordinates of the atoms of the NHC, or of any other ligand (new features in development), for which the $\%V_{Bur}$ value has to be calculated. This means that in the case of an organometallic complex the coordinates of all the atoms that do not belong to the NHC ligand must be removed. After upload of the coordinates, the user needs to provide, in the mandatory input windows:

- the sequence number of the atom that coordinates to the metal (the carbene C atom or the P atom in the cases of NHCs or PR_3 , respectively),
- the number of atoms needed to build the additional point (X_N or X_C in Scheme 2.3) to construct the coordination axis (two in the case of the NHCs, three in the case of PR_3), and
- the sequence numbers of the two N atoms (in the case of NHCs) or of the three C atoms bonded to the P atom (in the PR_3 case).

At this point, the user can choose either to accept or to change the default settings (Bondi radii scaled by 1.17 for the atoms, $R = 3.5 \text{ \AA}$ for the radius sphere, and $d = 2.10 \text{ \AA}$ for the distance between the coordinated atom and the putative metal centre, $s = 0.05 \text{ \AA}$ for the mesh spacing). Finally, if H atoms are to be included in the $\%V_{Bur}$ calculation, it is necessary to active the hydrogen.



Scheme 2.3

2.4 Flexibility of NHCs

After this prefaction, a detailed static and dynamics characterization of eleven N-heterocyclic carbenes in Ru-complexes of general formula (NHC)Cl₂Ru=CH₂ will be presented. Analysis of the dynamic trajectories indicates that the nature of the N-substituent can result in extremely different flexibility of the Ru-complexes. In almost all the cases the N-substituent trans to the Ru-ylidene bond is severely folded so that it protects the vacant coordination position at the Ru-center. Limited flexibility is instead associated to the N-substituent on the side of the Ru-ylidene bond. NHCs with a single ortho substituent, either a simple Me or a bulkier *i*-Pr group, have a preferential folding that bends the unsubstituted side of the ring towards the halide-Ru-halide plane. Analysis of the dynamics trajectories in terms of buried volume indicates that the real bulkiness of these systems can be somewhat modulated, and this flexibility is a key feature that allows NHCs to modulate their encumbrance around the metal in order to make room for bulky substrates. Analysis of the buried volume in terms of steric maps illuminated that NHCs with mesityl or 2,6-diisopropylphenyl N-substituents shape quite different reactive pockets. Rather flat with a constant pressure on the halide-Ru-halide plane the former, vault shaped with higher pressure on the sides the latter. As concerns the NHCs with a ortho tolyl or *i*-Pr group on the N-substituent, the steric maps quantify the higher impact of the unsubstituted side of the ligand in the first coordination sphere of the metal, and evidence the overall *C*_S and *C*₂-symmetric reactive pockets of the corresponding complexes. The detailed characterization of the differently shaped reactive pockets is a further conceptual tool that can be used to rationalize the experimentally different performances of catalysts bearing these ligands or to devise new applications.

2.4.1 Computational details – Static calculations

The DFT static calculations were performed at the GGA level with the Gaussian03 package,[140] using the BP86 functional of Becke and Perdew. [14, 141, 142] The electronic configuration of the molecular systems was described with the standard split-valence basis set with a polarization function of Ahlrichs and co-workers for H, C, N, O, P, and Cl (SVP keyword in Gaussian03).[143] For Ru has been used the small-core, quasi-relativistic Stuttgart/Dresden effective core potential, with an associated (8s7p6d)/[6s5p3d] valence basis set contracted according to a (311111/22111/411) scheme (standard SDD keywords in Gaussian03).[144, 145, 146] The geometry optimizations were performed without symmetry constraints, and the characterization of the located stationary points was performed by analytical frequency calculations. Solvent effects in-

cluding contributions of non electrostatic terms have been estimated in single point calculations on the gas phase optimized structures, based on the polarizable continuous solvation model PCM using CH_2Cl_2 as the solvent.[147, 148]

2.4.2 Computational details – Dynamic calculations

The dynamics DFT simulations were performed using the Born–Oppenheimer scheme as implemented in the CP2K Quickstep code.[149] The electronic structure calculations were done at the DFT level using the Perdew–Burke–Ernzerhof exchange and correlation functional.[150] Within CP2K the Kohn–Sham molecular orbitals are described by a linear combination of Gaussian–type orbitals, whereas an auxiliary planewave basis set is employed in order to expand the electron density.[151] A double- ζ basis set with a polarization function, in conjunction with the Goedecker–Teter–Hutter pseudopotentials, was used for all the atoms (standard DZVP–GTH keywords in CP2K).[31] The auxiliary planewave basis set was defined by a cubic box of $20 \times 20 \times 20 \text{ \AA}$ and by an energy cutoff of 300 Ry. The equations of motion were integrated using a timestep of 0.5 fs. The systems were first equilibrated at 300 K for 2 ps in the NVT ensemble, and then systems were sampled for additional 10 ps. $\%V_{Bur}$ calculations. The buried volume calculations were performed with the SambVca package developed by Cavallo and co-workers.[123] The radius of the sphere around the metal center was set to 3.5 \AA , while for the atoms have been adopted the Bondi radii scaled by 1.17, and a mesh of 0.05 \AA was used to scan the sphere for buried voxels. The steric maps were evaluated with a development version of the SambVca package.

2.4.3 Static analysis

This section starts discussing the ϕ_1 and ϕ_2 values in the structure of complexes 7–17 as obtained from a standard geometry optimization. The optimized values are reported in Table 2.1. Have been noted that the optimized ϕ_1 and ϕ_2 values of system 7, bearing the SIMes NHC ligand, are practically equal to 90° , which means that the mesityl rings are perpendicular to the NHC plane. The same occurs for systems 8 and 9, bearing the SIPr and IMes NHC ligands, respectively. Of course, freezing the ϕ_1 and ϕ_2 angles to exactly 90° for 7–9 has no energy consequences. Differently, the ϕ_1 and ϕ_2 angles in the unsubstituted system 10, bearing the SIPh NHC ligand, strongly deviate from 90° with the ϕ_2 angle more coplanar with the NHC ring rather than orthogonal to it. This is a clear consequence of the space available around the vacant coordination position trans to the Ru–ylidene bond, which allows the phenyl N–substituent

to rotate remarkably. Of course, this rotation is prodrome to deactivation reactions through activation of the ortho C–H bonds.^{51,66-67} Forcing either ϕ_1 or $\phi_2 = 90^\circ$ results in structures which are 1.3 and 2.5 kcal/mol higher in energy, respectively, which indicates that the phenyl ring can rotate almost freely. Further, fixing both ϕ_1 and $\phi_2 = 90^\circ$ results in a structure that is 3.4 kcal/mol higher in energy, which indicates that rotations around ϕ_1 and ϕ_2 are not connected. Two Ph substituents on the C4 and C5 atoms of the NHC skeleton,

Table 2.1: Minimized Values of the ϕ_1 and ϕ_2 Angles in Systems 7–17, the Gas-Phase Energies, in kcal/mol, of the same systems in a Geometry in which the ϕ_1 and/or ϕ_2 angles are forced to be equal to 90° , and % V_{Bur} Values. In parenthesis the values in CH_2Cl_2

System	ϕ_1	ϕ_2	$E(\phi_1 = 90^\circ)$	$E(\phi_2 = 90^\circ)$	$E(\phi_1 = \phi_2 = 90^\circ)$	% V_{Bur}
7	91.0	92.2	0.0 (0.0)	0.0 (0.0)	0.0 (0.0)	31.6
8	88.9	93.6	0.0 (0.0)	0.0 (0.1)	0.0 (0.1)	31.9
9	91.5	92.4	0.0 (0.0)	0.0 (0.0)	0.0 (0.0)	30.9
10	134.7	27.0	1.3 (0.1)	2.5 (2.8)	3.4 (3.4)	32.6
11	92.3	113.7	0.0 (0.0)	0.8 (0.7)	0.7 (0.5)	30.6
12	78.0	44.8	0.1 (0.1)	0.9 (0.5)	1.0 (0.6)	34.1
13	66.3	59.0	1.4 (1.4)	2.2 (2.3)	3.9 (3.8)	31.2
14	66.1	60.5	1.0 (0.9)	1.5 (1.6)	2.5 (2.5)	30.8
15	64.2	57.8	1.2 (1.2)	1.9 (2.2)	3.0 (3.0)	30.3
16	66.0	158.5	0.4 (0.1)	2.2 (2.2)	2.7 (2.6)	32.4
17	66.6	69.5	0.2 (0.0)	0.3 (0.3)	0.6 (0.6)	30.4

as in system 16, do not prevent rotation around the N–substituent bonds very effectively, see the quite large deviation of the optimized ϕ_1 and ϕ_2 values for 16, while a better control of these angles is obtained with 4 Me substituents on the NHC skeleton, see system 17. Remarkably, the o-tolyl system 11, bearing the SITol NHC ligand, presents ϕ_1 very close to 90° and ϕ_2 deviating from it by roughly 20° only. This clearly indicates that one single Me ortho substituent is already enough to prevent rotation of the N–substituents, even on the side of the vacant coordination position trans to the Ru–ylidene bond. Nevertheless, as shown by Grubbs and Goddard system 11 is flexible and it is able to rotate more away from a ϕ_1 and $\phi_2 \sim 90^\circ$ when a bulky substrate coordinates to the metal.^{53,68} This underlines the need of a method able to describe properly the flexibility of these complexes. The optimized ortho F substituted system 12 also presents ϕ_1 and ϕ_2 very close to 90° and, in the optimized structure, there is no evidence for a Ru \cdots F interaction that is instead observed in the X-ray structure.⁶⁹ Neither the B3LYP nor the PBE functionals would results in a better agreement with the X-ray structure, but also with these functionals the optimized geometries do not present a Ru \cdots F interaction. Moving to the asymmetric systems 13–15, has been noted that these systems present nearly identical ϕ_1 and ϕ_2 values, deviating by roughly 20° – 30° from 90° , even in the

absence of any substituent on the NHC skeleton. This deviation, which is in line with the X-ray structure of a complex strictly related to 13,48 indicates that the folding of the N-substituents in 13–15 is dictated by steric repulsion between the *i*-Pr substituents and the halides, rather than by repulsion between the *i*-Pr substituents and the substituents on the NHC skeleton. Surprisingly, freezing ϕ_1 or ϕ_2 to 90° costs no more than 2.5 kcal/mol, which indicates that some flexibility around the N-substituent bond is possible also for these systems. Again, the energy of the structure with both ϕ_1 and ϕ_2 fixed to 90° indicates that no correlation between the two angles exist.

2.4.4 Dynamics analysis

In this section have been reported on molecular dynamics simulations performed to get insights on the flexibility of 7–17. The distribution of the ϕ_1 angle for systems 7–17, as obtained by the statistical analysis of the 10 ps molecular dynamics trajectories, is reported Figure 2.10. For the sake of clarity the distribution of systems 7–12, which correspond to systems where the interest is focused on the nature of the N-substituent, are reported in Figure 2.10a, while those of systems 13–17, which are systems that allow to investigate the effect of substituents on the C–C bridge of the NHC ring, are reported in Figure 2.10b. In both cases system 7 is used as reference. Consistently with the static calculations, the ϕ_1 distribution of 7 shows a peak centered at 90° , and the flexibility is substantially restricted to $\pm 15^\circ$. The unsaturated analogous IMes system 9 shows an almost overlapping distribution, indicating that the nature of the NHC skeleton has a limited impact on the flexibility of the ϕ_1 angle. Conversely, the SIPr based system 8 shows a flatter and somewhat broader and jagged peak, which is due to bumping of the *i*-Pr substituents into the halide ligands that makes the ϕ_1 angle to oscillate wildly in the 60° – 120° window. This result indicates that the static calculations offer a limited perspective only. Also unexpected and quite instructive is the behavior of the N-phenyl system 10, with a rather broad ϕ_1 distribution covering the range 30° – 150° and tails almost approaching $\phi_1 = 0^\circ$ or 180° , which correspond to geometries with the phenyl ring almost coplanar with the NHC mean plane. Of course, conformations with $1 \equiv 0$ or 180° are geometrically very suited to interact with the ylidene moiety in a C–H (de)activation reaction.^(51, 66, 67) At this point the attention could be turned to the *o*-tolyl system 11, which in principle should have a behavior intermediate between those of 7 and 10. Instead, the ϕ_1 distribution of 11 is quite peaked, which means that a single Me group on the N-substituent is enough to reduce remarkably the flexibility of this system. Furthermore, the distribution of 11 almost overlaps to that of 7 at higher ϕ_1 values, which indicates that the folding of the substituted side of the *o*-tolyl ring toward the Cl–Ru–Cl plane

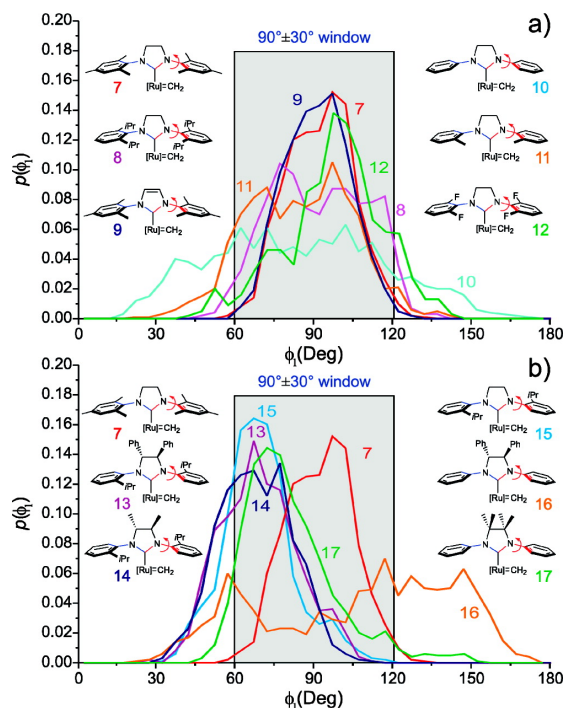


Figure 2.10: Distribution of the ϕ_1 angle for systems 7–17. [Ru] stands for the $\text{Ru}(\text{Cl}_2)(\text{PMe}_3)$ moiety. $\phi_1 = 90$ or -90° corresponds to geometries with the aromatic ring of the N substituent perpendicular to the mean plane of the NHC ring, while $\phi_1 = 0$ or 180° corresponds to geometries with the aromatic ring of the N substituent coplanar with the mean plane of the NHC ring.

is controlled by interactions between the ortho-substituent and the nearby Cl atom. Conversely, the distribution of 11 presents a substantially larger shoulder at low ϕ_1 values, which indicates that the o-tolyl ring can fold more the unsubstituted side toward the Cl–Ru–Cl plane, and this rotation is only hindered by the bumping of the ortho Me group of the tolyl ring into the $-\text{CH}_2-\text{CH}_2$ bridge of the imidazolin ring. This result relates well with the good catalytic performances of 11, since it is a less hindered catalyst than 7, but the limited flexibility relative to 10 prevents it from suffering C–H deactivation reactions. The ortho F system 12 presents a somewhat narrower peak with a shoulder at higher ϕ_1 values, indicating that the F atoms are big enough to prevent almost free rotation as in 10, but they are smaller than a Me group, as in 7, so that some folding can occur.

Now the systems which present some degree of substitution on the $-\text{CH}_2-\text{CH}_2-$ bridge of the imidazolin ring will be treated. The three systems with a single ortho *i*-Pr group, systems 13–15, present a similarly shaped peak roughly centered at 70° , in agreement with the static geometry optimization discussed before, and with the crystallographic structure of a strictly related compound.

This indicates that on moving from a single ortho Me group, system 11, to a single ortho *i*-Pr group, system 15, there is a remarkable change in the flexibility of the ϕ_1 angle. In fact, the shoulder at low ϕ_1 values of 11 is increased into a peak, while conformations at $\phi_1 > 90^\circ$ are simply not accessible. The similar behavior of 13–15 indicates that this substantial change is not related to the presence of substituents on the NHC bridge, and confirms that the driving force that pushes the substituted side of the N–aromatic ligand of 13 and 14 away from the Cl–Ru–Cl plane is the interaction of the *i*-Pr group with the halide ligands. Now 16 and 17 to 10 will be compared. The distribution of 16 is rather flat, as that of 10, but presents a low and broad peak at ϕ_1 values around 120° – 150° . This folds the N–phenyl ring towards the phenyl ring on the NHC bridge, to engage with it in a sort of van der Waals stacking interaction. Differently, 17 shows a rather sharp peak. This indicates that the 4 Me groups on the NHC bridge, beside placing the phenyl N–substituent perpendicular to the NHC ring, restrict remarkably the conformational freedom of the ϕ_1 angle. This reinforces the conclusion that the high stability of 17 is in the difficulty of the ortho C–H bonds of the phenyl rings to undergo C–H (de)activation reactions. The ϕ_2 angle will be dealt; ϕ_2 is the angle around the N–substituent bond opposite to the Ru–methylidene bond, see Figure 2.11. Focusing on 7–12, the ϕ_2 plots show rather broad and overlapping peaks centered around 90° with the only noticeable exceptions of 10 and 11. The former presents a very flat ϕ_2 profile indicating that this phenyl group rotates almost freely. This is different from the phenyl on the side of the Ru–methylidene bond, where the methylidene group prevented free rotation. System 11, instead, presents a well shaped ϕ_2 peak shifted roughly 30° from that of 7–9. This indicates that the corresponding *o*-tolyl ring assumes a preferential conformation that, again, folds the methyl substituted side away from the Cl–Ru–Cl plane. System 12 presents a ϕ_2 peak rather similar to that of 7, which means that the corresponding F–substituted ring, consistently with the static calculations, has no tendency to rotate and engage with the metal in a Ru...F interaction. Moving to 13–17, see Figure 2.11b, it is possible to notice that 13–15 present almost overlapping peaks clearly shifted from 90° . This indicates once more that the presence of substituents on the C4 and C5 atoms of the imidazolin skeleton has no influence on the conformational freedom of the N–substituents, which is instead completely dictated by the single ortho *i*-Pr group. Further support is given by 16, where the Ph substituents on the imidazolin skeleton are substantially unable to lock rotation of the phenyl ring around the ϕ_2 bond. Again, this rotational freedom can be restrained by complete substitution of the imidazolin skeleton, such as in 17, which presents a peak rather similar to that of 7. Finally, the behaviours of the 1 and 2 dihedral angles in the key species of the metathesis reaction have been also investigated, which are the 14e complex from dissociation of the PMe_3 moiety from 7 and the ethene–

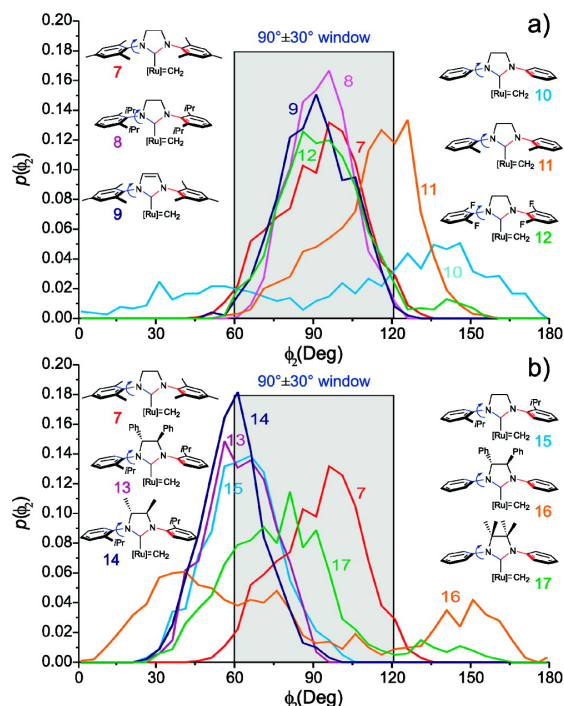


Figure 2.11: Distribution of the ϕ_2 angle for systems 7–17. [Ru] stands for the $\text{Ru}(\text{Cl}_2)(\text{PMe}_3)$ moiety. $\phi_2 = 90$ or -90° corresponds to geometries with the aromatic ring of the N substituent perpendicular to the mean plane of the NHC ring, while $\phi_2 = 0$ or 180° corresponds to geometries with the aromatic ring of the N substituent coplanar with the mean plane of the NHC ring.

coordinated and metallacyclic intermediates. However, the ethene-coordinated intermediate is not stable enough under the above depicted above simulation conditions and very rapidly collapses into the metallacyclic intermediate. This behavior is consistent with the known very low barrier for the metathesis step calculated by several authors. For this reason, the analysis has been restricted to the $14e$ and to the metallacyclic intermediates, and again compared them with the starting (pre)catalysts 7 (see Figure 2.12). The distribution of the 1 angle in the two intermediates strongly resembles that in the (pre)catalyst 7, although that corresponding to the metallacycle is slightly less peaked. Similar small differences are calculated for the distributions of the 2 angle of 7 and of the metallacycle, while that corresponding to the $14e$ intermediate is slightly more peaked. However, the general conclusion is that the 1 and 2 distributions are rather similar in the three key species of olefin metathesis, which is consistent with the previous analysis which suggested the main role of the halide ligands and of the ylide moiety in determining the flexibility of the N substituents of the NHC ligand.

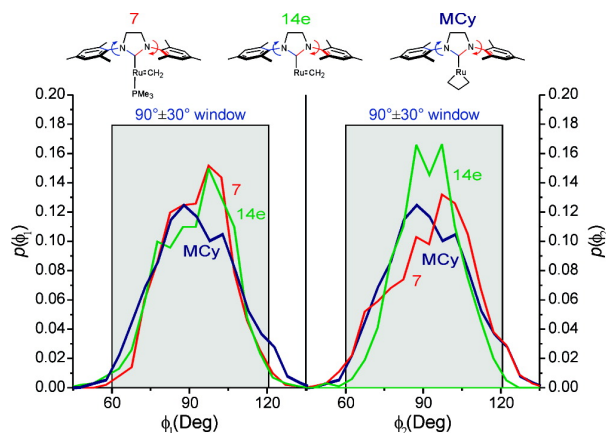
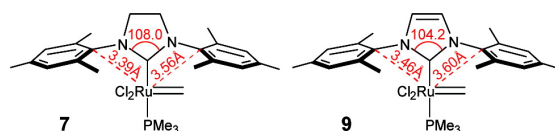


Figure 2.12: Distribution of the ϕ_1 and ϕ_2 angles for the (pre)catalyst, the 14e intermediate, and the metallacycle of system 7

2.4.5 Buried volume analysis

In the previous sections has been shed light on the different flexibility showed by 7–17. However, the analysis did not quantify the impact these differences have in the first coordination sphere of the metal, where reactivity occurs. To clarify this point it is useful the $\%V_{Bur}$ descriptor.[112, 123, 124, 152] The $\%V_{Bur}$ of the NHC ligands in the optimized structure of 7–17 are reported in Table 2.1. In line with the performed analysis of the $\%V_{Bur}$ in the model (NHC)Ir(CO)2Cl systems,[123] the SIMes ligand has a $\%V_{Bur}$ slightly greater than the corresponding unsaturated IMes ligand. This is consequence of the different nature of the NHC skeleton that results in the N–C–N angle being 3.8° greater in the saturated imidazolin ring of the SIMes ligand than in the unsaturated imidazol ring of the IMes ligand (108.0° and 104.2° in SIMes and IMes, respectively).[153] This subtle geometrical difference bends the N–substituent of the saturated NHCs slightly more toward the metal, see the shorter Ru– C_{ipso} distances in Scheme 2.4, thus increasing the steric demand measured by the $\%V_{Bur}$. Beside these two reference systems, the SIPh ligand of 10 shows a



Scheme 2.4

$\%V_{Bur}$ of 32.6, which is greater than that of the SIMes and SIPr based systems 7 and 8. This can be related to the remarkable rotation of the N–substituents that place the phenyl groups almost coplanar to the NHC mean plane. Similar

behavior is shown by 16, consistently with the high folding around ϕ_1 and ϕ_2 . Differently, the tetrasubstituted NHC of 17 shows a $\%V_{Bur}$ of only 30.4, indicating once more the role of the four Me groups on the C4 and C5 substituents of the NHC ring to keep the N-substituent perpendicular to the NHC ring. Thus, the performed analysis is in line with the strategy designed by Grubbs and co-workers to achieve good catalytic performances in the ring closing metathesis of tetrasubstituted olefins: a small N-substituent to accommodate large substrates and a bulky backbone to prevent its rotation, which would reduce stability.[154] Differently from the results on the model (NHC)Ir(CO)₂Cl systems, the SIPr ligand of 8 has a $\%V_{Bur}$ slightly larger than that of the SIMes ligand of 7, although it presents remarkably bulkier *i*-Pr ortho substituents. As concerns the NHCs with a single ortho substituent, the ITol NHC of 11 shows a $\%V_{Bur}$ slightly smaller than that of the SIMes in 7 and of the NHC of 13. This last result is clearly a consequence of the folding of the *i*-Pr substituents away from the halide-Ru-halide plane.

However, the $\%V_{Bur}$ analysis based on static structures does not reflect the flexibility exhibited by the NHC ligands during the molecular dynamics simulations discussed above and highlighted by Grubbs and Goddard.[133] To investigate this point the dynamic trajectories of the most relevant among the systems of Chart 2.2. Namely, 7, 8, 9 and 11, to investigate the effect of the N-substituent, and 10, 13 and 17 to investigate the effect of substituents on the NHC C4-C5 bridge in terms of the $\%V_{Bur}$. The distribution of the $\%V_{Bur}$ of the corresponding NHCs, calculated on the structures collected during the molecular dynamics simulations, are reported in Figure 2.13. Starting from 7 it is clear that the $\%V_{Bur}$ obtained from the geometry optimization only corresponds to the peak of a fairly broad distribution. The $\%V_{Bur}$ of the SIMes in 7 spans easily over the 30-34% range, and the distribution overlaps with those of the other systems. This result gives a completely different perspective of the impact that the SIMes ligand has in the first coordination sphere around the metal, and clearly indicates that even small variations in the geometry of the rather rigid SIMes ligand can have a strong impact in terms of bulkiness.

The $\%V_{Bur}$ distribution of the SIPr in 8 is peaked at higher values and is somewhat broader than that of the SIMes in 7. It also presents a rather long tail at high values evidencing again that normal vibrations of the SIPr ligand, not captured by static methods, have a strong influence on the amount of space this bulky ligand requires. Differently, the distribution of the unsaturated IMes in 9 is shifted at slightly smaller values, consistently with previous analysis that suggested that the unsaturated NHCs are slightly less bulky than the saturated counterparts. As concerns the *o*-tolyl NHC in 11, the distribution is slightly broader and it is peaked at lower values relative to the SIMes in 7, highlighting that the single methyl substitution of the *o*-tolyl N-substituent has a double

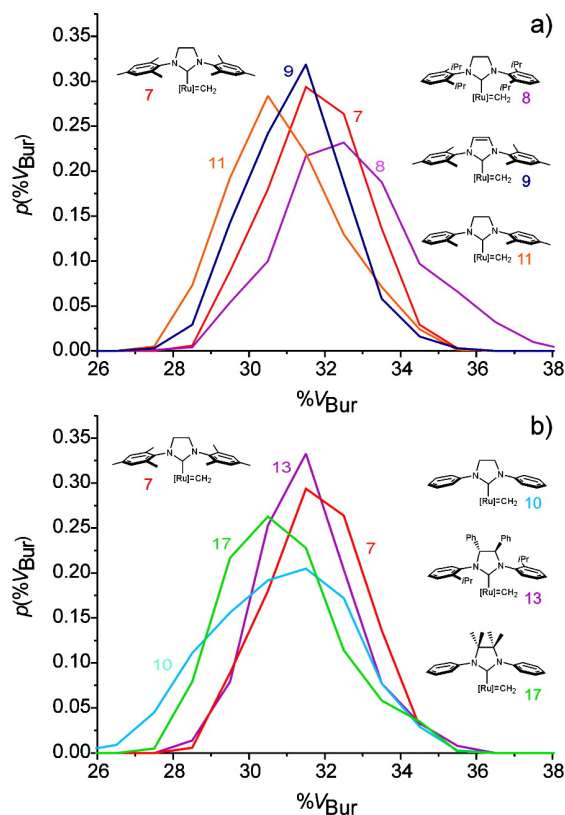


Figure 2.13: Distribution of the $\%V_{Bur}$ for selected systems.

positive effect. It results in a less demanding ligand so that 8 can accommodate bulky substrates better than 7,[133] but it is bulky enough to prevent large rotations around the N–substituent bonds, thus decreasing the rate of deactivation reactions.

Moving to the NHC in 13 and 17, the single *i*-Pr ligand of 13 results in a bulkiness substantially similar to that of the SIMes in 7, with the distribution shifted to slightly lower $\%V_{Bur}$ values, although the complete picture is quite more complicated, see below. Very instructive is instead the comparison between the unsubstituted NHC of 10 and the tetramethyl substituted NHC of 17. The former presents a very broad peak, consistent with the high conformational freedom around the N–substituents bonds, the latter presents a much narrower distribution. In a sense, the tetramethyl substitution confers to 17 a better defined structure, which is a concept that could be useful in the rational design of new ligands with a controlled behavior. The discussion now proceed dissecting the $\%V_{Bur}$ values of some of the most interesting NHCs in terms of quadrants contributions. In a previous paper, Cavallo *et al.* proposed that the

stereoselectivity of 13 could be explained by considering that the folding of the aryl N-substituents could result in a different space occupation of the quadrants around the metal center.[129] The $\%V_{Bur}$ allows to measure this difference. Indeed, the distribution of the $\%V_{Bur}$ in the four quadrants are reported in Figure 2.13 for the representative NHCs of 11 and 13, and for comparison of the parent SIMes NHC of 7. Due to the symmetry of the SIMes ligand the two head quadrants (as well as the two tail quadrants) present identical $\%V_{Bur}$ distributions and thus only the averages have been reported, black lines in Figure 2.13. The tail quadrant is much more buried by the SIMes ligand than the head quadrant, average $\%V_{Bur}$ peaked at roughly 38% and 25%, respectively. This is a clear consequence of the vacant coordination position trans to the Ru-methylidene bond, that allows the NHC ligand to fold back in order to minimize steric interactions with the methylidene group (the $C_{(NHC)}-Ru=CH_2$ angle in 7 is 103.8°). Focusing on the NHC of 11, the asymmetry of the o-tolyl

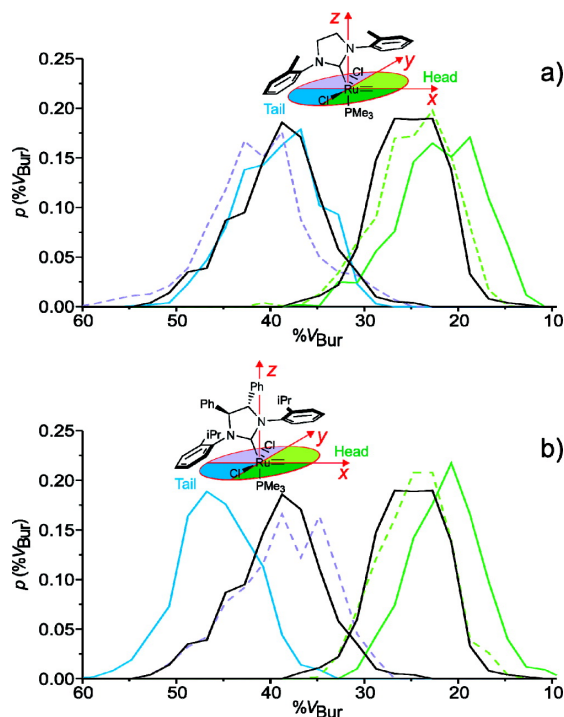


Figure 2.14: Distribution of the $\%V_{Bur}$ values in the quadrants around the metal center for selected systems.

N-substituents splits the $\%V_{Bur}$ peaks, colored lines in Figure 2.13. As a result the peaks corresponding to the substituted side of the o-tolyl rings (pale colored quadrants and dashed lines in Figure 2.13) are shifted to lower values, which means that these quadrants are less encumbered by the NHC ligand and thus are more accessible to bulky substrates. The splitting on both the tail and

the head side is roughly 3–4%, illuminating how small structural differences can have an impact in catalytic performances. Interestingly, on the head side the % V_{Bur} distribution of the unsubstituted part of the *o*-tolyl ring almost overlaps to that of the IMes, consequence of the increased rotation around the ϕ_1 angle. This suggests that similar bulkiness can be obtained by playing with conformational effects (rotation around ϕ_1) rather than substitutional effects (adding a Me group in the ortho position). Moving to the asymmetric NHC of 13 an even more pronounced splitting of the distributions in the head and tail quadrants is observed. Also in this case the less hindered quadrants correspond to *i*-Pr substituted side of the NHC, which is a strong support to the mechanism of stereoselectivity Cavallo *et al.* proposed.[129] Interestingly, the splitting of the % V_{Bur} distributions in the tail quadrants is remarkably high, more than 10%, consistent with a severe folding of the N-substituent on the side of the vacant coordination position at the Ru center. Now into the first coordination sphere of the metal will be envisaged through the steric maps shown in Figure 2.15 for selected systems. The reason for this choice is that the % V_{Bur} descriptor – like the Tolman’s cone angle – measures an average property, while catalysis can be determined by a different distribution of the buried volume in the first coordination sphere of the metal.[155] The steric maps of Figure 2.15 report the value along the *z*-axis at which the NHC ligand starts to bury space in the coordination sphere around the Ru center. Positive values of the isocontour lines refer to the top half-sphere, which is the half sphere where the NHC ligand dwells. The geometries analyzed are the optimized geometries of Table 2.1, and have been aligned as shown in Figure 2.13. Focusing on the SIMes in 7 it is clear the way the tail mesityl group shields the vacant coordination position on the Ru center, see the deep blue area on the left two quadrants in Figure 2.15a. The impact of the head mesityl group in the right zone is less relevant, since it has to compete with the methyldene group for space. Nevertheless, the broad pale yellow area at 1.00–1.25 Å indicates that the mesityl ring is able to impart a noticeable steric pressure on the methyldene, particularly through the ipso and ortho C atoms, see the pale green imprints of these atoms in Figure 2.15a. The ortho methyl groups of the mesityl ring have a small impact at the borders of the coordination sphere. Quite interesting is the comparison between the SIMes and the SIPr in 7 and 8, see Figure 2.15a and b. The bulkier ortho *i*-Pr groups of the head N-substituent have a much stronger influence at the border of the coordination sphere, see the pale blue areas. To relieve the steric interaction between these groups and the halide atoms the SIPr ligand is slightly pushed away. Consequently, the steric pressure on the central zone, where the Ru-methyldene bond is placed, is less encumbered by the SIPr rather than the SIMes ligand. This is clearly indicated by the absence of the pale green spots corresponding to the ortho C atoms of the ring in Figure 2.15b. In short, de-

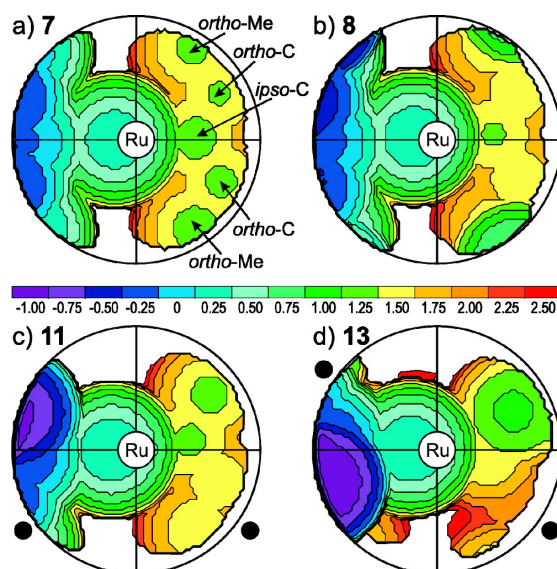


Figure 2.15: $\%V_{Bur}$ maps of the NHC in the optimized geometries of (a) 7, (b) 8, (c) 11, and (d) 13. The spots corresponding to the ortho and ipso C atoms of the mesityl ring and of the *o*-methyl substituents of 7 are indicated by arrows. The quadrants occupied by the *o*-methyl and *o*-isopropyl substituents in 11 and 13 are indicated by a black dot. The coloring scale of the isocontour levels, in Å is also reported

spite the similar $\%V_{Bur}$ the two ligands shape a remarkably different reactive pocket. Quite flat and with a constant pressure the SIMes ligand, vault shaped with higher steric pressure at the border the SIPr ligand. These differences, which cannot be captured by the simple $\%V_{Bur}$ descriptor, since it measures an average property, could contribute to the remarkable catalytic differences exhibited by the corresponding complexes. Focusing on the *o*-tolyl NHC of 11 small differences with respect to the SIMes of 7 also emerge. First, the space available on the bottom-left tail quadrant, which corresponds to the unsubstituted side of the *o*-tolyl ring, is more hindered than the top-left quadrant, which corresponds to the substituted side of the ring. Further, the bottom-left quadrant is also more hindered than the analogous quadrant in the SIMes of 7, see the deep violet area in Figure 2.15c. Similar asymmetry can be appreciated in the right head quadrants, and again the bottom one is more buried with the imprint of the ortho C atom visible, whereas in the top quadrant, which correspond to the substituted side of the *o*-tolyl ring, there is no trace of both the ortho C atom and its Me substituent.

Moving to the asymmetric NHC of 13 the peculiar folding and the asymmetry of the catalyst can be appreciated in full. The steric map is asymmetric both in the tail (left) and head (right) quadrants. In both cases the less encumbered quadrants are those occupied by the *i*-Pr substituted side of the N-substituents.

The unsubstituted side of the N-substituent in the tail quadrants has an imprint similar to that of the o-tolyl ring in 11, compare the similar purple areas in Figure 2.15c and Figure 2.15d, whereas in the head quadrants the asymmetric NHC of 13 has a much greater impact, note the large green spot corresponding to the ortho C atom in the bottom-right quadrant of Figure 5d. This clearly indicates that a substrate will prefer to coordinate to the Ru center (trans to the NHC) in such a way that bulkiness is placed in the *i*-Pr quadrants. This analysis supports the mechanism Cavallo *et al.* proposed to rationalize the stereoselectivity in the desymmetrization of achiral trienes by 13.[129] Finally, it is interesting to note that the o-tolyl NHC in 11 presents a rough C_S -symmetric map, with the two bottom quadrants more hindered, whereas the asymmetric NHC in 13 presents a rough C_2 -symmetric map, with the top-left and bottom-right quadrants more hindered. This can be qualitatively related to the rather good ability of the o-tolyl system to form cis-olefins, and supports the proposed explanation of the higher enantiomeric excesses observed experimentally in the asymmetric ring closing metathesis of E-olefins relative to the Z isomer.[129, 127]

2.4.6 Analysis of free NHCs

In this last section some features of free NHCs will be discussed, starting with the energy profile around one of the ϕ angles for some of the most typical and uncoordinated NHCs ligands, see Figure 2.16. The NHCs have been chosen in order to exploit the effect of ortho Me substituents and the nature of the NHC ring (saturated or unsaturated). The first result is that the two NHCs with phenyl N-substituents prefer a planar geometry with the phenyl ring coplanar with the the NHC ring, see the minima at $\phi = 0^\circ$ and 180° for the IPh and SIPh curves in Figure 2.16. The geometry with the phenyl ring almost perpendicular to the NHC ring are roughly 3 and 6 kcal/mol higher in energy for IPh and SIPh, respectively, see the maxima at $\phi = 90^\circ$ and -90° . Of course, the planar geometry is destabilized by steric repulsion between the NHC and the phenyl rings, but this destabilization is more than compensated by conjugation of the high energy π orbitals of the NHC ring with the aromatic ring of the N-substituents. The balance between these two effects rationalizes the various systems. Indeed, the presence of a single ortho Me group introduces additional steric destabilization to the planar geometry, so that the energy curves of the SITol and ITol are flatter and, in the case of the ITol, the in plane geometry is not the most stable. Finally, the SIMes and IMes prefer a geometry with the mesityl rings almost perpendicular to the NHC ring, see the double shallow minima around $\phi = 90^\circ$ and -90° in their curves in Figure 2.16. The curves corresponding to saturated imidazolin NHCs are roughly 2–3 kcal/mol higher than those of the analogous

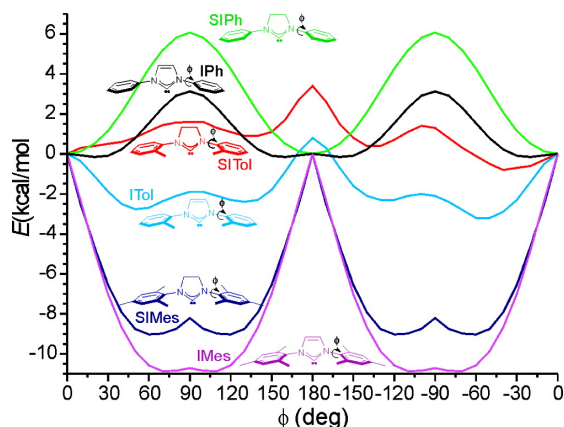


Figure 2.16: Energy profile around the ϕ_1 angle in selected free NHCs.

unsaturated imidazol NHC around $\phi = 90^\circ$ and -90° . This increased preference for the planar geometry in the case of the saturated NHCs can be ascribed to the different π orbital scheme between saturated and unsaturated NHCs. In the latter class the π orbitals of the N–C–N moiety are already stabilized by conjugation with the π orbitals of the unsaturated C4=C5 bond, whereas in the former class not. Incidentally, the different nature of the NHC skeleton has been also related to the higher tendency of saturated NHCs to dimerize.[126] Finally, the asymmetric NHC ligand 13 can exist in the two limit isomers with the *i*-Pr groups away (anti) from the nearby Ph groups, as in the X-ray structure, or with the both the *i*-Pr groups on the same side (syn) of the Ph groups. Surprisingly, the syn isomer is more stable than the anti isomer both in the gas phase and in CH_2Cl_2 , by 2.3 and 0.3 kcal/mol, respectively. Said that the isomerization pathway connecting them has been explored, see Figure 2.17. The barriers

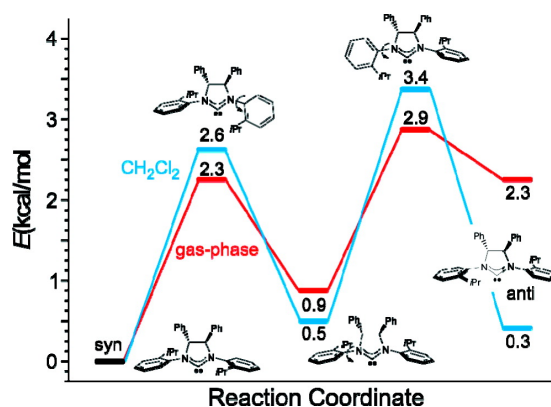


Figure 2.17: Isomerization pathway connecting the syn and the anti isomers.

separating the syn and anti isomers are roughly 3 kcal/mol, which indicates

a rapid equilibrium between the two isomers, and the small preference for the syn isomer indicates that both isomers are abundantly present in solution. The slightly higher stability of the syn isomer can be easily rationalized by visual inspection of the structures reported in Figure 2.18. In both isomers the Ph rings on the NHC skeleton push the nearby side of the aromatic ring of the N-substituent toward the carbonyl C atom. In the anti isomer this corresponds to fold the *i*-Pr substituents toward the NHC backbone, while in the syn isomer the *i*-Pr groups are folded in a unhindered region, which corresponds to reduced steric stress in the syn isomer. However, after complexation to the Ru

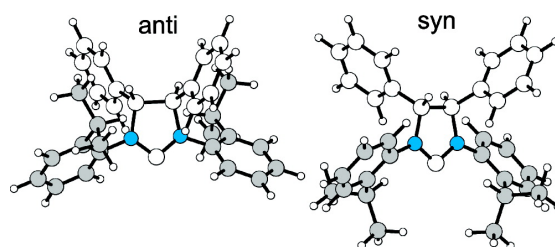


Figure 2.18: Optimized structure of the anti and syn isomers of the NHC of 13.

center the syn isomer of 13 is 7.2 kcal/mol higher in energy than the anti isomer of Chart 2.2, due to steric clashes of the folded down *i*-Pr groups and the Cl ligand. This suggests that complexation to the metal occurs only (or faster) with the slightly less stable anti isomer of the free NHC, while the abundant syn isomer is probably unable (or slower) to be trapped by the metal. Removal of the free anti isomer of the NHC shifts the syn/anti equilibrium toward the anti isomer until it is quantitatively trapped by metal.

2.4.7 Summary

Here has been presented a detailed static and dynamics characterization of a large set of NHCs ligands in Ru-complexes. These analysis indicated that the nature of the N-substituent can result in extremely different flexibility of the Ru-complexes. In almost all the cases the N-substituent trans to the Ru-ylidene bond is severely folded in such a way that it protects the vacant coordination position at the Ru-center, while somewhat limited flexibility is associated to the N-substituent on the side of the Ru-ylidene bond. The phenyl N-substituent can rotate almost freely, whereas rotation of the mesityl (or greater) N-substituents is quite restricted. Results for the *o*-tolyl N-substituent indicate that one single ortho-group on the N-substituent is already enough to restrict remarkably flexibility. Two phenyl substituents on the C4-C5 are not enough to freeze phenyl N-substituents, while four methyl substituents freeze it. In agreement with

previous results NHCs with a single ortho-substituent, either a simple Me or a bulkier *i*-Pr, have a preferential folding that bends the unsubstituted side of the ring towards the halide-Ru-halide plane. Analysis of the dynamics trajectories in terms of the $\%V_{Bur}$ indicated that the real bulkiness of these systems at work can be somewhat modulated. This increased flexibility, which cannot be captured by static experimental or theoretical approaches such as X-ray or geometry optimizations, is instead fully captured and for the first time evidenced by the presented dynamics approach. In short, the results indicate that the flexibility around the N-substituent bond is a key feature, so far underestimated, that allows NHCs to modulate their encumbrance around the metal in order to make room for bulky substrates.

Analysis of the $\%V_{Bur}$ of the optimized structures in terms of steric maps illuminated the real impact of the NHC ligands in the first coordination sphere of the metal, which is the place where catalysis occurs. The comparative maps of the systems with mesityl and 2,6-diisopropylbenzene N-substituents indicated that they shape rather different reactive pockets. Rather flat with a constant pressure on the halide-Ru-halide plane the former, vault-shaped with higher pressure on the side and lower pressure on the middle the latter. As concerns the NHCs with a *o*-tolyl or a *o*-isopropyl group on the N-substituent, the steric maps quantify the higher impact of the unsubstituted side of the ligand in the first coordination sphere of the metal, and evidence the overall C_S and C_2 -symmetric reactive pockets of the corresponding complexes. This detailed characterization of the differently shaped reactive pockets is a further conceptual tool that can be used to rationalize the experimentally different performances of catalysts bearing these ligands or to devise new applications. Finally, the Ru-complexes that have been investigated here are relevant as (pre)catalysts for olefin metathesis. However, it is reasonable that the emerged behavior can be easily extended to NHC ligands in almost any NHC-transition metal complex, with a particular emphasis on those able to promote catalytic activity for a broad spectrum of different applications.

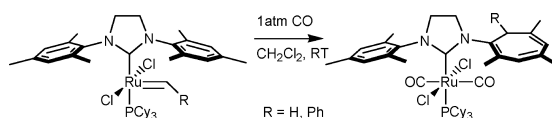
2.5 Deactivation of NHC bearing Ru Catalysts by Lewis acids

In this section the reactivity induced by coordination of a CO molecule trans to the Ru–ylidene bond of a prototype Ru–olefin metathesis catalyst bearing the NHC ligand SIMes will be explored. Static DFT calculations indicate that CO binding to the Ru center promotes a cascade of reactions with very low energy barriers that lead to the final crystallographically characterized product, in which the original methylidene group has attacked the proximal aromatic ring of the SIMes ligand leading to a cycloheptatriene through a Buchner ring expansion. Analysis of the relevant molecular orbitals, supported by *ab initio* molecular dynamics simulations, illuminate the key role of the π -acid CO coordinated trans to the Ru–methylidene bond to promote this reactivity. Based on this result, a large set of π -acid groups could promote this deactivating reaction have been investigated. Results clearly indicate that almost any sufficiently π -acidic group that can approach the Ru center in the sterically crowded position trans to the Ru–methylidene bond can promote this deactivation route.

Unfortunately, stability remains an issue, and little is known about deactivation pathways, although work in this challenging area is increasing. [156, 157, 158, 159, 160, 161, 162, 163, 164, 62, 165] Broadly speaking, deactivation pathways are those chemical transformations of the (pre)catalyst or the active species that remove them from productive metathesis. In this sense, Diver, Feistier, and co-workers [156, 157, 157] have clearly shown that addition of π acids such as CO or isocyanides to a solution of typical second-generation catalysts can switch a metathesis catalyst into a cyclopropanation catalyst, [166, 167, 168, 169, 170, 171] by activating the Ru–ylidene bond to a carbene-like reactivity. This promotes ylidene attack to the proximal N-bonded aromatic ring of the NHC ligand, which results in a Buchner type ring expansion reaction; see Scheme 2.5. Although it is difficult to call the reaction of Scheme 2.5 a deactivation reaction, since CO is not normally added during metathesis, understanding the chemistry behind this transformation is relevant for the following reasons

- π -Acids are inevitably present during metathesis, and any organometallic textbook presents educative comparisons between the σ -basic/ π -acid properties of CO, olefins and phosphines. Clearly, olefins and phosphines are much weaker π -acids than CO, but a reduced acidity could still induce slow deactivation reactions as those shown in Scheme 2.5 for CO.
- A clear understanding of the changes in the chemical behavior promoted by a σ -basic/ π -acid ligand trans to the Ru–ylidene bond would expand

the present knowledge of the chemistry of Ru-based catalysts with possible consequences in the design of new ligands with tuned properties.



Scheme 2.5

Indeed, the position trans to the Ru-ylidene bond has been scarcely considered during the years.[172, 173, 174, 175] For example, Grubbs and co-workers have suggested that one of the ortho-F atoms of the NHC A shown in Chart 2.4 could be engaged in an interaction with the Ru center that results in increased metathesis activity.[131] Furthermore, strategies for the synthesis of pre-catalysts having labile ligands that could result in more stable and active catalysts, such as B and C of Chart 2.4, are explored.[175] For these reasons the reactivity changes induced by a series of σ -basic/ π -acid ligands coordinated trans to the Ru-methylidene bond of the systems shown in Chart 2.5 have been computationally investigated. Such a systematic comparison should increase the under-

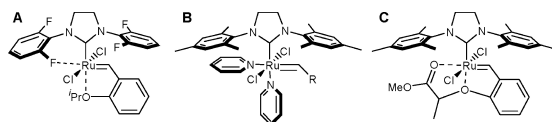


Chart 2.4

standing of the basic properties of the Ru-ylidene bond and of the reactivity changes that could in principle be induced by changes in the nature of the ligands connected to the Ru atom. Most of the calculations reported here are based on a classical static density functional theory (DFT) approach, but a DFT based *ab initio* molecular dynamics (AIMD) simulation have been also performed: this offers the invaluable opportunity to capture the time evolution of the reactive species.[176, 177]

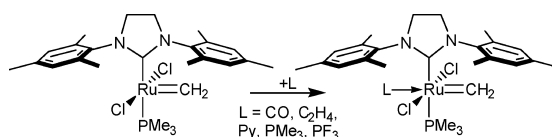


Chart 2.5

2.5.1 Computational details – Static calculations

All the DFT static calculations were performed at the GGA level with the Gaussian03 set of programs,[140] using the BP86 functional of Becke and Perdew.[14, 141, 142] The electronic configuration of the molecular systems was described with the standard split-valence basis set with a polarization function of Ahlrichs and co-workers for H, C, N, O, P, F, and Cl (SVP keyword in Gaussian03).[143] For Ru the small-core, quasi-relativistic Stuttgart/Dresden effective core potential, with an associated (8s7p6d)/[6s5p3d] valence basis set contracted according to a (311111/22111/411) scheme (standard SDD keywords in Gaussian03) has been used.[144, 145, 146] The geometry optimizations were performed without symmetry constraints, and the characterization of the located stationary points was performed by analytical frequency calculations. Solvent effects including contributions of nonelectrostatic terms have been estimated in single-point calculations on the gas phase optimized structures, based on the polarizable continuous solvation model PCM using CH_2Cl_2 as a solvent.[147, 148] In conclusion, the energies reported correspond to the “Total free energy in solution: with all non electrostatic terms” value in the Gaussian03 output.

The electrophilicity of the complexes was evaluated as the Parr electrophilicity index shown in equation 2.1:[178]

$$\omega = \frac{\mu}{2\eta} \quad (2.1)$$

where μ and η are the chemical potential and the molecular hardness, respectively. In the framework of DFT,[179] μ and η for a N-electron system with total electronic energy E and subject to an external potential are defined as the first and second derivatives of the energy with respect to N at a fixed external potential.[180, 181, 182] In numerical applications, μ and η are approximated with the finite difference formulas of equation 2.2, which are based on Koopmans’ theorem,[183]

$$\mu \cong \frac{1}{2}(\varepsilon_L + \varepsilon_H), \quad \eta \cong \frac{1}{2}(\varepsilon_L - \varepsilon_H) \quad (2.2)$$

where ε_H and ε_L are the energies of the highest occupied molecular orbital (HOMO) and the lowest unoccupied molecular orbital (LUMO), respectively. The strength of the Ru-ylidene bond was evaluated with the Mayer Bond Order (MBO),[184, 185] which is a valuable tool in the analysis of the bonding in main group compounds and has been also used to characterize transition metal systems.[186, 187, 188, 189, 190, 191, 190, 192, 193] Finally, in some cases the change in the local aromaticity of a given ring will be discussed. As a structure-based measure, the Kruszewski and Krygowski harmonic oscillator model of

aromaticity (HOMA) index has been used; see equation 2.3:[194]

$$\text{HOMA} = 1 - \frac{\alpha}{n} \sum_{i=1}^n (R_{opt} - R_i)^2 \quad (2.3)$$

where n is the number of bonds considered, R_i are the bond lengths, and α is an empirical constant (for C–C bonds $\alpha = 257.7$) fixed to give HOMA = 0 for a model non-aromatic system and HOMA = 1 for a system with all the bonds equal to their optimal value R_{opt} , which is 1.388 Å for C–C bonds (*i.e.*, the bond length in fully aromatic systems).

2.5.2 Computational details – Dynamic calculations

The AIMD simulations were performed using the Born–Oppenheimer scheme as implemented in the CP2K Quickstep code.[?] The electronic structure calculations were done at the DFT level using the Perdew–Burke–Ernzerhof exchange and correlation functional.[142] Within CP2K the Kohn–Sham molecular orbitals are described by a linear combination of Gaussian–type orbitals, whereas an auxiliary plane-wave basis set is employed to expand the electron density.[151] A double- ζ basis set with a polarization function,20,24 in conjunction with the Goedecker–Teter–Hutter pseudopotentials,[31] was used for all the atoms (standard DZVP–GTH in CP2K). The auxiliary plane-wave basis set was defined by a cubic box of $20 \times 20 \times 20 \text{ \AA}^3$ and by an energy cutoff of 300 Ry. The equations of motion were integrated using a time step of 0.5 fs. A harmonic constraint centered at 3.0 Å with a force constant of 15 kcal/mol was applied on the Ru–CO distance, and the system was equilibrated for 0.5 ps by imposing that the temperature was held within 300 K (± 10 K by rescaling atomic velocities). After equilibration the system was sampled in the NVE ensemble for 5 ps. After the first picosecond, the constraint on the Ru–CO distance was removed and the system was allowed to evolve freely.

2.5.3 Results

The argumentation starts discussing the effect of a CO molecule coordinated trans to the Ru=CH₂ bond, since clean experimental data are available for this system. Starting from precatalyst 1a, the first step corresponds to coordination of a CO molecule to the vacant coordination position trans to the Ru=CH₂ bond. The binding energy of the CO molecule to the Ru atom in 2a is 22.5 kcal/mol. Coordination of the CO molecule has a strong effect on the Ru=CH₂ bond, which elongates from 1.81 Å in 1a to 1.92 Å in 2a, and pushes the phosphine almost perfectly trans to the NHC ligand, with a small elongation (less than

0.04 Å) of the Ru–NHC and Ru–P bonds. CO coordination also results in the remarkable reduction of the NHC–Ru=CH₂ angle from 103.9° in 1a to 93.9° in 2a, thus increasing the proximity of the reactive methyldene group with the proximal aromatic ring of the SIMes ligand (the C_{methyldene}–C_{ipso} distance reduces from 3.56 to 2.62 Å).

At this point, the cyclopropanation reaction between the methyldene group and one of the C_{ipso}–C_{ortho} bonds of the nearby mesityl ring occurs in two steps. The former corresponds to attack of the methyldene group to the C_{ipso} atom, which requires overcoming the negligible barrier of 0.7 kcal/mol and leads to 3a, which still presents a Ru–CH₂ bond and is only 3.7 kcal/mol more stable than 2a (Figure 2.19). The second step of the cyclopropanation reaction requires the complete rupture of the Ru–CH₂ bond with the concerted formation of a cyclopropane ring by attack of the C_{methyldene} atom to one of the C_{ortho} atoms of the mesityl ring. This step requires overcoming a barrier of 0.3 kcal/mol only, after which the system collapses into the quite stable intermediate 4a, 15.0 kcal/mol below the CO coordinates species 2a. Intermediate 4a presents a vacant coordination position trans to the CO. Analysis of the Mayer bond orders indicated that transition state [2a–3a] is highly concerted, since the bond orders of the breaking π Ru–C_{methyldene} bond and of the forming C_{methyldene}–C_{ipso} bond in transition state [2a–3a] are halfway (0.99 and 0.53, respectively) between the values in 2a (1.48 and 0.14) and 3a (0.60 and 0.91). Conversely, [3a–4a] can be classified as an early transition state, since the bond orders of the breaking σ Ru–C_{methyldene} bond and of the forming C_{methyldene}–C_{ortho} bond in [3a–4a] (0.56 and 0.23, respectively) are clearly closer to the values in 2a (0.60 and 0.15) than in 3a (0.17, 0.87). Overall, considering the rather small energy barriers associated with the 2a \rightarrow 3a and 3a \rightarrow 4a steps, it is reasonable to hypothesize that kinetically formation of the cyclopropane intermediate 4a, after CO coordination, occurs in a single step from 2a down to 4a. Coordination of a second CO molecule to 4a is a barrierless process and leads to intermediate 5a. The binding energy of the second CO molecule, 20.4 kcal/mol, is comparable to the binding energy of the first CO in 2a, 22.5 kcal/mol. At this point, the only step needed to form the experimentally observed product is the opening of the C_{ipso}–C_{ortho} bond of the tensioned cyclopropane ring of 5a, which leads to product 6a, overcoming yet another small energy barrier, 0.8 kcal/mol in this case. The cyclopropane opening in the absence of a second CO molecule coordinated to the Ru atom has been also examined. In this case the somewhat larger barrier of 4.2 kcal/mol must be passed, after which the system collapses into intermediate 7a. After the cyclopropane ring is opened, coordination of a second CO molecule leads to the final product 6a. Considering the small energy barrier for the 4a \rightarrow 7a step, it is possible that coordination of the second CO molecule occurs after the ring expansion step. Product 6a, shown in Fig-

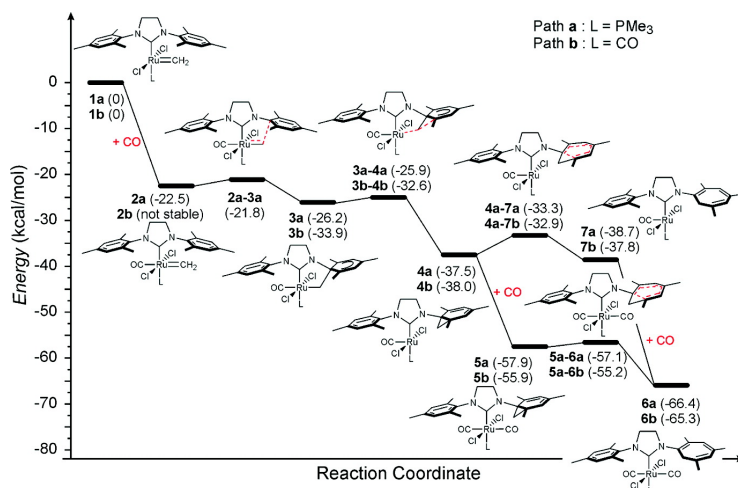


Figure 2.19: Energy diagram of the complete 1 to 6 deactivation pathway. In parentheses is the energy of the various species, in kcal/mol, relative to the pre-catalyst 1a.



Figure 2.20: Kinetic trans (6a) and thermodynamic cis (6a-cis) isomers of the decomposition product.

ure 2.20, is the only species for which X-ray data are available. Geometrical analysis indicates that the computed structure is in excellent agreement with the crystallographic structure, with a rmsd of 0.032 Å for distances and of 0.8° for angles.[†] This also indicates that the sterically demanding PCy₃ phosphine can be safely replaced with the less bulkier PMe₃ phosphine to shed light on this kind of reactions. As suggested by Diver and co-workers, alternative geometries for 6a have been explored, since complexes of generic formula Ru(CO)₂X₂L₂ (where X is a halide or pseudo-halide and L is a neutral donor ligand) usually present a stable Ru(cis-CO)₂(cis-X)₂(trans-L)₂ geometry.[195, 196] Four different isomers with a cis-CO and cis-Cl geometry are possible, since the NHC ligand is C₁ symmetric after formation of the seven-member cycle. All of them are roughly 10 kcal/mol lower in energy than the trans isomer 6a, with the most stable isomer, 6a-cis shown in Figure 2, 10.4 kcal/mol more stable than 6a. These results support the hypothesis of Diver and co-workers that 6a corresponds to the kinetic product of the reaction 6 and that isomerization between the trans and cis isomers is not an easy process. The reaction pathway when the phosphine of precatalyst 1a is substituted by a CO molecule leading to 1b is also shown in Figure 2.19. Energetically, substitution of PMe₃ with CO is almost thermoneutral, since the CO binding energy is only 1.3 kcal/mol larger than that of PMe₃, although this substitution probably requires dissociation of PMe₃ from 1a, which costs 27.8 kcal/mol. Coordination of a second CO molecule trans to the Ru-methylidene bond of 1b does not lead to an intermediate analogous to 2a. Instead, all the geometry optimizations that have been tried inevitably collapsed into species 3b, in which the C_{methylidene}-C_{ipso} bond is already formed. Beside this difference, the energy profile with a CO molecule trans to the NHC ligand (path b in Figure 2.19) is rather similar to that with a PMe₃ molecule trans to the NHC ligand (path a in Figure 2.19). Our inability to locate intermediate 2b indicates that the CO molecule trans to the NHC ligand contributes to weaken the Ru-ylidene bond, activating it toward the proximal mesityl ring. Considering the relative size of the PMe₃ and CO ligands in 1a and 1b, it is clear that the effect of the second CO ligand is almost entirely electronic in nature. The activating effect of the CO coordinated trans to the NHC ligand is also evidenced by the increase of the Parr electrophilicity index,[148, 147, 197, 198] which increases from 112.1 in 1a to 174.7 kcal/mol in 1b. However it is coordination of a CO molecule trans to the Ru-ylidene bond the key factor facilitating attack of the methylidene group to the proximal mesityl ring. This point is reinforced by observing that the aromaticity of this

[†]Standard deviations for distances and angles:

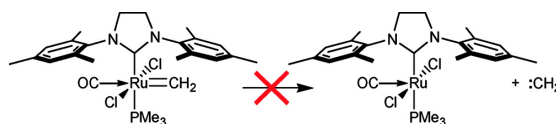
$$S_{n-1} = \frac{\sum_{i=1}^N (CV - EV)}{N - 1}$$

where *CV* stands for calculated value, *EV* experimental value (X-ray data), and *N* is the number of distances or angles taken into account

mesityl ring is comparable in 1a and 1b, as indicated by very similar HOMA indexes, 0.834 and 0.838, respectively.

2.5.4 Results and Discussion

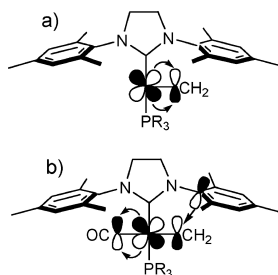
As already indicated, methyldiene attack to one of the aromatic rings of the SIMes ligand with formation of a cycloheptatriene type ring corresponds to a classical Buchner ring expansion reaction. To understand the chemistry behind this reaction, the possibility that CO coordination could induce the release of a free carbene was tested at the beginning, as shown in Scheme 2.6. However, the reaction of Scheme 2.6 is endoergonic by 40.7 kcal/mol, which rules out this possibility and is in agreement with the experimental non-detection of regioisomers due to remote cyclopropanation of aromatic π -bonds, as could occur in the presence of free carbene.[156] To rationalize the activation role of



Scheme 2.6

the CO, Diver and co-workers suggested that CO binding may weaken π -back-bonding between the Ru atom and the ylidene ligand, making the latter more electrophilic and disengaging it from the metal center. To verify this hypothesis, a comparative molecular orbital (MO) analysis of complexes 1a and 2a have been performed. Results can be summarized considering the MO diagram reported in Scheme 2.7. In the precatalyst 1a the classical Fischer carbene bonding scheme is established.[199] Electron density is donated from filled d orbitals on the Ru to the empty π orbital of the methyldiene. Differently, in the presence of the strong π -acid CO molecule, electron density from the Ru is more strongly donated to π -acid MOs of the CO. As suggested by Diver, this depletes electron density from the π orbital of the methyldiene, which is able to accept from the properly oriented π orbital of the C_{ipso} atom of the proximal ring, resulting in a very low barrier for formation of the $C_{\text{methylidene}}-C_{\text{ipso}}$ bond. Natural bond order (NBO) analysis of the $\text{Ru}-C_{\text{methylidene}}$ bond supports this view. In fact, in species 1a the MO corresponding to the π $\text{Ru}-C_{\text{methylidene}}$ bond is 62% Ru and 38% $C_{\text{methylidene}}$. After CO coordination, which is in 1b, this MO becomes 75% Ru and 25% $C_{\text{methylidene}}$. Interestingly, a similar analysis of the σ $\text{Ru}-C_{\text{methylidene}}$ bond indicates that in 1a this bond is 47% Ru and 53% $C_{\text{methylidene}}$, while in 1b (due to the strong trans effect of the CO) this MO becomes 35% Ru and 65% $C_{\text{methylidene}}$. In short, after CO coordination the methyldiene has greater “free-carbene” character. Consequently, in the 3a

of 4a step the $C_{\text{methylidene}}$ atom is able to attack with a low energy barrier one of the C_{ortho} atoms of the N-bonded ring that, incidentally, is also activated by the loss of aromaticity after formation of the $C_{\text{methylidene}}-C_{\text{ipso}}$ bond. Other evidence of the incipient interaction between the π -orbitals of the methylidene C atom and of the C_{ipso} atom of the proximal mesityl ring is the decrease of the HOMA index of this mesityl ring that drops from 0.834 in 1a to 0.787 in 2a and the decrease of the Mayer Bond Order of the $\text{Ru}=\text{CH}_2$ bond that drops from 2.015 in 1a to 1.479 in 2a. The chemical consequence of this interaction is in the higher reactivity of 2a with respect to 1a, as indicated by the increase of the Parr electrophilicity index,[148, 147, 197, 198] from 112.1 kcal/mol in 1a to 212.1 kcal/mol in 2a. This change in electrophilicity is a consequence of the increased stability of the LUMO, which results in a smaller HOMO-LUMO gap and thus in decreased chemical hardness (21.3 and 16.3 kcal/mol for species 1a and 2a, respectively). In order to characterize dynamically this reaction



Scheme 2.7

an *ab initio* molecular dynamics simulation has been performed, starting from precatalyst 1a with a CO molecule constrained to be at 3.0 Å from the Ru center. The most relevant structural fluctuations of the system are reported in Figure 2.21 During the first picosecond, with the CO molecule constrained at 3.0 Å from the Ru center, only small oscillations in the Ru-methylidene and $C_{\text{ipso}}-C_{\text{ortho}}$ bond distances are observed. Larger oscillations are visible for the $C_{\text{methylidene}}-C_{\text{ipso}}$ distance, but the minimum value never is below 2.5 Å, due to the repulsive interaction between the filled π MO on the methylidene C atom and the aromatic π MOs of the mesityl ring, which is consistent with the MO picture of Scheme 2.7a. During the first picosecond the Ru-CO distance oscillates broadly around 3.0 Å, and CO coordination to the Ru center is forbidden by the constraint. Indeed, after release of this constraint, which is after 1 ps, the CO coordinates rapidly to the Ru center with a damped oscillating behavior centered around a value of ~ 2 Å. Interestingly, as the Ru-CO distance stabilizes, that is at ~ 1.5 -2.0 ps, larger oscillations start in the $C_{\text{methylidene}}-C_{\text{ipso}}$ distance, with peaks at the low values of 2 Å at ~ 2.0 -2.5 ps. Such a short distance is possible because of the transfer of the Ru electron density from the π MO on the methylidene C atom to the π -acid MO of the CO, consistent with the

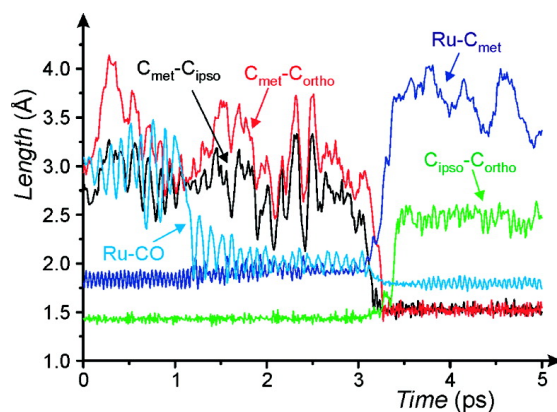
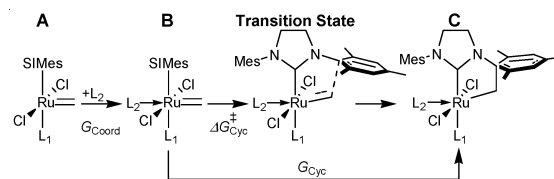


Figure 2.21: Time evolution of the most relevant distances during the AIMD simulation. C_{met} stands for $C_{\text{methylidene}}$.

MO picture of Scheme 3b. Accidentally, at ~ 3.2 ps one of these oscillations overcomes the repulsive forces between the $C_{\text{methylidene}}$ and C_{ipso} atoms (*i.e.*, the system overcomes the transition state 2a–3a of Figure 2.19), and the system collapses rapidly into structure 3a, with clean formation of the $C_{\text{methylidene}}-C_{\text{ipso}}$ bond. Almost immediately, complete rupture of the Ru–methylidene bond of 3a is observed, with simultaneous formation of intermediate 4a that, under the presented simulation conditions, is stable for a very short time between 3.2 and 3.4 ps. In fact, the Buchner expansion step occurs rapidly and the system reaches the final product 7a, with rupture of the $C_{\text{ipso}}-C_{\text{ortho}}$ bond, at ~ 3.6 ps. The heptatriene product 7a is rather stable in the last 1.4 ps of the simulation, suggesting that dynamically 7a is favored over the almost isoenergetic species 4a, probably due to a larger conformational freedom in 7a. This series of events suggests that cyclopropane rupture occurs prior to coordination of the second CO molecule.

At this point one might wonder to which extent this reaction could occur without a ligand trans to the Ru–ylidene bond or, alternatively, in the presence of a π -acid weaker than CO, such as olefins, phosphines, or pyridine, which are typically present during metathesis or, finally, with methyl isocyanide, a ligand used experimentally by Diver, Keister, and co-workers.[156] To this end the first step of the cyclopropanation reaction (see Scheme 2.8) in the absence of any ligand, in the presence of an ethene molecule (to model the C=C double bond of any substrate), and in the presence of a pyridine, a PMe_3 , or a PF_3 molecule (to model typical labile ligands) have been investigated. PF_3 is chosen as an example of a rather π -acid phosphine. On the other hand, also varied the nature of the ligand trans to the NHC ligand has been changed. The results for the various ligands are shown in Table 1. First of all, with no L_2 ligand trans to the Ru–methylidene bond, *i.e.*, in system 1a, entry 1 in Table 1, the



Scheme 2.8

metallacycle structure C of Scheme 2.8 is not stable. All the attempts to locate a metallacycle structure similar to 3a in the absence of an L_2 ligand failed, and the geometry optimization collapsed into the starting species 1a. In the case of $L_2 = \text{CO}$, entry 2 in Table 1, as already discussed in the Results section, the L_2 coordinated species 2a and the metallacycle species 3a (corresponding to B and C in Scheme 2.8) are stable, though the metallacycle 3a is favored relative to 2a by 3.7 kcal/mol. In the presence of the weak π -acid $\text{C}=\text{C}$ double bond of an ethene molecule as well as in the presence of a pyridine molecule trans to the Ru–methylene bond, entries 3 and 4 in Table 1, the metallacycle C is not stable. Indeed, ethene coordination to 1a is even disfavored by 1.8 kcal/mol, probably due to steric crowding around the metal that prevents the ethene molecule to assume a proper orientation (*i.e.*, parallel to the NHC–Ru–P axis) to interact effectively with filled d orbitals of the metal.³⁸ On the other hand, pyridine coordination to 1a is favored by 6.1 kcal/mol, thanks to its σ -donicity and flat geometry, but it lacks the required π -acid property to destabilize the Ru–methylene bond and thus pyridine is unable to stabilize the metallacycle. This conceptual scheme is somewhat confirmed by the behavior of the systems with $L_2 = \text{PMe}_3$ and PF_3 , entries 5 and 6 in Table 1, the latter a prototype of very electron-poor phosphites, which also have moderately strong π -stabilization properties. In these cases both species B and C of Scheme 2.8 are stable, and the metallacycle structure C is slightly more stable than the coordinated species B in the case of the more acidic PF_3 phosphine (by 3.7 kcal/mol) than in the case of the less acidic PMe_3 phosphine (by 0.7 kcal/mol).

At this point the behavior with $L_2 = \text{NH}_3$, entry 7 in Table 2.2, is rather obvious. In fact, differently from phosphines, amines do not show π -acid properties, which explains why NH_3 is unable to stabilize the metallacycle C. Remarkably, a small PH_3 ligand coordinates favorably trans to the Ru–methylene bond, entry 8 in Table 2.2, which clearly indicates that the mesityl rings of the SIMes ligand shields remarkably this position, which would be otherwise reactive. Replacing the L_1 PMe_3 ligand with a pyridine has a minor effect on the behavior of the system (compare entries 10–12 in Table 2.2 with entries 1, 2, and 4) while replacing both L_1 and L_2 with stronger π -acids such as CO and PF_3 (entries 13 and 14 in Table 2.2) results in a reduction of the barrier separating the coordinated species A from the metallacycle species C that, remarkably, becomes

the only stable structure. The electrophilicity of the species with the L_2 ligand coordinated to the Ru atom indicates that the higher the electrophilicity, the higher the reactivity of the methyldene group toward the C_{ipso} . This is reasonable, considering that the LUMO of the species with the L_2 ligand coordinated to the Ru atom mostly corresponds to the π MO on the methyldene group. Interestingly, in all the cases where both structures A and C are stable, the energy barrier for the $A \rightarrow C$ conversion is rather small. This indicates that an L_2 π -acid ligand trans to the Ru-ylidene bond modifies more the thermodynamics that regulates the stability of possible structural isomers of the Ru-complex, rather than the kinetics of the $A \rightarrow C$ conversion.

Table 2.2: Energetics, in kcal/mol, of the First Step of the Cyclopropanation Reaction shown in Scheme 2.8 and Electrophilicity, ω , of the Species with the L_2 Ligand Coordinated to the Ru Atom. The entries G_{Cyc} indicated by a § refer to the species with L_2 dissociated from Ru.

System	L_1	L_2	ω	G_{Coord}	ΔG_{Cyc}^\ddagger	G_{Cyc}
1	PMe_3	none	-	-	-	not stable
2	PMe_3	CO	212.1	-22.5	0.7	-3.7
3	PMe_3	ethene	139.8	1.8	-	not stable
4	PMe_3	pyridine	143.2	-6.1	-	not stable
5	PMe_3	PMe_3	138.5	3.6	1.9	-0.7
6	PMe_3	PF_3	216.1	-12.0	0.2	-3.4
7	PMe_3	NH_3	112.9	-13.2	-	not stable
8	PMe_3	PH_3	145.7	-7.7	5.0	4.6
9	PMe_3	MeNC	152.6	-17.7	3.8	2.7
10	pyridine	none	-	-	-	not stable
11	pyridine	CO	228.3	-19.4	-0.5	-7.0
12	pyridine	pyridine	149.7	-6.9	-	not stable
13	PF_3	PF_3	-	not stable	-	-26.2 §
14	CO	CO	-	not stable	-	-33.9 §

The decomposition pathway discussed so far is the one that seems to be preferred according to these results. Nevertheless, other possibilities have been taken into account. Beside the alternative pathway in which a CO molecule first displaces the PMe_3 ligand, path b in Figure 2.19, the possibility that CO binding to the pre-catalyst 1a, leading to 2a, could promote PMe_3 dissociation from 2a have been investigated. Surprisingly, as the PMe_3 ligand has been removed from 2a the geometry optimization collapsed into the metallacycle structure of Figure 2.22. This structure is 23.0 kcal/mol above 2a, which rules out this possibility. This result evidences once more the remarkable activating role of a π -acid ligand trans to the Ru-ylidene bond. Finally, the energetics of the Buchner ring expansion step after cyclopropanation of the aromatic ring have been explored, in particular looking to the four systems showed in Chart 2.6, in order to get more insights. Comparison between systems 15a–18a and systems

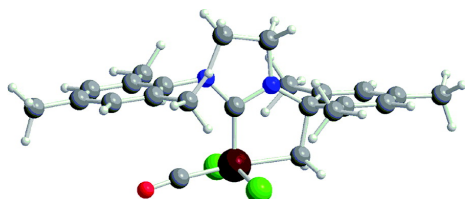


Figure 2.22: Structure of the optimized geometry after removal of the PMe_3 ligand from 2a.

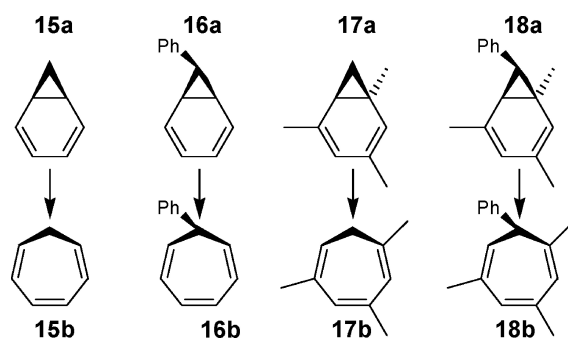


Chart 2.6

15b–18b allows to understand the effect of the ylidene group and of the methyl groups of the mesityl ligand on the energetics of the Buchner ring expansion step. The energetics of this step is shown in Table 2. The clean result is that in all the cases a rather low energy barrier is found. Further, the ring expansion step in 17a f 17b can be directly compared with the ring expansion step 5a f 6a shown in Figure 2.19. Clearly, this step is even more facile in the Ru–complex 5a, with a barrier of only 0.8 kcal/mol and an energy gain of 8.5 kcal/mol, versus a barrier of 2.7 kcal/mol and an energetic gain of 4.3 kcal/mol for the 17a to 17b conversion. In the case of a Ru–benzylidene bond, the ring expansion step would correspond to 18a f 18b. Interestingly, this system presents the highest barrier, 6.7 kcal/mol, and the ring expansion product is practically isoenergetic with the starting cyclopropane species.

2.5.5 Summary

Inspired by the experimental results of Diver and co-workers, who explored the reactivity induced by coordination of CO to the Ru atom of typical NHC-based olefin metathesis catalysts, we clarified the mechanistic details of this transformation. The performed calculations clearly indicate that CO binding to the Ru center promotes a cascade of reactions with very low energy barriers that lead to the final crystallographically characterized product. Analysis of the relevant MOs, supported by dynamics simulations, illuminates the key role

of the π -acid CO coordinated trans to the Ru-methylidene bond. Basically, it attracts electron density from the Ru, which results in reduced Ru back-donation to the π MO on the methylidene group. The reduced electron density on the π MO of the methylidene group allows for a favorable interaction with the π -aromatic system of the proximal mesityl group, which leads to metallacycle formation first and subsequently in the formation of a tensioned cyclopropane structure that finally evolves to the experimental product via a Buchner type ring expansion. Furthermore, the scope of this work to investigate to which extent a large set of π -acid groups that can be normally present during olefin metathesis could promote this deactivating reaction have been expanded. The presented results clearly indicate that several π -acid groups can promote this deactivation route. However, this group must be able to approach the Ru center in the sterically protected coordination position trans to the Ru-methylidene bond. Finally, these comparative analysis indicated that the role of the π -acid is not kinetic in nature (*i.e.*, in lowering the energy barrier for attack of the ylidene group to the proximal mesityl ring) but rather thermodynamic (*i.e.*, in making the metallacycle species a stable intermediate that can further evolve).

Chapter 3

Gold Nanoparticle/Polymer Interfaces: All atom Structures from Molecular Dynamics Simulations

During the past fifteen years, organic semiconductor devices such as light-emitting diodes,[200, 201] photovoltaic cells,[202] and transistors [203] have aroused considerable interest because of the unique advantages provided by organic materials and devices.

An electronic bistable device with a triple-layer structure, two organic layers and a middle discontinuous metal layer, sandwiched between two metal electrodes shows promising performance and can be used as non-volatile memory.[204, 205] But its fabrication is through thermal evaporation in high vacuum, and stringent conditions are required to control the morphology of the middle, discontinuous metal layer. Before the work of Ouyang *et al.*,[206] a memory device using conducting polymers has been reported,[207] but this device can be written only once and cannot be used as programmable memory. A two-terminal electronic bistable device, which can be fabricated through solution processing and can be written/erased many times, should be the target for organic memory.

In particular, polymer nanocomposites based on nanometer-size metal particles are experiencing an explosive growth during the last years due to their technological applications.[208] Organizing inorganic nanoparticles by using soft materials as matrix is crucial for developing materials with new functionalities.[206] A vast array of applications of this class of materials are emerging in the field

of nanoelectronics and have aroused considerable interest because of the unique advantages provided. These advantages include low fabrication cost, high mechanical flexibility and versatility of the chemical structure. Electronic memories using organic materials such as polymers are industrial targets for the next future.[209, 210, 204] Memories based on polymeric materials have been achieved by several groups.[207, 206, 211] The efforts in this field can be ascribed to the number of advantages that this technology offers: the materials used are readily available and easily controlled, the device can be fabricated through simple solution processing, the response time is short, and the operating voltages are low. Furthermore, polymer memories exhibit simplicity in structure, good scalability, low-cost potential, 3D tacking capability and large capacity for data-storage.

Advances in memory technology is involving the development of such kind of nanoscale devices: bistable molecules,[212, 213] donor-acceptor charge transfer complexes,[214, 215] and nanocomposites constructed by organic molecules and nanoparticles[209, 216, 206] are the typical ingredients for the obtainment of these peculiar memory device architectures.

With the development of facile routes of synthesis,[217] gold nanoparticles coated with surface thiol layers are used extensively as building blocks to construct such mesoscopic structures. Yang Yang and co-workers developed several devices based on nanoparticles included into organic or polymeric materials.[218] In particular, organic non volatile memory devices made from a polystyrene (PS) film containing gold nanoparticles and 8-hydroxyquinoline (8-HQ) sandwiched between two metal electrodes shows electrical bistability,[206] that will be briefly introduced in Section 3.1

Understanding the structure of the interfaces, in this new class of materials, is fundamental to improve device function and efficiency, and detailed investigations of interface physics and chemistry are at the focus of research. Understanding and possibly manipulating structural organization at the interfaces level is the key to a “bottom-up” fabrication approach to the development of nanoscale devices. A key issue to rationalize the behaviour and then hopefully to improve the performances of these nanomaterials is a fundamental understanding of the effects of various molecular parameters on the interface structure.

In particular, for the device developed by Yang and co-workers, the bistability has been attributed to an electric field induced charge transfer between the gold nanoparticles and 8-HQ molecules.[206]

Unfortunately, experimental structural information at atomic level for nanoparticles dispersed in polymer matrices, nowadays is extremely difficult especially for the characterization of the interfaces between the nanoparticle and the

dispersing polymer phase. Indeed, classical experimental methods for solving the atomic structure of bulk crystals fail for such materials for the intrinsic difficulty to determine atomic arrangements in nanostructured materials. The need to determine atomic arrangements in nanostructured materials has been called the “nanostructure problem.”[219] It is difficult to achieve an X-ray structure even for gold nanoparticles as pure phase, given to their typical heterogeneity. Just recently, through systematic variation of solution conditions for gold nanoparticle synthesis, a procedure to obtain thiol monolayer-protected gold nanoparticle sufficiently uniform in size for the growth of large single crystals for X-ray structure determination has been reported.[220] Very recently, a sophisticated electron microscopy approach coupled with imaging simulation has been proposed as technique to provide structural insights into gold nanoclusters.[221]

On the other hand, within the last 10 years, computer simulations have evolved becoming a predictive tool for addressing structural investigations of complex materials based on polymers.[222, 223, 224]

For nanostructured materials, the computational prediction of detailed molecular structures is difficult. This is particularly true for polymer based materials, due to the very broad range of length and time scales governing the chain molecular motions.[222]

Many simulation studies to model solid nanoparticles embedded in a polymer matrix have been reported. Most of them use particles without atomistic details. Early studies of coarse-grain models of dense polymer melts containing solid spherical nanoparticles have been conducted with Monte Carlo methods (MC) by Vacatello[225] and with Molecular Dynamics (MD) simulations by Starr and co-workers.[226] Coarse-grain models have been further applied in various MD[227, 228, 229, 230, 231, 232] and MC[233, 234, 235, 236, 237, 238] studies to explore general effects such as the size of the nanoparticles, the filling density and the strength of the nanoparticle-polymer interactions.

For a recent review on theory and simulations of polymer nanocomposites the reader can refer to reference [239].

Brown and co-workers in a preliminary investigation obtained an atomistic detailed model of a silica nanoparticle embedded into an amorphous phase of generic linear polymer modeled at “united-atom” level. [240] Afterwards, they have carried out detailed all-atom MD simulations on a series of PEO oligomer-silica nanoparticle systems.[241] With the exception of the study of Brown and co-workers of reference[241] no further all-atom molecular simulations of nanoparticles dispersed in polymers have been reported.

The scope of this work is to use molecular dynamics simulations in order to provide all-atom models of the interfaces between gold nanoparticles and a polymer matrix. For the relevance of these systems in organic memory tech-

nology, the attention has been focused on programmable devices made of PS containing gold nanoparticles and 8-HQ. A characterization at molecular level of the interfaces between the gold nanoparticles, the polymeric matrix and the 8-HQ molecules can help to understand the behavior of this class of devices.

The model system consists of a gold nanoparticle embedded in a melt of 10-mers of atactic polystyrene as pure phase and in presence of 8-HQ molecules and the effect of nanoparticle coating on the structure of interfaces. In particular, the results of simulations of four systems containing a gold nanoparticle coated by 1-dodecanthiols included in pure polystyrene melt and in presence of 8-HQ as third component and non-coated gold nanoparticle included in pure polystyrene melt and in presence of 8-HQ as third component are reported and compared.

3.1 The “Experimental system”

Ouyang *et al.* described the fabrication and operation of a simple, field-programmable memory cell. The device meets the criteria set out above: the active layer is fabricated by solution processing – *i.e.* with less issues, more expensive – it is write-read-erasable through many cycles, and in addition is potentially competitive with inorganic memory in some ways and potentially outperforms it in others.[206] For example, it can be processed in three-dimensional arrays for very high-density storage. The device has a simple structure with an organic film sandwiched between two aluminium electrodes as depicted in Figure 3.1. The organic film was formed by spin-coating a 1,2-dichlorobenzene solution of

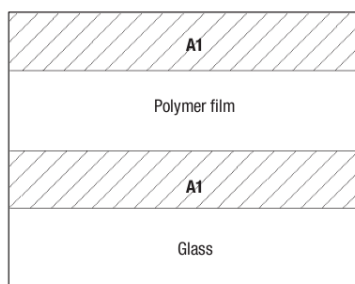


Figure 3.1: Device structure for a device of structure Al/Au-DT+8HQ+PS/Al.

1-dodecanthiols-protected gold nanoparticles (Au-DT NPs), 8-HQ and PS; the whole device could be represented as Al/Au-DT+8HQ+PS/Al. Both the top and the bottom Al electrodes have a width of 0.2 mm, so that the device has an area of $0.2 \times 0.2 \text{ mm}^2$.

3.1.1 Synthesis

The Au-DT nanoparticles were prepared by the two-phase arrested growth method, dissolving 0.62 g $\text{HAuCl}_4 \cdot 3\text{H}_2\text{O}$ in 50 ml water and mixed it with 160 ml p-xylene solution of 3 g tetraoctylammonium bromide. The organic phase was isolated, and 0.4 ml dodecanethiol was added. The formation of the gold nanoparticles was completed by adding 50 ml aqueous solution of 0.76 g NaBH_4 dropwise into the organic solution under vigorous stirring. The nanoparticles were purified by washing with 300 ml methanol at least three times. Nanoparticles were characterized by transmission electron microscopy (TEM) (Figure 3.2) and had a narrow size distribution (1.6–4.4 nm in diameter).

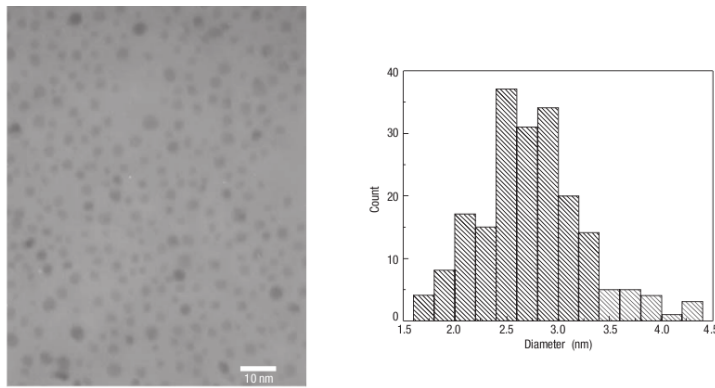


Figure 3.2: Transmission electron micrograph and size histogram of Au-DT nanoparticles. For the simulations below, the smallest radius have been used (0.6 nm).

3.1.2 Testing & Performances

The I–V curves of the device were tested in air, nitrogen or vacuum with an HP 4155B semiconductor parameter analyser or Keithley 2400 Source Meter. The I–V curves at low temperature were tested using a Janis temperature-variable probe station and liquid nitrogen as coolant. The nanosecond voltage pulse was generated by an HP 214B pulse generator. The pulse for the write-erase-read cycles was generated by an HP 3245A universal source, and the pulse and the current on the device were read with a Tektronix TDS 460A four-channel digitizing oscilloscope using a 1-M Ω resistor.

In the next, positive electric field is defined as being when the top electrode is positively biased, and negative electric field when the top electrode is negatively biased. The current-voltage (I–V) curves of the device are shown in Figure 3.3 The device showed very low current, about 10^{-11} A, at 1 V in vacuum. An

electrical transition took place at 2.8 V with an abrupt current increase from 10^{-11} A to 10^{-6} A (Figure 3.3a, curve A). The device showed good stability in this high-conductivity state during the subsequent voltage scan (curve B). The high-conductivity state could be returned to the low-conductivity state by applying negative bias as indicated in curve C, where the current suddenly dropped to 10^{-10} A at -1.8 V. After the device has returned to the low-conductivity state, it can be switched back to the high-conductivity state by applying a higher bias in either polarity (such as “+4 V” or “-4 V”), because of its symmetrical structure. Whether tested under a nitrogen atmosphere or in air, the device showed similar electrical behaviour. The presence of oxygen and moisture in the environment did not affect the threshold voltages for the electrical transitions and the current in the high-conductivity state, but it caused the current in the low-conductivity state to be one order of magnitude higher than that in vacuum. Switching between the high- and low-conductivity states of

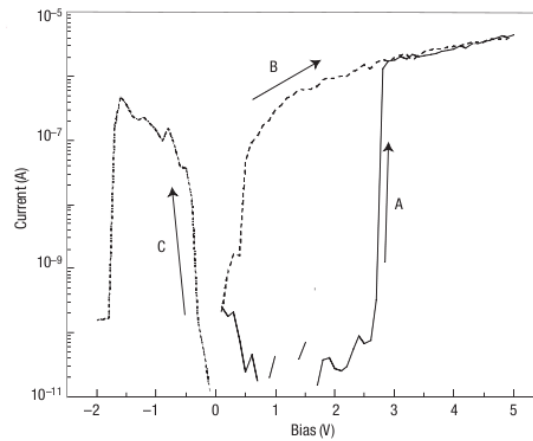


Figure 3.3: Current-voltage curve for a device of structure Al/Au-DT+8HQ+PS/Al. A, B and C in a represent the first, second and third bias scans, respectively. The arrows indicate the voltage-scanning direction.

Al/Au-DT+8HQ+PS/Al was performed numerous times. The device was repeatedly written, read and erased in air, as demonstrated in Figure 3.4 (for convenience the absolute value of the current is shown). A voltage of 5 V was applied to write “1” to the device: that is, this voltage switched the device to the high-conductivity state. By convention, the high-conductivity state is designated with “1” and with “0” as the low-conductivity state.). The written “1” state could be read by a low voltage (1.1 V in this case). The current during the read pulse was of the order of 10^{-7} A. This high-conductivity state was erased by a voltage of -2.3 V, which returned the device to the low-conductivity “0” state. This state could also be detected by applying a small voltage. The current was of the order of 10^{-9} A. These write-read-erase cycles demonstrate that

the device can be used as a non-volatile memory device. The device in the low-

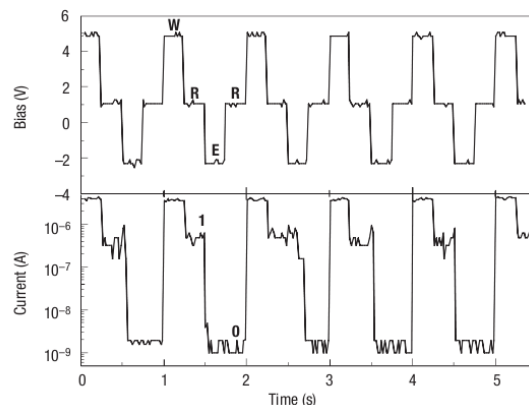


Figure 3.4: Write-read-erase cycles of device Al/Au-DT+8HQ+PS/Al. The top and bottom curves are the applied voltage and the corresponding current response, respectively. W, R and E in the top figure mean write, read and erase, respectively. The labels “1” and “0” in the bottom figure indicate the device in the high- and low- conductivity state, respectively.

conductivity state can be switched to the high-conductivity state by a pulse of 5 V with a width of 25 ns. The authors pointed out that their equipment (HP 214B pulse generator) was incapable of generating a pulse shorter than 25 ns. It is possible that this device is faster than they were able to measure.

The different conduction mechanisms in the two states suggest a change in the electron distribution of the device after the electrical transition. It has already been demonstrated that 8-HQ and gold nanoparticles can be electron donor and acceptor, respectively.[242, 243, 244, 245] Hence, based on our current results, they proposed a charge transfer between Au-DT NP and 8-HQ under a high electric field for the electronic transition in Al/Au-DT+8HQ+PS/Al. Fourier transform infrared and ultraviolet-visible absorption spectroscopy measurements of the composite film indicate that before the electronic transition, there may be little or no direct interaction between the Au-DT nanoparticle and 8-HQ. The concentration of free charge carriers is low, so that the device shows a low current. However, when the electrical field increases to a certain value, an electron on the highest occupied molecular orbital (HOMO) of 8-HQ may gain enough energy to tunnel through the capped molecule, dodecanethiol, into the gold nanoparticle. Consequently, the HOMO of 8-HQ becomes partially filled, and 8HQ and the gold nanoparticle are charged positively and negatively, respectively. Therefore, carriers are generated and the device shows a high-conductivity state after the charge transfer. It is well known that the conductivity of conjugated organic compounds will increase after their HOMO or

LUMO (lowest unoccupied molecular orbital) becomes partially filled.[246, 247]

The latest statements open for further studies that are off topic in this thesis and will not be treated any longer. The next section is intended to guide the reader quickly to the earlier work and concepts that are essential for understanding the present investigation. Further details and extensive validations of the mesoscale approach can be found in references [248] and [249].

The basic idea of coarse-grain (CG) models is to group several atoms in one effective bead.

3.2 Coarse-grained Approach

Although computational power increases 10-fold every 5 years, the huge number of degrees of freedom (DOF) and the large relaxation times typical of an entangled polymer melt effectively precludes fully atomistic approaches to the investigation of long polymer chains. Just to have an idea, the longest relaxation of an entangled polymer melt of length N scales at least as N^3 , giving at least N^4 in CPU time and the required computer time for a reliable equilibration is out of reach. Polymer coarse-grained models have been widely utilized in order to solve this problem.[250, 251, 252, 253, 254, 255] The general strategy is to reduce the number of the DOF by simplifying the models and keeping only those DOF that are relevant for a particular range of interest. In general, the price to pay for a coarser model is the loss of chemical detail. To this purpose, several atoms are grouped together into “super-atoms”, that typically comprised of on the order of ten atoms. The potentials between super-atoms are adjusted to reproduce mainly structural properties of the polymer. The structure of an ensemble of polymer chains are described by the distributions of geometrical quantities. These distributions are extracted from atomistic simulations of oligomers and can be used as targets to be reproduced by the coarse-grained (CG) model.

Following this approach, different polymer properties have been calculated by mesoscale simulations in good agreement with experimental data.[256, 257, 258, 259] In the case of vinyl polymers and in particular for polystyrene, due to its industrial relevance, different coarse-grain models have been recently proposed. The application of different mapping schemes to CG polystyrene and the related results are good illustrations of the idea that, for a given polymer, the choice of the mapping scheme is not unique, and the adopted CG strategy is related mainly to the purpose of the CG simulation.

Milano *et al.* introduced a systematic procedure, based on atomistic simu-

lations of polystyrene oligomers (10-mers) using iterative Boltzmann inversion, to coarse-grain atomistic models of vinyl polymers into a mesoscopic model, which is able to keep information about chain tacticity.[248] The model consists of chains of superatoms centered on methylene carbons of two different types according to the kind of diad (m or r) they belong to; for further explanations see the Subsection 3.2.1. The change to a coarse-grained scale leads to an effective speed-up of 2000 for the computational efficiency of the relaxation of the chains. The proposed mesoscale model has been successfully tested against structural and dynamical properties of the melt for different chain lengths for atactic polystyrene as well as for stereoregular chains and opened the possibility of relaxing melts of high molecular weight vinyl polymers.[248] Sun and Faller reported a coarse-grain model of polystyrene based on iterative Boltzmann inversion to study the dynamics of melts.[260] They further extended this approach to polystyrene-polyisoprene blends.[261] Recently, Kremer and co-workers introduced a coarse-grain model of polystyrene based on atomistic simulations of isolated polystyrene dimers where the bonded parameters are chosen in a way which takes into account polymer stereochemistry.[262] The main purpose of this contribution is the development and validation of a reverse mapping procedure suitable for the coarse-grained model based on diads. It generates well-relaxed amorphous vinyl polymers melts structures at the atomistic level starting from the mesoscale models. This is one of the important uses of coarse grained models.[256] In fact, the apparently complicated procedure “atomistic simulations \rightarrow derivation of a coarse-grained model; coarse-grained simulations \rightarrow reverse-mapping and local relaxation of the atomistic model” is an efficient way to obtain well-relaxed polymer structures. After threading an atomistic model through the coarse-grained chains followed by local relaxation of molecular dynamics, atomistic properties, which depend on the behavior of individual atoms, can be calculated.

3.2.1 Mesoscale Models for Vinyl Polymers

Vinyl chains present along their backbone sequences of methylene ($-\text{CH}_2$) and pseudoasymmetric methyne groups ($-\text{CHR}$). Due to the presence of these pseudoasymmetric carbons, vinyl polymers can be stereoregular or stereoirregular. The definition of isotactic, syndiotactic, and atactic vinyl polymers are well-established in terms of succession of meso (m) and racemo (r) diads, so they have been officially adopted as the IUPAC standard.* A diad can be consid-

*According to the IUPAC stereochemical definitions and notations relating to polymers: “stereoregular vinyl polymers can be defined in terms of the regular sequences of diads; thus an isotactic vinyl polymer consists entirely of m diads, *i.e.*, it corresponds to the following succession of relative configuration $-m-m-m-m-m-m-$, whereas a syndiotactic vinyl polymer consists entirely of r diads, corresponding to the sequence $-r-r-r-r-r-r-$ ”. As for an atactic

ered as the shortest distinguishing piece of a stereosequence if two consecutive configurations have the same absolute configuration (*e.g.*, RR or SS), the diad is meso (*m* diad, see Figure 3.5a); if they are different (*e.g.*, RS or SR), the diad is designated as racemo (*r* diad, see Figure 3.5a). The basic idea of the coarse-graining scheme is to consider a configurational base unit, in particular a diad, as superatom at the mesoscale level. According to this choice, as depicted in Figure 3.5b, the center of a superatom is the methylene carbon. The forcefield corresponding to this choice of mesoscale model has two types of particles *m* or *r*, and three different bond types corresponding to the three indistinguishable triads (*mm*, *mr*, *rr*), and six angle types corresponding to the six indistinguishable tetrads (*mmm*, *mmr*, *mr_m*, *mrr*, *rmr*, *rrr*). Bonds and angle distributions and intermolecular radial distribution functions between the diads extracted from atomistic simulation are considered as target distributions. A valid mesoscale model of a vinyl polymer will produce distributions close to the target ones.

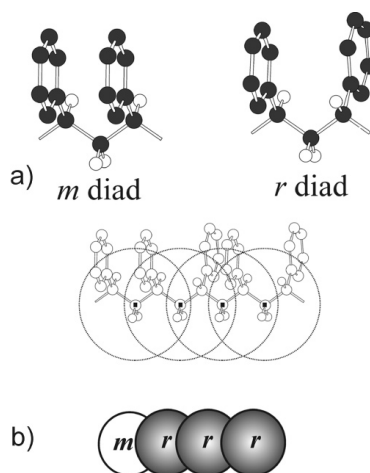


Figure 3.5: (a) Polystyrene *m* and *r* diads in transplanar conformation (hydrogen atoms on phenyl rings are omitted for clarity). (b) Illustration of the mapping scheme for polystyrene: one bead corresponds to a diadic *m* or *r* unit. The center of these super-atoms, as indicated by filled squares, are the methylene carbons. Hydrogen atoms on the phenyl ring carbons are omitted for clarity.

In particular, in the case of polystyrene,^[248] the mesoscale model, which reproduces bond and angle distributions as well as intermolecular radial distribution functions almost identical to the target atomistic ones, gives a very good reproduction of experimental structural data. The parametrization procedure together with mesoscale force field are briefly described in Subsection 3.2.2.

polymer, it is “A regular polymer, the molecules of which have equal numbers of the possible configurational base units in a random sequence distribution”; *i.e.* it corresponds to a random sequence of *m* and *r* diads.

3.2.2 Mesoscale Potentials and Force Field Parametrization

Mesoscale potentials obtained by Boltzmann inversion of a multi-peaked distribution approximated by a sum of several Gaussian functions have been recently proposed as a valid alternative to a fully numerical approach for bond and angle terms in mesoscale force-field for polymers:[263] Defining a Gaussian distribution of a bond length or bond angle denoted as θ :

$$g_i(\theta) = A_i/w_i\sqrt{\pi/2} \exp^{-2(\theta-\theta_{ci})^2/w_i^2} \quad (3.1)$$

the mesoscale potential can be obtained by Boltzmann-inverting a sum of such Gaussian distributions:

$$V(\theta) = -kT \ln \sum_{i=1}^n g_i(\theta) \quad (3.2)$$

and the corresponding force:

$$F(\theta) = -4kT \frac{\sum_{i=1}^n g_i(\theta) \frac{(\theta-\theta_{ci})}{w_i^2}}{\sum_{i=1}^n g_i(\theta)} \quad (3.3)$$

Additional information about the multicentred Gaussian-based potentials (MG-potentials) employed here can be found in references.[248, 263] As for the non-bonded part of the potential, pressure-corrected CG numerical potential optimized by iterative Boltzmann inversion have been used.[264] The effective non-bonded potential $V(\mathbf{r})$ is derived from a given tabulated starting potential $V_0(\mathbf{r})$, targeting to match the radial distribution function $g(\mathbf{r})$. The potential is iteratively improved by successive corrections,

$$V_{j+1}(\mathbf{r}) = V_j(\mathbf{r}) + kT \ln \frac{g_j(\mathbf{r})}{g_{target}(\mathbf{r})} \quad (3.4)$$

Further details of the parametrization procedure, including a complete set of distribution plots, and its validation against structural and dynamical properties can be found in the paper of Milano *et al.*[248]

3.2.3 Reverse mapping

The strategy chosen for an efficient reverse-mapping is based on rigid superposition of atomistic diads on the coarse-grained coordinates obtained from the mesoscale simulations. In particular, as sketched in Figure 3.6, in a chain made of i diads, the atomistic DOF are rebuilt superposing one by one atomistic

diad structures corresponding to different m or r superatoms. For a consistent rebuilding of the atomistic polymer structure, great care has to be taken to reinsert diads of proper chirality. Figure 3.6a shows the case of an end group, e , followed by a sequence of two m diads. The first inserted structures are the end groups, at the beginning of each chain, with equal probability, an end group of absolute chirality R or S is chosen. This initial choice of the absolute configuration determines the absolute configuration of the atomistic sequence utilized for the reverse-mapping of the entire chain. For instance, given an R chirality of the end group, a sequence of two m superatoms is formed by the addition of two diads in which the chiral carbons (indicated with an asterisk in Figure 3.6a) have both R configuration. Given the chirality S of the end group the same sequence of two m superatoms is translated into an atomistic structure by adding two diads both of S configuration. Similar considerations can be done for all possible sequences of diads sketched in Figure 3.6a–d. Once the chirality of the end group is fixed, it is possible to establish from the superatoms sequences of the coarse grained model the chirality of all the repeating units that have to be added. Then, the chain reverse-mapping can proceed as indicated in Figure 3.6a. First, the atomistic end group is rebuilt by superposing the three superatom centers with the corresponding three methylene groups (indicated by filled squares in Figure 2a). In a similar way, the following diad insertion (see diad $i + 1$ in Figure 3.6a) is done superposing the three methylene groups of the atomistic diad model indicated by squares with their corresponding mesoscale particle centers as indicated in the Figure 3.6a) Additional conditions are considered for the superposition of a non end group diad.

The structures obtained have to minimize the rmsd between methylene carbons and superatom centers and between some of the atoms (first chiral carbon and the hydrogen bonded to it) of the inserted diad with the corresponding atoms (last chiral carbon and the hydrogen bonded to it) of the previously inserted diad.

Structure superposition methods are used widely to compare molecular structures. They allow to superimpose molecular structures to facilitate visual comparisons and to give a quantitative measure of shape similarity as the root-mean-square deviation of distances between corresponding atoms. One can use different numerical and analytical approaches to the rigid fit of two structures. Methods based on linear algebra have been widely employed.[265, 266, 267] In general, the problem can be solved by finding the optimal orthogonal transformation and requires determination of a rotation matrix \mathbf{R} and a translation vector that will superimpose two sets of coordinates. In our case, due to the presence of chiral centers, the additional requirement of chirality preservation has to be considered. In linear algebra language, this means that the orthogonal transformation must not include reflections. Our choice is a method based

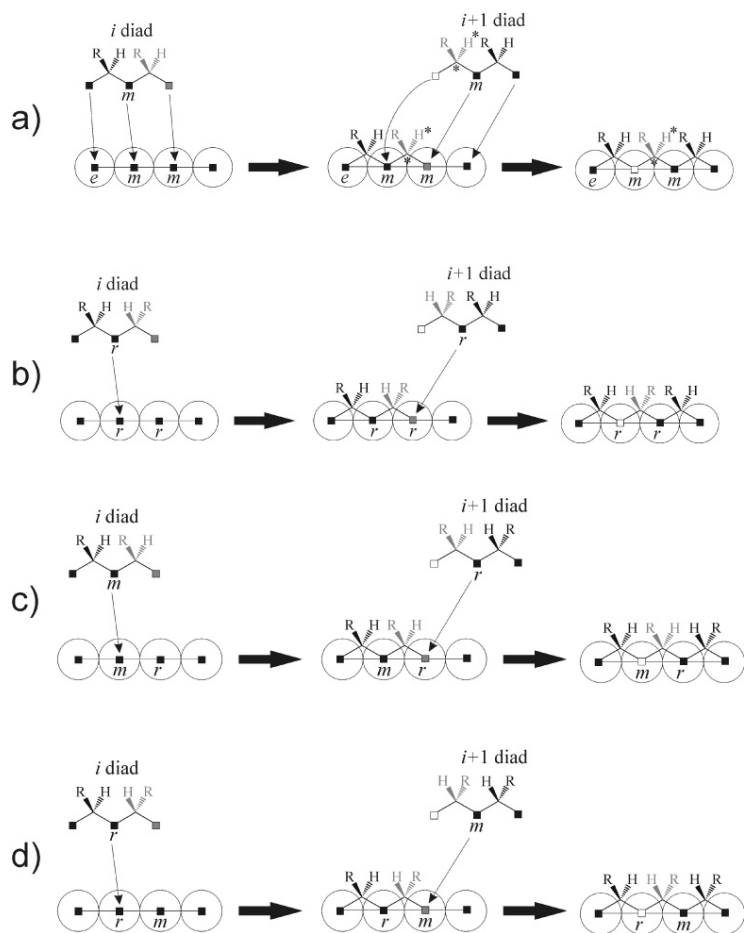


Figure 3.6: Atomistic diads rebuilding. All four possible (a) mm , (b) rm , (c) mr , (d) rr cases are depicted. Depending to the end group absolute R or S configuration each the four possible diad sequence can be translated in the correct atomistic sequence according to the mapping rules indicated in reference [249].

on quaternions introduced by Kearsley.[268] Which is analytical (*i.e.*, fast) and assures chirality preservation. Quaternions are a non-commutative extension of complex numbers and are widely used to describe rotations in classical as well as quantum and relativistic physics.

Just to have an idea, the reverse-mapping of the systems containing 150 chains of nine diads (corresponding to 150 10-mer chains, 24750 atom positions were rebuilt), and three chains of 350 diads (corresponding 3 351-mer chains, 16863 atom positions were rebuilt) took few seconds on a common personal computer (Pentium 4, 3 GHz).

For further details see reference [249].

3.3 Simulations Strategy and Initial Configurations Setup

In the case of a pure polymer melt, in a series of papers a systematic procedure to obtain well-relaxed all-atom melt structures of polystyrene starting from mesoscale simulations of realistic coarse-grain models have been introduced and validated.[241, 269, 248, 270, 249] The coarse-grain models obtained from reference atomistic simulations have been successfully tested using both MD [248] and, in order to simulate melts of molar mass up to 210000 g/mol, by connectivity-altering MC simulations.[270] In both cases, chain dimensions were found in very good agreement with experiments. Furthermore, the equilibrated long-chain configurations reduced to entanglement networks via topological analysis[271] provided a very good estimate of the molar mass between entanglements and of the entanglement tube diameter extracted from plateau modulus measurements. These coarse-grain models have been also used to calculate the viscosity by reverse non-equilibrium molecular dynamics (RNEMD).[269] Finally, well relaxed all-atom melts successfully tested against experimental data have been obtained by using a reverse-mapping procedure based on quaternion algebra that, starting from equilibrated mesoscale melt structures, allows a very fast and efficient reconstruction of the atomistic detail.[249]

Here a similar approach using coarse-grain simulations and successive reverse-mapping has been employed to obtain initial configuration for four different systems modeling a polymer melt including a nanoparticle. In particular, as sketched in Figure 3.7, as first stage, starting from one configuration obtained by MD equilibration of coarse-grain polymer chains, with periodic boundary conditions, an equilibrated atomistic configuration has been obtained applying the procedure described and validated in reference [249].

The initial configurations of a nanoparticle embedded into a polymer melt have been obtained inserting the gold nanoparticle into a cavity placed in the center of the cubic box. The cavity has been obtained discarding from the back mapping procedure the polymer chains overlapping with the nanoparticle. The chosen overlap criterion is geometrical. In particular, two atoms are overlapped if the distance between them (scaled by a tolerance coefficient λ chosen between 0.6 and 0.8) was less than the arithmetic average of their Lennard-Jones σ parameters. In the case of the non-coated nanoparticle, this procedure gives systems ready for the equilibration run with a timestep of 2 fs. For the coated nanoparticle, due to the presence of 1-dodecanethiol chains, the equilibration is more difficult. A straight application of the procedure outlined above gives a very low polymer density around the particle. This results in collapses of polymer chains in the neighborhood of dodecanethiol that causes failing of the

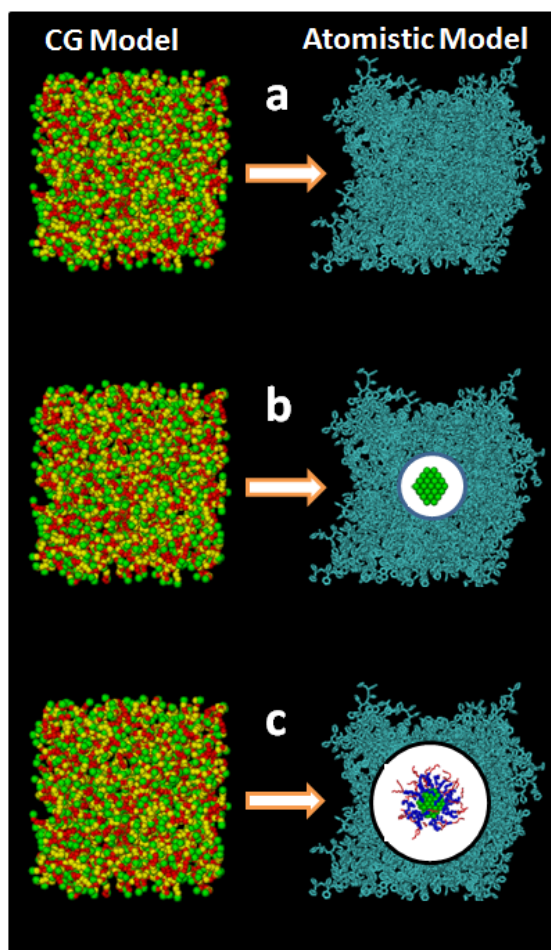


Figure 3.7: On the left side coarse-grain models of polymer melts used for the back mapping procedure are shown. The red beads correspond to m diads the yellow ones to r diads. Coarse grain particles representing chain end groups are in green. In the atomistic models the hydrogen atoms are not depicted for clarity. Schematization of the reverse-mapping procedure for the obtainment of initial configurations of (a) PS polymer melt; (b) PS polymer melt containing a non-coated nanoparticle (systems 1 and 3 of Table 3.1). (c) PS polymer melt containing a coated nanoparticle (systems 2 and 4 of Table 3.1). The coated nanoparticle has been depicted with methyl chain end groups and the four subsequent five methylene carbon atoms, for which in the reverse-mapping procedure λ is set equal to 0, in red, the remaining atoms of the chains are in blue.

constraint algorithm for reasonable values of the time step. As opposite, using different tolerance for the dodecanethiol atoms ($\lambda = 0$ or very low values and between 0.6 and 0.8 for the other atoms) and introducing slowly excluded volume interactions between the polymers and dodecanethiol atoms avoids the chain collapse but makes the procedure very long. The best choice was to use $\lambda = 0$ for the thiols methyl groups and for subsequent five carbon atoms and hydrogens bonded to them and between 0.6 and 0.8 for the other atoms. This avoids chain collapses and the excluded volume interactions can be introduced in few stages.

To avoid possible artifacts depending on the chosen preparation procedures, all systems were subjected to equilibration runs of 6 ns followed by production runs not smaller than 10 ns. Table 3.1 contains details about all simulated systems.

Table 3.1: Simulated systems. All systems have been simulated at constant temperature and pressure (500 K and 1 bar).

System	Nanoparticle	No. of PS chains	No. of 8HQ	Total. No. of atoms
1	Non-coated	145	0	24004
2	Coated	127	0	22478
3	Non-coated	86	277	19255
4	Coated	86	277	20699

System	$\rho(r)$ [kg/m ³]	Aver. Box size [nm]	D _{PS} ×10 ⁶ [cm ² /s]	D _{8HQ} ×10 ⁶ [cm ² /s]	Sim. Time [ns]
1	1057.9	6.42	1.51	–	10.5
2	1051.3	6.29	1.48	–	13.6
3	1072.7	6.10	3.25	20.5	30.0
4	1051.6	6.25	3.40	20.8	30.0

3.3.1 Simulation Details

All atomistic simulations were performed with the GROMACS package. [272] The Berendsen manostat and barostat were used to get a NPT ensemble with $\tau_P = 10$ ps and $\tau_T = 0.1$ ps couplings with a time step of 0.2 fs. All bond lengths were kept constant by the SHAKE algorithm while for non-bonded interactions a cut-off together with a neighbor list of 1.35 nm were used.

For CG simulations, the GMQ_num code, a version of the GMQ package able to

handle numerical potentials and modified in order to implement multicentred Gaussian potentials, was used. The simulations were performed at constant temperature (500 K) and constant pressure ($P = 1$ bar) for production runs. The time constants for the loose coupling thermostat and manostat were set to 0.1 and 5 ps. A time step of 15 fs was used. Non-bonded interactions were truncated beyond 15 Å.

The polystyrene force field has been already used to describe different polystyrene based materials: polystyrene gels,[273, 274], amorphous PS calculation of positronium annihilation spectra,[275] anisotropy of diffusion of helium and CO₂ in a nanoporous crystalline phase of syndiotactic PS.[276] Details about the force field and parameters can be found in reference.[249] Both coated and non-coated nanoparticle models consider a gold core made of 79 Au atoms, organized in a cubo-octahedral geometry with a Au-Au bond length of 0.292 nm. The model of coated nanoparticle has 38 thiolate chains. This number has obtained experimentally and reported by Murray *et al.* for coated nanoparticles of 79 Au atoms in cubo-octahedral geometry.[277]

The Lennard-Jones σ and ϵ values for Au were set as 0.293 nm and 0.1631 kJ/mol, Au-S bond has been modeled by a harmonic potential with a minimum distance of 0.240 nm, all the parameters regarding Au, C, and S atoms have been taken from the models of an Au(111) surface coated by alkylthiolate monolayers reported by Ayappa and co-workers, further details and parameters can be found in reference [278].

The 8-HQ model was developed on the basis of similarity between this molecule and organic molecules present in the OPLS force field.[279] In particular, σ and ϵ parameters corresponding to pyridine and phenol have been employed. The σ and ϵ values of N were set as 0.325 nm and 0.71128 kJ/mol. The σ and ϵ values of O were set as 0.307 nm and 0.71128 kJ/mol. For N atom partial charges and constrained distances employed for 8-HQ are shown in the Figure 3.8 below. Other parameters regarding bond angles, proper and improper torsions have been taken from OPLS models for pyridine and phenol.

3.4 Results & Discussion

3.4.1 Polymer Chains and 8-HQ diffusion

In Figure 3.9 the center of mass mean square displacement (MSD) of PS chains as function of time is shown. From the slope of the curves reported it is possible to calculate diffusion coefficients, using Einstein's equation:

$$6D = \frac{d}{dt} \langle |R_i(t) - R_i(0)|^2 \rangle \quad (3.5)$$

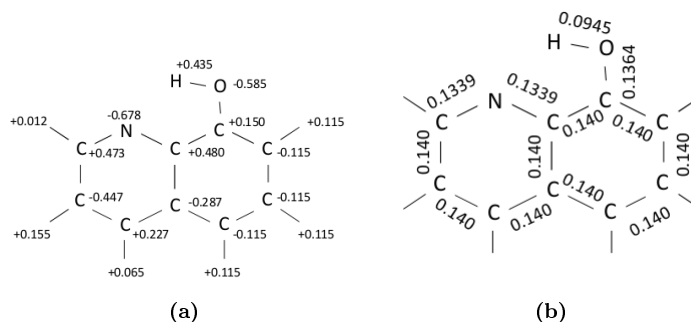


Figure 3.8: (a) Partial charges (ecu) adopted for the 8-HQ model. (b) Bond constraints (nm) adopted for the 8-HQ model. The C-H bond have been all constrained to 0.108 nm.

Where $R_i(t)$ is the position of the i^{th} polymer center of mass at time t . Averaging is performed over all polymer chains as well as over time origins. As reported in Table 3.1, the diffusion coefficients of polymer chains have similar values in both systems containing a non-coated and a coated NP, in both cases the calculated value is about 1.5×10^{-6} cm²/s. This value is lower than the one for a pure PS melt of 2.4×10^{-6} cm²/s calculated at the same temperature using the same PS model.[248] This difference shows that the presence of a NP in a polymer melt reduces the chain mobility. From the Figure 3.9 is also clear that both curves corresponding to simulated systems including the 8-HQ molecules (systems 3 and 4) show a similar behavior and a higher slope with respect to systems 1 and 2 in which there is a pure polymer phase. This is reasonable because it is known that in presence of a lower molecular weight compound there is an increase of mobility of a polymeric material. The resulting center of mass diffusion coefficients for PS chains are 3.25×10^{-6} cm²/s for the system including a non-coated NP and 3.40×10^{-6} cm²/s for the system containing a coated NP.

For the smaller 8-HQ molecule one order of magnitude larger (see Table 3.1) diffusion coefficients than for PS chains are calculated for both systems 2 and 4.

3.4.2 Radial Density Profiles

In Figure 3.10 radial mass densities $\rho(r)$ as function of the distance r from the nanoparticle center of mass are shown. In particular, in Figure 3.10a the radial mass density of PS chains as a pure phase is shown.

The $\rho(r)$ of Figure 3.10a shows two distinct peaks at about 1.3 and 2.3 nm.

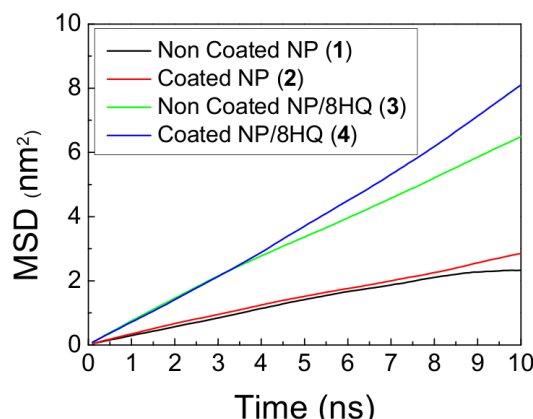


Figure 3.9: Mean square displacements *Vs.* time calculated for the centre of mass of PS chains in the four considered systems. The two curves corresponding to systems 3 and 4 containing 8-HQ molecules show larger slopes with respect to the systems with a pure polymer phase.

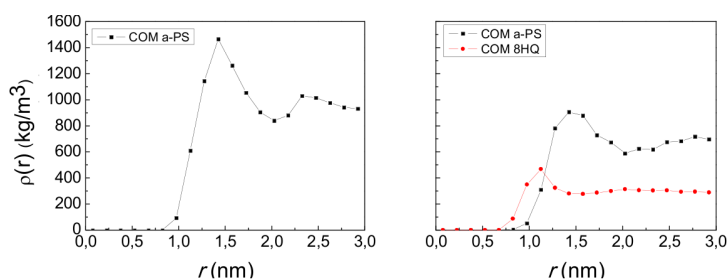


Figure 3.10: Radial density profiles of the centre of mass of PS chains, for systems containing a non-coated gold nanoparticle as function of the distance from NP centre of mass. (a) System 1. (b) System 3. In red is reported the calculated radial density for the centre of mass of 8-HQ molecules.

The first peak is stronger (1500 kg/m^3), showing a chain ordering in the vicinity of the nanoparticle, the second peak is weaker (1000 kg/m^3). Beyond 2.5 nm the value of the density becomes equal to the polymer melt density. This means that at distances larger than 2.5 nm there is no correlation between the presence of the nanoparticle and polymer chain positions. The calculated radius of gyration of the non-coated nanoparticle is 0.53 nm, while for a polymer chain is about 0.6 nm. It is apparent that polymer chains closer to the nanoparticle are arranged in two layers the first one more tightly packed (with a density 60% higher than the melt value) the second one less but with a density still higher (around 10%) than the pure PS melt. This is not surprising and this typical behavior is reported by numerous simulations studies.[225, 233, 236, 227, 280, 228, 240, 210, 241]

The $\rho(r)$ of Figure 3.10b shows the behavior of the system in presence of 8-HQ. The radial density retains the main the features of the corresponding

one in a polymer pure phase. There is still a packing of polymer chains close to the nanoparticle but, in this case, a single peak at 1.3 is obtained showing less strong chain ordering (1000 kg/m^3). As for third component, the first peak (red curve of Figure 3.10b) lies at 1.1 nm indicating some preference for 8-HQ molecules to be placed at the polymer/nanoparticle interface.

Different is the behavior of the system containing the coated nanoparticle shown in Figure 3.11. In fact, beside an obvious shift of the first peak at larger distances due to the alkanethiol chains excluded volume interactions (in this case the sum of the nanoparticle 0.89 nm and polymer gyration radius is about 1.5 nm), this system is characterized by a smoother behavior of the $\rho(r)$.

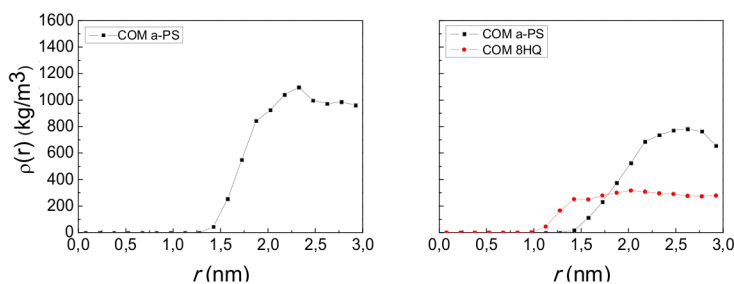


Figure 3.11: Radial density profiles of the centre of mass of PS chains, for systems containing coated gold nanoparticle as function of the distance from NP centre of mass. (a) System 2. (b) System 4. In red is reported the calculated radial density for the centre of mass of 8-HQ molecules.

The density shows much less structure and a slower growth from zero to the maximum value (1100 kg/m^3 at about 2.2 nm). In the same way the $\rho(r)$ of 8-HQ (red curve of Figure 3.11) does not show peaks in the vicinity of the coated nanoparticle. Furthermore it is interesting to note that the $\rho(r)$ of 8-HQ shows quite high values (comparable with the long distance one) already for distances smaller than the nanoparticle radius of gyration. This indicates a penetration of the 8HQ molecules inside the dodecanthiols layer.

This feature will be more clear and will be treated in a more detailed way in the following where the atomic contribution to the radial density will be discussed: atomic radial mass densities $\rho(r)$ for the each system as function of the distance r from the nanoparticle center of mass are shown. In particular, the density due to backbone, phenyl rings and end groups carbon atoms of the polymer chains will be reported separately.

In Figure 3.12 the behavior of $\rho(r)$ for the system containing a non-coated nanoparticle in a pure polymer phase is shown. It is worth noting that, as results

from the curve related to the phenyl rings (red curve of Figure 3.12), the atoms of the rings are closer to the nanoparticle/polymer interface. Non zero values of the density of the aromatic carbons start from 0.6 nm. In Figure 3.13 is

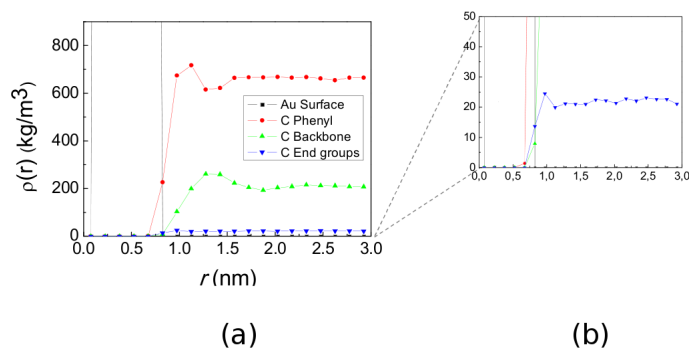


Figure 3.12: Atomic radial mass densities as function of the distance from the NP centre of mass for system containing a non-coated nanoparticle in a pure polymer phase.

shown a typical configuration of polymer chains close to the nanoparticle, from the picture it is clear that the polymer chains approach the nanoparticle surface exposing mainly the phenyl rings.

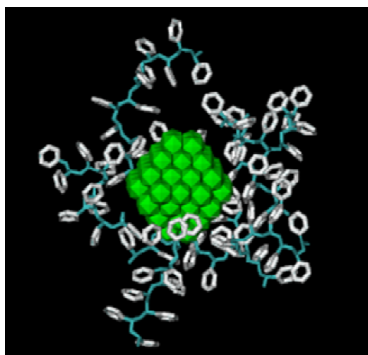


Figure 3.13: Snapshot of system 1, showing some polymer chains closer to the nanoparticle surface. Polymer chains approach the nanoparticle surface exposing mainly the phenyl rings (white color). The backbone carbons are in blue, hydrogen atoms are omitted for clarity.

In Figure 3.12b is reported a detail of the plot of Figure 3.12a, in particular, the polymer chain end groups radial density is shown in a smaller scale. From the plot of Figure 3.12b is clear that there is a slightly higher concentration of end groups at a distance of about 1 nm from the nanoparticle center of mass.

In Figure 3.14 the behavior of $\rho(r)$ for the system containing a non-coated nanoparticle in polymer phase in presence of 8-HQ is shown. Similarly to the

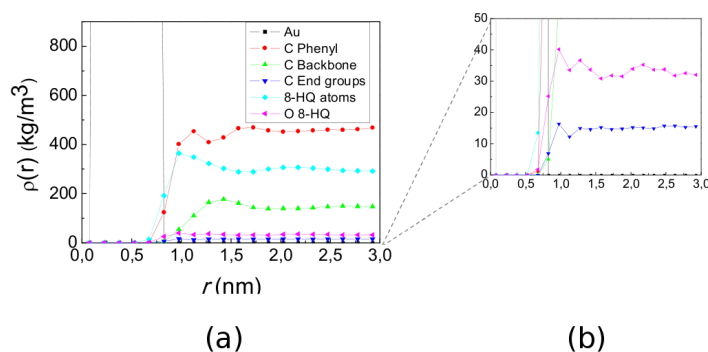


Figure 3.14: Atomic radial mass density as function of the distance from the NP centre of mass for system 3, containing a non-coated nanoparticle in a polymer phase in presence of 8-HQ molecules

pure polymer system, the phenyl carbon atoms are closer to the nanoparticle but the peak is less pronounced showing less structuring of the polymer around the nanoparticle (this different behavior is also apparent in the centre of mass radial densities). In this case also the atoms of 8-HQ are close to the nanoparticle surface. Non zero values of radial density of atoms of 8-HQ start from about 0.6 nm. Also in this case there is a higher concentration of the polymer end groups at a distance of about 1 nm from the nanoparticle centre of mass.

The discussion is focused now on the systems including a coated nanoparticle, in Figure 3.15 the behavior of $\rho(r)$ for the system containing a coated nanoparticle in a pure polymer phase is reported. The alkanethiolate carbon chains

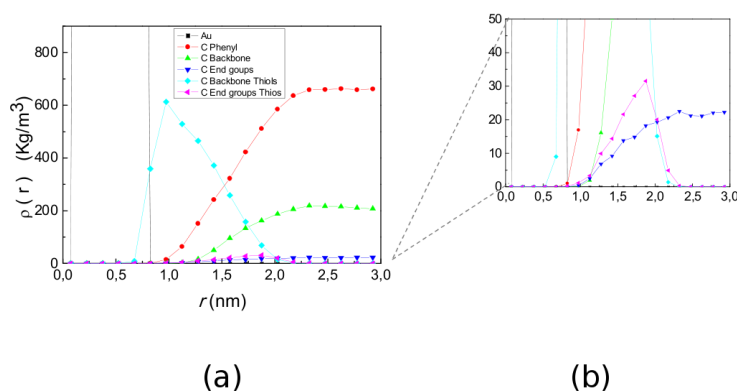


Figure 3.15: Atomic radial mass densities as function of the distance from the NP centre of mass for the system 2 containing a coated nanoparticle in a pure polymer phase

density (aqua curve of Figure 3.15a) shows non zero values until 2.0 nm. This length can be considered as the maximum average nanoparticle radius. Also in this case the atoms closer to the interface are the phenyl ring carbons. It is worth noting that the curves of the radial density of alkanethiol carbons and the one related to polymer chains largely overlap in the region going from 0.7 to 2 nm from the NP centre of mass. This indicates that the polymer chains atoms, especially the one of phenyl rings penetrate, at some extent, inside the alkanethiolate chains. Indeed, non zero values of the radial densities of phenyl carbon atoms can be observed starting from 0.7 nm. In contrast with the behavior of the system including a non-coated nanoparticle the radial density of carbon atoms of both phenyl rings and backbone grows more smoothly and without showing a maximum. Furthermore, differently from the behavior of the systems with a non-coated nanoparticle, there is not an higher concentration of polymer chain end groups close to the gold surface neither in the region of alkanethiolate chains. In particular, from Figure 3.15b it is clear that the polymer chain end groups radial density increases smoothly from zero starting from about 1 nm from the nanoparticle centre of mass until reaching the constant bulk value starting from 2.1 nm from the nanoparticle centre of mass. The radial density of NP alkyl chains end groups shows a maximum at around 2 nm in the region of nanoparticle polymer interface.

In Figure 3.16 is shown a typical configuration of polymer chains close to the coated nanoparticle, from the picture is clear that the polymer chains approach the nanoparticle surface exposing the phenyl rings (white atoms), some of the rings penetrate trough the alkyl chains (in red) layer.

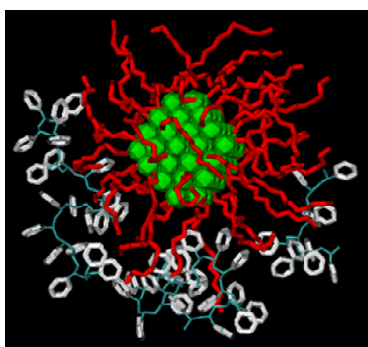


Figure 3.16: Snapshot of system 2, showing some polymer chains closer to the nanoparticle surface. Similarly, to system 1 (shown in Figure 3.13) polymer chains approach the nanoparticle surface exposing mainly the phenyl rings (white color) some of the phenyl rings penetrate trough the alkyl chains layer (in red). The backbone carbons are in blue, the thiols chains are depicted in red, hydrogen atoms are omitted for the sake of clarity.

In Figure 3.17A the radial densities of the system including a coated nanopar-

ticle in a polymer phase in presence of 8-HQ are shown.

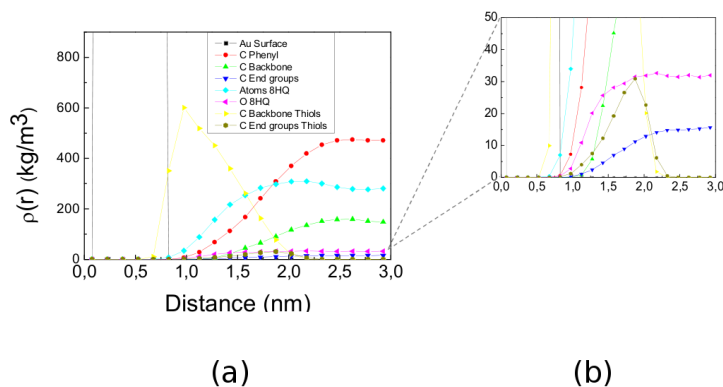


Figure 3.17: Atomic radial mass densities as function of the distance from the NP centre of mass for the system 4 containing a coated nanoparticle in a polymer phase in presence of 8-HQ molecules.

Similarly to the pure polymer system, the phenyl carbon atoms are close to the nanoparticle and from the overlap between the curves related to phenyl and backbone carbon atoms and to the alkyl chains of the nanoparticle also in this case it is possible to observe some penetration of the polymer chains inside the coating layer. In this case, the atoms closer to the gold surface are the 8-HQ ones. In fact the curve related to the 8-HQ atoms radial density starts to show non zero value from about 0.6 nm and finally grows to bulk values starting from distances from the nanoparticle centre of mass of about 2 nm. It is worth noting that, in the case of the non-coated nanoparticle, the 8-HQ molecules are close to the nanoparticle surface together with the carbon atoms of the phenyl groups (the two curves of Figure 3.17 corresponding to 8-HQ and phenyl carbon overlap in the region close to the gold surface).

In contrast, in this case for the coated NP shown in Figure 3.17a the radial density of 8-HQ atoms results closer to the NP centre of mass and the curve corresponding to the phenyl ring is shifted at a larger distance. Furthermore, in the case of Figure 3.17a, the radial density of 8-HQ atoms grows more smoothly than the one shown if Figure 3.17 and does not show peaks. Also in this case the radial density of NP alkyl chains end groups shows a maximum at around 2 nm in the region of nanoparticle polymer interface.

3.4.3 Polymer Chain Dimension

In Figure 3.18 the behavior of end-to-end distance and radius of gyration of the PS chains as function of the distance between the nanoparticle and chain

centre of mass are reported. In particular, in Figure 3.18a are shown the data extracted from the simulations of systems including a non-coated nanoparticle. From Figure 3.18a it is clear that for both pure polymer phase as well as in presence of 8-HQ there is an increase of the dimension for chains closer to the nanoparticle. In particular, at short distance from the nanoparticle, for the systems shown in Figure 3.18a there is an increase of about 6% (black curve) in the end-to-end distance from the value of the melt. For the system including 8-HQ (red curve of Figure 3.18a) there is a similar increase (about 7%) of the chain dimension. At distances larger than 2 nm the chain dimension converges to the value of the pure PS melt. The results are similar for the system including 8-HQ (red curve of Figure 3.18a). For the systems shown in Figure 2.1a the behavior of the radius of gyration shows trends similar to the end-to-end distance.

In Figure 3.18b are shown the data extracted from the simulations of systems including a coated nanoparticle. The behavior is similar to the one shown in Figure 3.18a, there is an increase of the chain dimension close to the nanoparticle then for larger distance the dimension converges to the one of the pure polymer melt. The system in pure polymer phase shows a chain expansion of about 8% with respect to the value of pure polymer melt close to the nanoparticle. In the presence of 8-HQ (red curve of Figure 3.18b) the chain expansion is about 5%. In all cases for both non-coated and coated nanoparticles in the case of pure polymer phase and in presence of 8-HQ an increase of the chain dimension going from 5 to 8% is found. A similar behavior has been obtained in simulations of model bead a spring polymers in contact with a nanoparticle by Glotzer *et al.*[229] the increase in the dimension was found to be of the order of 20%. Brown and co-workers found from molecular dynamics simulations of PEO oligomers in contact with a silica nanoparticle an expansion of chain dimension of the order of 15%. Brown The smaller expansion values that we obtained probably are due to the larger stiffness of PS with respect to more flexible bead and spring and PEO chains.

3.4.4 Orientation of 8-HQ molecules

The orientation of 8-HQ with respect to the nanoparticle can be characterized using certain molecule-fixed unit vectors. In Figure 3.19 are schematized the structures of the gold nanoparticle and 8-HQ together with the vectors used to characterize the orientation of 8-HQ with respect the (111) surface of the nanoparticle.

In particular the vectors $\hat{\mathbf{u}}_{\text{NP}}$ perpendicular to the eight (111) surfaces of the octahedral nanoparticle and the three vectors $\hat{\mathbf{u}}_1$, $\hat{\mathbf{u}}_2$ and $\hat{\mathbf{u}}_3$ are depicted.

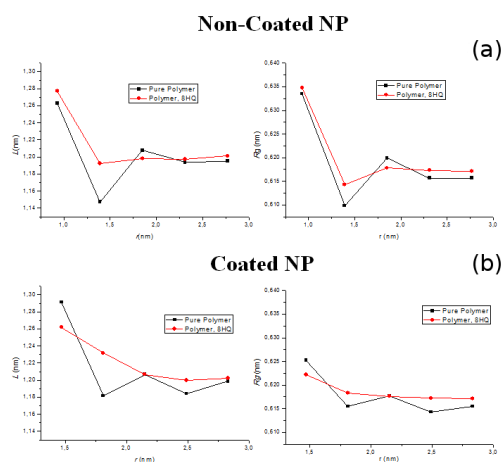


Figure 3.18: (a) PS end-to-end distance (L) and radius of gyration (R_g) as function of distance between NP and PS centre of mass for systems 1 (black curves) and 3 (red curves) containing a non-coated nanoparticle. (b) PS end to end distance (L) and radius of gyration as function of distance between NP and PS centre of mass for systems 2 (black curves) and 4 (red curves) containing a coated nanoparticle.

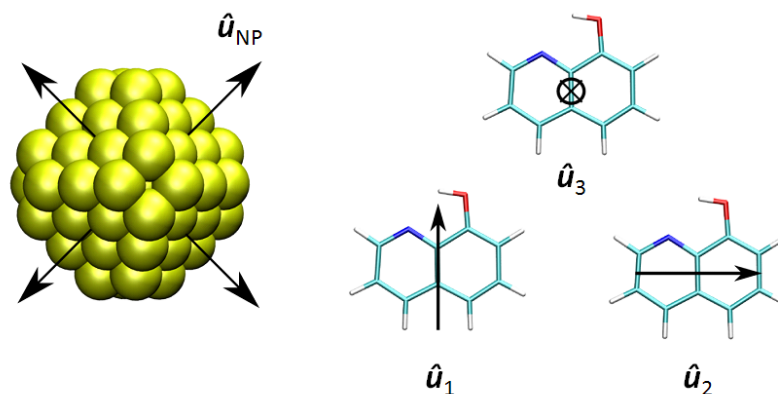


Figure 3.19: Schematized structures of gold nanoparticle and 8-HQ together with the vectors used to characterize the orientation of 8-HQ with respect the nanoparticle (111) surface. Four among eight possible \hat{u}_{NP} vectors perpendicular to the nanoparticle surfaces are shown

As unit vector have been arbitrarily taken: \hat{u}_1 the in-plane vector along the bond shared by the two rings of 8-HQ; the other in-plane vector \hat{u}_2 , perpendicular to \hat{u}_1 and joins the middle of the two C-C bonds parallel to the central C-C bond; a third orientation vector \hat{u}_3 obtained by the vector product of $\hat{u}_1 \times \hat{u}_2$ is normal to the molecular plane.

The orientation of the 8-HQ molecule with respect to the nanoparticle, as

function of the distance between the nanoparticle and 8-HQ centre of mass, has been characterized calculating a suitable orientation function averaged over different molecules, for all eight $\hat{\mathbf{u}}_{\text{NP}}$ vectors and simulation time. Specifically, the mutual orientation of the nanoparticle surface and the 8-HQ molecular plane can be obtained considering the angle between the vectors $\hat{\mathbf{u}}_{\text{NP}}$ (perpendicular to the (111) nanoparticle surface) and $\hat{\mathbf{u}}_3$ perpendicular to the molecular plane of 8-HQ. In Figure 3.20 is reported the averaged order parameter P_2 of the angle between the vectors $\hat{\mathbf{u}}_{\text{NP}}$ and $\hat{\mathbf{u}}_3$ as function of the distance for the system containing a non coated nanoparticle in the presence of 8-HQ. The order parameter

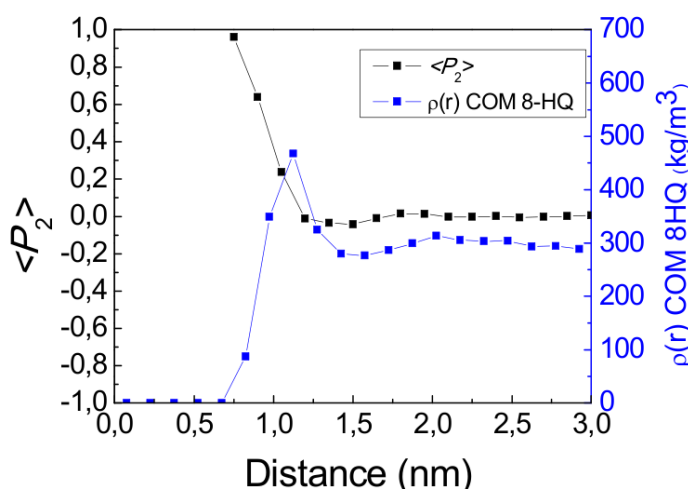


Figure 3.20: P_2 order parameter of the angle between the vectors $\hat{\mathbf{u}}_{\text{NP}}$ and $\hat{\mathbf{u}}_3$ (see Figure 3.19) as function of the distance between NP and 8-HQ centers of mass for the system containing a non-coated nanoparticle in the presence of 8-HQ. The blue curve shows the behavior of 8-HQ centre of mass radial density.

P_2 has been obtained calculating the second order Legendre polynomial

$$P_2 = \frac{1}{2}(3 \cos^2 \theta - 1) \quad (3.6)$$

Values of P_2 close to one indicate a predominance of parallel or antiparallel orientation of two vectors, values close to -0.5 indicate a predominance of perpendicular orientation. Random orientations give values of P_2 equal to zero. According to the definitions given above, from the plot of figure 11 it is clear that for distances between the nanoparticle and 8-HQ centre of mass lower than 1.2 nm the 8-HQ molecules are oriented with the molecular plane parallel to the nanoparticle surface. In figure 11 together with the P_2 the radial density of 8-HQ molecules is also reported. From the radial density behavior is clear that at short distances, where the orientation is stronger, the radial density is low. The nanoparticle radius is about 0.6 nm and this means that when the distance

between 8-HQ and nanoparticle centre of mass is about 0.6 the molecules are attached to the surface. According to this, the few molecules 8-HQ that are very close to the surface have a strong parallel orientation. This behavior is reasonable due to the excluded volume interactions between atoms of the gold surface and the atoms of the 8-HQ molecules. At distances where the radial density is larger at around 1 nm the parallel orientation is still present but less stronger. Finally, at distances larger than 1.2 the plot of figure 11 indicates a random orientation. In Figure 3.21 is depicted a snapshot of the simulated systems including a non-coated nanoparticle, where some of the 8-HQ molecules closest to the gold surface are shown. From Figure 3.21 it is clear the parallel

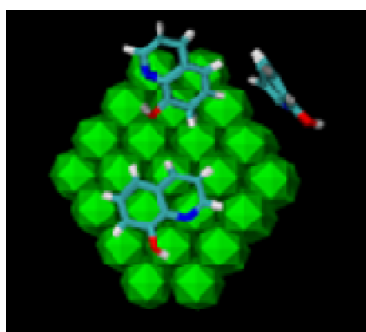


Figure 3.21: Snapshot of system 3, showing three 8-HQ molecules close to the nanoparticle surface. According to the analysis of orientation functions shown in Figure 3.20 the 8-HQ molecules orient the molecular plane parallel to the NP surface.

orientation of 8-HQ molecules with respect to the nanoparticle surface.

In Figure 3.22 is reported the averaged order parameter P_2 of the angle between the vectors $\hat{\mathbf{u}}_{\text{NP}}$ and $\hat{\mathbf{u}}_3$ as function of the distance for the system containing a coated nanoparticle in the presence of 8-HQ. At very short distances, between 0.6 and 0.7 nm from the nanoparticle centre of mass, the molecular plane is oriented parallel to the nanoparticle surface. In this case, as is possible to see from the plot of 8-HQ radial density, at these very short distances the 8-HQ radial density is practically zero. The region from 1.0 to about 1.5 nm away from the center of mass correspond to higher density of alkyl chains (*i.e.* the nanoparticle corona). In this region, as already noted in the previous section, the density of 8-HQ is relevant. The behavior of the average P_2 in this region is characterized by negative values ranging from -0.3 to zero at distances larger than 1.5 nm. This indicates a preference for the 8-HQ molecules penetrating inside the region with high density of alkyl chains to orient perpendicular to the gold surface. In Figure 3.23 is depicted a snapshot of the simulation of the system including a coated nanoparticle in presence of 8-HQ, in the figure have been reported some of the 8-HQ molecules closer to the nanoparticle surface.

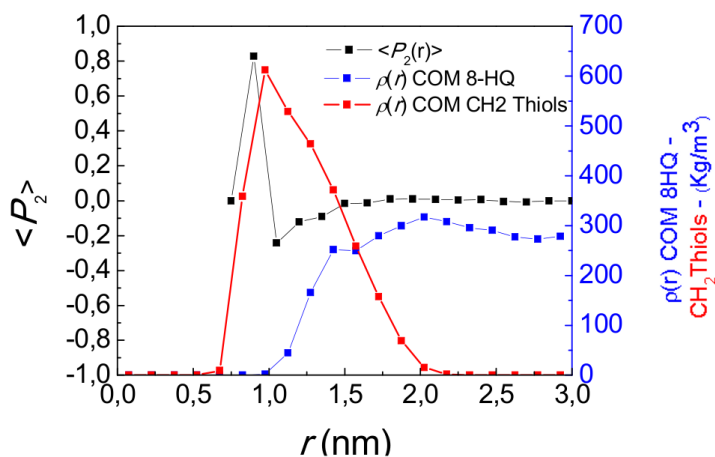


Figure 3.22: P_2 order parameter of the angle between the vectors \hat{u}_{NP} and \hat{u}_3 as function of the distance between NP and 8-HQ centers of mass for the system containing a coated nanoparticle in the presence of 8-HQ. The red curve shows the behavior of thiols carbon atoms density. The blue curve shows the behavior of 8-HQ centre of mass radial density.

From the picture it is clear the penetration of the 8-HQ molecules through the alkyl chain layer and their tendency to be perpendicular to the gold surfaces.

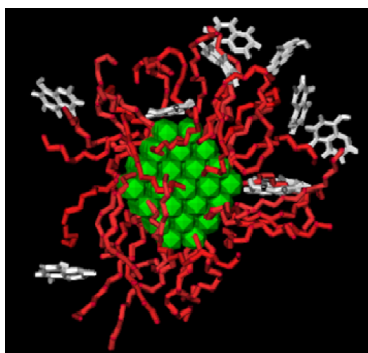


Figure 3.23: Snapshot of system 4, showing some 8-HQ molecules close to the coating layer. According to the analysis of orientation functions shown in Figure 3.22 the inner 8-HQ molecules have the tendency to orient the molecular plane perpendicular to the NP surface.

3.5 Summary

Using MD simulations interfaces between gold nanoparticle and PS melts have been fully characterized at atomistic level. Considering their relevance in the memory technology applications, systems containing gold nanoparticle included

in PS polymer melts also in presence of 8-HQ molecules have been studied. Four different systems have been compared. In order to understand the effects of nanoparticle coating on the interfaces structure, results obtained for systems including coated and non-coated gold nanoparticles in a PS melt have been compared. Furthermore, the effects of the presence of a third low molecular weight component (8-HQ) and its orientation with respect non-coated and coated gold nanoparticles have been considered. According to previous literature studies, calculated radial density profiles show that the presence of non-coated nanoparticles in a polymer melt causes an ordering of polymer chains. This effect is less pronounced but still present for PS chains in presence of the lower molecular weight 8-HQ third component. A similar ordering behavior is found for the 8-HQ molecule. In presence of a coated gold nanoparticle, calculated radial density profiles, show much less order for both PS chains and 8-HQ molecules with respect to systems including a non-coated nanoparticle. Atomic contributions to the radial density profiles reveal that, in both cases of non-coated and coated gold nanoparticles the PS chains expose the phenyl rings to the nanoparticle surface. In the case of coated nanoparticles there is some penetration of the PS phenyl rings into nanoparticle coating layer. When 8-HQ is present, this molecule is closer to the nanoparticle surface and when in contact with a coated nanoparticle shows a deeper penetration into the thiols layer. The orientation of 8-HQ results short range and parallel with respect to the surface of non-coated gold nanoparticles. Different is the 8-HQ orientation in the case of a coated gold nanoparticle. In this case the orientation results perpendicular to the nanoparticle surface.

Conclusions

In addition to the summary at the end each topic, the most important conclusions that can be drawn from this thesis are listed below:

- Reactivity Problem – Metathesis:
 - (a) The flexibility around the N–substituent bond is a key feature, so far underestimated, that allows NHCs to modulate their encumbrance around the metal in order to allow the coordination even for incoming bulky substrates. The Ru–complexes that have been investigated here are relevant as (pre)catalysts for olefin metathesis. However, it is reasonable that the emerged behavior can be easily extended to NHC ligands in almost any NHC–transition metal complex.
 - (b) The reduced electron density on the π MO of the methyldiene group, due to the presence of a π –acid ligand trans to it, allows for a favorable interaction with the π –aromatic system of the proximal mesityl group of the NHC ligand, which leads to metallacycle formation first and subsequently in the formation of a tensioned cyclopropane structure that finally evolves to the experimental product via a Buchner type ring expansion. The presented results clearly indicate that several π –acid groups can promote this deactivation route. However, this group must be able to approach the Ru center in the sterically protected coordination position trans to the Ru–methyldiene bond.
- Structure Problem – Metal/polymer interface: the calculated radial density profiles allowed to get atomistic insights in the Metal/polymer interface. In both cases of non–coated and coated gold nanoparticles the polystyrene chains expose the phenyl rings to the nanoparticle surface. In the case of coated nanoparticles there is some penetration of the polystyrene phenyl rings into nanoparticle coating layer. When it is present, the third organic component (8–hydroxyquinoline) is closer to the nanoparticle surface and when in contact with a coated nanoparticle shows a deeper penetration into the thiols layer. The orientation of 8–hydroxyquinoline results

short range and parallel with respect to the surface of non-coated gold nanoparticles. Different is the 8-hydroxyquinoline orientation in the case of a coated gold nanoparticle. In this case the orientation results perpendicular to the nanoparticle surface.

References

- [1] Alder, B. J. and Wainwright, T. E. *The Journal of Chemical Physics* **27**(5), 1208 (1957).
- [2] Alder, B. J. and Wainwright, T. E. *The Journal of Chemical Physics* **31**(2), 459–466 (1959).
- [3] Miyamoto, S. and Kollman, P. A. *Journal of Computational Chemistry* **13**(8), 952–962 (1992).
- [4] Ryckaert, J.-P., Ciccotti, G., and Berendsen, H. J. C. *Journal of Computational Physics* **23**(3), 327–341 (1977).
- [5] Hess, B., Bekker, H., Berendsen, H. J. C., and Fraaije, J. G. E. M. *Journal of Computational Chemistry* **18**(12), 1463–1472 (1997).
- [6] Verlet, L. **159**, 98 (1967).
- [7] Verlet, L. **165**(1), 201–214 (1968).
- [8] Feynman, R. P., Leighton, R. B., and Sands, M. *The Feynman Lectures on Physics*, volume 1. Vol. 1 edition, (1963).
- [9] Andersen, H. C. *The Journal of Chemical Physics* **72**(4), 2384 July (1980).
- [10] Marx, D. and Hutter, J. *Modern methods and algorithms of quantum chemistry*. Forschungszentrum Juelich, nic series edition, (2000).
- [11] Parr, R. G. and Yang, W. *Density-Functional Theory of Atoms and Molecules*. Oxford University Press, Oxford Oxfordshire, (1989).
- [12] Dreizler, R. M. and Gross, E. K. U. *Density Functional Theory*. Berlin: Springer, (1990).
- [13] Kohn, W. and Sham, L. J. November (1965).
- [14] Becke, A. D. September (1988).
- [15] Lee, C., Yang, W., and Parr, R. G. January (1988).
- [16] Perdew, J. and Wang, Y. June (1992).
- [17] Perdew, J. P., Burke, K., and Ernzerhof, M. *Physical Review Letters* **77**(18), 3865–3868 October (1996).
- [18] Handy, N. and Cohen, A. *Molecular Physics* **99**(5), 403–412 March (2001).
- [19] Cohen, A. and Handy, N. *Molecular Physics* **99**(7), 607–615 April (2001).
- [20] Handy, N. C. and Cohen, A. J. *The Journal of Chemical Physics* **116**(13), 5411 (2002).
- [21] Wu, Q. and Yang, W. *The Journal of Chemical Physics* **116**(2), 515 (2002).
- [22] Becke, A. D. *The Journal of Chemical Physics* **98**(7), 5648 (1993).
- [23] Becke, A. D. and Roussel, M. April (1989).
- [24] Becke, A. D. *The Journal of Chemical Physics* **112**(9), 4020 (2000).
- [25] Ernzerhof, M., Maximoff, S. N., and Scuseria, G. E. *The Journal of Chemical Physics* **116**(10), 3980 (2002).
- [26] Proynov, E., Chermette, H., and Salahub, D. R. *The Journal of Chemical Physics* **113**(22), 10013 (2000).

- [27] Liu, Z., Carter, L. E., and Carter, E. A. *The Journal of Physical Chemistry* **99**(13), 4355–4359 March (1995).
- [28] Vanderbilt, D. *Physical Review B* **41**(11), 7892–7895 April (1990).
- [29] Troullier, N. and Martins, J. L. *Physical Review B* **43**(3), 1993–2006 January (1991).
- [30] Bachelet, G., Hamann, D., and Schlüter, M. *Physical Review B* **26**(8), 4199–4228 October (1982).
- [31] Goedecker, S., Teter, M., and Hutter, J. *Physical Review B* **54**(3), 1703–1710 July (1996).
- [32] Blöchl, P. E. *Physical Review B* **50**(24), 17953–17979 December (1994).
- [33] Goedecker, S. *Reviews of Modern Physics* **71**(4), 1085–1123 July (1999).
- [34] Gerald Lippert, J. H. and Mic, B. *Molecular Physics* **92**(3), 477–488 October (1997).
- [35] Hartwigsen, C., Goedecker, S., and Hutter, J. *Physical Review B* **58**(7), 3641–3662 August (1998).
- [36] Carter, E. A., Ciccotti, G., Hynes, J., and Kapral, R. *Chemical Physics Letters* (1989).
- [37] Bash, P., Singh, U. C., Brown, F., Langridge, R., and Kollman, P. A. *Science* **235**(4788), 574–576 January (1987).
- [38] Patey, G. N. and Valleau, J. P. *The Journal of Chemical Physics* **63**(6), 2334 (1975).
- [39] Rosso, L., Minář, P., Zhu, Z., and Tuckerman, M. E. *The Journal of Chemical Physics* **116**(11), 4389 (2002).
- [40] Raiteri, P., Laio, A., Gervasio, F. L., Micheletti, C., and Parrinello, M. *The Journal of Physical Chemistry B* **110**(8), 3533–9 March (2006).
- [41] Ensing, B., De Vivo, M., Liu, Z., Moore, P., and Klein, M. L. *Accounts of chemical research* **39**(2), 73–81 (2006).
- [42] Barducci, A., Bonomi, M., and Parrinello, M. *Biophysical journal* **98**(9), L44–6 May (2010).
- [43] Spiwok, V., Lipovová, P., and Králová, B. *The Journal of Physical Chemistry B* **111**(12), 3073–3076 March (2007).
- [44] Gervasio, F. L. and Laio, A. *Reports on Progress in Physics* **71**(12), 126601 (2008).
- [45] Barducci, A., Bussi, G., and Parrinello, M. *Physical Review Letters* **100**(2), 1–4 (2008).
- [46] Bonomi, M. and Parrinello, M. *Comput. Chem* **30**, 7 October (2009).
- [47] Branduardi, D., Gervasio, F. L., and Parrinello, M. *The Journal of chemical physics* **126**(5), 054103 (2007).
- [48] Merlitz, H. and Wenzel, W. *Chemical Physics Letters* **362**(3-4), 271–277 August (2002).
- [49] Sugita, Y. and Okamoto, Y. *Chemical Physics Letters* **314**(1-2), 141–151 November (1999).
- [50] Nakajima, N., Higo, J., Kidera, A., and Nakamura, H. *Chemical Physics Letters* **278**(4-6), 297–301 October (1997).
- [51] Wang, F. and Landau, D. *Physical Review Letters* **86**(10), 2050–2053 March (2001).
- [52] Henkelman, G. and Jónsson, H. *The Journal of Chemical Physics* **113**(22), 9978 (2000).
- [53] E, W., Vanden-Eijnden, E., and Ren, W. *Physical Review B* **66**(5), 5–8 (2002).
- [54] E, W., Vanden-Eijnden, E., and Ren, W. *The Journal of chemical physics* **126**(16), 164103 (2007).
- [55] Maragliano, L., Fischer, A., Vanden-Eijnden, E., and Ciccotti, G. *The Journal of chemical physics* **125**(2), 24106 July (2006).
- [56] Bolhuis, P. G., Chandler, D., Dellago, C., and Geissler, P. L. *Annual review of physical chemistry* **53**, 291–318 (2002).
- [57] Woo, T. K. and Rowley, C. N. *The Journal of chemical physics* **126**(2), 024110 (2007).
- [58] Henkelman, G. and Jónsson, H. *The Journal of Chemical Physics* **111**(15), 7010 (1999).
- [59] Voter, A. *Physical Review Letters* **78**(20), 3908–3911 May (1997).

- [60] Trost, B. M. *Accounts of Chemical Research* **35**(9), 695–705 September (2002).
- [61] Poulsen, C. S. and Madsen, R. *Synthesis* (1), 0001–0018 (2003).
- [62] Diver, S. T. and Giessert, A. J. *Chemical reviews* **104**(3), 1317–82 March (2004).
- [63] Calderon, N. *Accounts of Chemical Research* **5**(4), 127–132 April (1972).
- [64] Calderon, N. *Tetrahedron Letters* **8**(34), 3327–3329 (1967).
- [65] Eleuterio, H. *Journal of Molecular Catalysis* **65**(1-2), 55–61 March (1991).
- [66] Polymerization, C. **143**(8), 3–6 (1960).
- [67] Banks, R. L. and Bailey, G. C. *Industrial & Engineering Chemistry Product Research and Development* **3**(3), 170–173 September (1964).
- [68] Fischer, E. O. and Maasböl, A. *Angewandte Chemie, International Edition in English* **3**(8), 580–581 August (1964).
- [69] Natta, G., Dall'Asta, G., and Mazzanti, G. *Angewandte Chemie, International Edition in English* **3**(11), 723–729 November (1964).
- [70] Casey, C. P. and Burkhardt, T. J. *Journal of the American Chemical Society* **96**(25), 7808–7809 December (1974).
- [71] Katz, T. J. and McGinnis, J. *Journal of the American Chemical Society* **97**(6), 1592–1594 March (1975).
- [72] Grubbs, R., Carr, D. D., Hoppin, C., and Burk, P. L. *Journal of the American Chemical Society* **98**(12), 3478–3483 June (1976).
- [73] Grubbs, R., Burk, P. L., and Carr, D. D. *Journal of the American Chemical Society* **97**(11), 3265–3267 May (1975).
- [74] Katz, T. J. *Angewandte Chemie, International Edition in English* **44**(20), 3010–9 May (2005).
- [75] Lee, S. J., McGinnis, J., and Katz, T. J. *Journal of the American Chemical Society* **98**(24), 7818–7819 November (1976).
- [76] Keim, W. *Chemie Ingenieur Technik* **66**(4), 548–548 April (1994).
- [77] Nelson, J. *Synthesis and Reactivity in Inorganic, Metal-Organic, and Nano-Metal Chemistry* **14**(7), 1047–1047 (1984).
- [78] Kubas, G. J. *Accounts of Chemical Research* **21**(3), 120–128 March (1988).
- [79] Huang, J., Stevens, E. D., Nolan, S. P., and Petersen, L. *Journal of the American Chemical Society* **121**(12), 2674 (1999).
- [80] Scholl, M. *Tetrahedron Letters* **40**(12), 2247–2250 March (1999).
- [81] Arduengo, A. J., Kline, M., Calabrese, J. C., and Davidson, F. *Journal of the American Chemical Society* **113**(25), 9704–9705 (1991).
- [82] Arduengo, A. J. *Accounts of Chemical Research* **32**(11), 913–921 November (1999).
- [83] Tebbe, F. N., Parshall, G. W., and Reddy, G. S. *Journal of the American Chemical Society* **100**(11), 3611–3613 May (1978).
- [84] Arduengo, A. J., Harlow, R. L., and Kline, M. *Journal of the American Chemical Society* **113**(1), 361–363 (1991).
- [85] Assen, E., Kantchev, B., O'Brien, C. J., and Organ, M. G. *Angewandte Chemie, International Edition in English* **46**(16), 2768–2813 (2007).
- [86] Miyaura, N. and Suzuki, A. *Chemical Reviews* **95**(7), 2457 (1995).
- [87] Marion, N. and Nolan, S. P. *Accounts of Chemical Research* **41**(11), 1440 (2008).
- [88] Würtz, S. and Glorius, F. *Accounts of Chemical Research* **41**(11), 1523 (2008).
- [89] Diez-Gonzalez, S., Marion, N., and Nolan, S. P. *Chemical Reviews* **109**(8), 3612 (2009).
- [90] Wolfgang, A. H., Lukas, J. G., Christian, K., and Georg, R. J. A. *Angewandte Chemie, International Edition in English* **35**, 2805 (1996).
- [91] Danopoulos, A. A., Pugh, D., and Wright, J. A. *Angewandte Chemie, International Edition in English* **47**(50), 9765–9767 (2008).

- [92] Hanasaka, F., Tanabe, Y., Fujita, K.-i., and Yamaguchi, R. *Organometallics* **25**(4), 826 (2006).
- [93] Lee, C. W. and Grubbs, R. *Journal of Organic Chemistry* **66**(21), 7155 (2001).
- [94] Powell, M. T., Hou, D.-R., Perry, M. C., Cui, X., and Burgess, K. *Journal of the American Chemical Society* **123**(36), 8878 (2001).
- [95] Nieto-Oberhuber, C., López, S., Jiménez-Núñez, E., and Echavarren, A. M. *Chem. Eur. J.* **12**, 5916–5923 (2006).
- [96] Añorbe, L., Domínguez, G., and Pérez-Castells, J. *Chem. Eur. J.* **10**, 4938–4943 (2004).
- [97] Laitar, D. S., Muller, P., and Sadighi, J. P. *Journal of the American Chemical Society* **127**(49), 17196 (2005).
- [98] Kleeberg, C., Dang, L., Lin, Z., and Marder, T. B. *Angewandte Chemie, International Edition in English* **48**(29), 5350–5354 (2009).
- [99] Keaton, R. J., Blacquiere, J. M., and Baker, R. T. *J. Am. Chem. Soc.* **129**, 1844 (2007).
- [100] Scholl, M., Ding, S., Lee, C. W., and Grubbs, R. *Organic Letters* **1**(6), 953–956 (1999).
- [101] Weskamp, T., Kohl, F. J., Hieringer, W., Gleich, D., and Herrmann, W. A. *Angewandte Chemie, International Edition in English* **38**, 2416 (1999).
- [102] Trnka, T. M. and Grubbs, R. *Accounts of Chemical Research* **34**(1), 18 (2000).
- [103] Fürstner, A. *Angewandte Chemie, International Edition in English* **39**, 3012 (2000).
- [104] Samojłowski, C., Bieniek, M., and Grela, K. *Chemical reviews* **109**(8), 3708–3742 August (2009).
- [105] Grubbs, R. *Handbook of Olefin Metathesis*. Wiley-VCH: Weinheim, Germany, (2003).
- [106] Rouhi, M. A. *Chemical & Engineering News* **80**, 29 (2002).
- [107] Rybak, A. and Meier, M. A. R. *Green Chem.* **9**, 1356–1361 (2007).
- [108] Malacea, R., Fischmeister, C., Bruneau, C., Dubois, J. L., Couturier, J. L., and Dixneuf, P. H. *Green Chem.* **11**, 152–155 (2009).
- [109] Tsantrizos, Y. S., Ferland, J.-M., McClory, A., Poirier, M., Farina, V., Yee, N. K., Wang, X.-j., Haddad, N., Wei, X., Xu, J., and Zhang, L. *Journal of Organometallic Chemistry* **691**(24-25), 5163 (2006).
- [110] Kanada, R. M., Itoh, D., Nagai, M., Nijima, J., Asai, N., Mizui, Y., Abe, S., and Kotake, Y. *Angewandte Chemie, International Edition in English* **46**(23), 4350–4355 (2007).
- [111] Wallace, D. J., Goodman, J. M., Kennedy, D. J., Davies, A. J., Cowden, C. J., Ashwood, M. S., Cottrell, I. F., Dolling, U.-H., and Reider, P. J. *Organic Letters* **3**(5), 671 (2001).
- [112] Dorta, R., Stevens, E. D., Scott, N. M., Costabile, C., Cavallo, L., Hoff, C. D., and Nolan, S. P. *Journal of the American Chemical Society* **127**(8), 2485–95 March (2005).
- [113] de Frémont, P., Scott, N. M., Stevens, E. D., Ramnial, T., Lightbody, O. C., Macdonald, C. L. B., Clyburne, J. A. C., Abernethy, C. D., and Nolan, S. P. *Organometallics* **24**(26), 6301–6309 (2005).
- [114] Fantasia, S., Petersen, L., Jacobsen, H., Cavallo, L., and Nolan, S. P. *Organometallics* **26**(24), 5880–5889 (2007).
- [115] Kelly, R. A., Clavier, H., Giudice, S., Scott, N. M., Stevens, E. D., Bordner, J., Samardjiev, I., Hoff, C. D., Cavallo, L., and Nolan, S. P. *Organometallics* **27**(2), 202–210 (2008).
- [116] Leuthäuser, S., Schmidts, V., Thiele, C. M., and Plenio, H. *Chemistry (Weinheim an der Bergstrasse, Germany)* **14**(18), 5465–5481 January (2008).
- [117] Frey, G. D., Rentzsch, C. F., von Preysing, D., Scherg, T., Muehlhofer, M., Herdtweck, E., and Herrmann, W. A. *J. Organomet. Chem.* **691**, 5725–5738 (2006).
- [118] Khramov, D. M., Lynch, V. M., and Bielawski, C. W. *Organometallics* **26**(24), 6042–6049 (2007).
- [119] Sanderson, M. D., Kamplain, J. W., and Bielawski, C. W. *Journal of the American Chemical Society* **128**(51), 16514–16515 (2006).
- [120] Hu, X. L., Castro-Rodriguez, I., Olsen, K., and Meyer, K. *Organometallics* **23**(4), 755–764 (2004).

- [121] Chianese, A. R., Kovacevic, A., Zeglis, B. M., Faller, J. W., and Crabtree, R. H. *Organometallics* **23**(10), 2461 (2004).
- [122] Chianese, A. R., Li, X., Janzen, M. C., Faller, J. W., and Crabtree, R. H. *Organometallics* **22**, 1663 (2003).
- [123] Poater, A., Cosenza, B., Correa, A., Giudice, S., Ragone, F., Scarano, V., and Cavallo, L. *European Journal of Inorganic Chemistry* **2009**(13), 1759–1766 May (2009).
- [124] Hillier, A. C., Sommer, W. J., Yong, B. S., Petersen, L., Cavallo, L., and Nolan, S. P. *Organometallics* **22**(21), 4322–4326 October (2003).
- [125] Viciu, M. S., Navarro, O., Germaneau, R. F., Kelly, R. A., Sommer, W. J., Marion, N., Stevens, E. D., Cavallo, L., and Nolan, S. P. *Organometallics* **23**(7), 1629–1635 March (2004).
- [126] Poater, A., Ragone, F., Giudice, S., Costabile, C., Dorta, R., Nolan, S. P., and Cavallo, L. *Organometallics* **27**(12), 2679–2681 June (2008).
- [127] Seiders, T. J., Ward, D. W., and Grubbs, R. *Organic letters* **3**(20), 3225–8 October (2001).
- [128] Funk, T. W., Berlin, J. M., and Grubbs, R. *Journal of the American Chemical Society* **128**(6), 1840–1846 (2006).
- [129] Costabile, C. and Cavallo, L. *Journal of the American Chemical Society* **126**(31), 9592–600 August (2004).
- [130] Vehlow, K., Gessler, S., and Blechert, S. *Angewandte Chemie, International Edition in English* **46**(42), 8082–8085 (2007).
- [131] Ritter, T., Day, M. W., and Grubbs, R. *Journal of the American Chemical Society* **128**(36), 11768–11769 (2006).
- [132] Stewart, J. J. P. *Journal of molecular modeling* **13**(12), 1173–213 (2007).
- [133] Stewart, I. C., Benitez, D., O’Leary, D. J., Tkatchouk, E., Day, M. W., Goddard III, W. A., and Grubbs, R. *Journal of the American Chemical Society* **131**(5), 1931–8 February (2009).
- [134] Cavallo, L., Correa, A., Costabile, C., and Jacobsen, H. *Journal of Organometallic Chemistry* **690**(24-25), 5407–5413 December (2005).
- [135] Clavier, H., Correa, A., Cavallo, L., Escudero-Adán, E. C., Benet-Buchholz, J., Slawin, A. M. Z., and Nolan, S. P. *European Journal of Inorganic Chemistry* **2009**(13), 1767–1773 May (2009).
- [136] Würtz, S., Lohre, C., Fröhlich, R., Bergander, K., and Glorius, F. *Journal of the American Chemical Society* **131**(24), 8344–5 June (2009).
- [137] Clavier, H. and Nolan, S. P. *Chemical communications (Cambridge, England)* **46**(6), 841–61 (2010).
- [138] Ragone, F., Poater, A., and Cavallo, L. *Journal of the American Chemical Society* **132**(12), 4249–58 March (2010).
- [139] Diebolt, O., Jurcik, V., Correa da Costa, R., Braunstein, P., Cavallo, L., Nolan, S. P., Slawin, A. M. Z., and Cazin, C. S. J. *Organometallics* (10), 100219145510007 (2010).
- [140] Frisch, M. J., Trucks, G. W., Schlegel, H. B., Scuseria, G. E., Robb, M. A., Cheeseman, J. R., Montgomery, J. A. J., Vreven, T., Kudin, K. N., Burant, J. C., Millam, J. M., Iyengar, S. S., Tomasi, J., Barone, V., Mennucci, B., Cossi, M., Scalmani, G., Rega, N., Petersson, G. A., Nakatsuji, H., Hada, M., Ehara, M., Toyota, K., Fukuda, R., Hasegawa, J., Ishida, M., Nakajima, T., Honda, Y., Kitao, O., Nakai, H., Klene, M., Li, X., Knox, J. E., Hratchian, H. P., Cross, J. B., Adamo, C., Jaramillo, J., Gomperts, R., Stratmann, R. E., Yazyev, O., Austin, A. J., Cammi, R., Pomelli, C., Ochterski, J. W., Ayala, P. Y., Morokuma, K., Voth, G. A., Salvador, P., Dannenberg, J. J., Zakrzewski, V. G., Dapprich, S., Daniels, A. D., Strain, M. C., Farkas, O., Malick, D. K., Rabuck, A. D., Raghavachari, K., Foresman, J. B., Ortiz, J. V., Cui, Q., Baboul, A. G., Clifford, S., Cioslowski, J., Stefanov, B. B., Liu, G., Liashenko, A., Piskorz, P., Komaromi, I., Martin, R. L., Fox, D. J., Keith, T., Al-Laham, M. A., Peng, C. Y., Nanayakkara, A., Challacombe, M., Gill, P. M. W., Johnson, B. G., Chen, W., Wong, M. W., Gonzalez, C., and Pople, J. A. (2003).
- [141] Perdew, J. P. *Phys. Rev. B* **34**, 7406 (1986).

- [142] Perdew, J. P., Burke, K., and Ernzerhof, M. *Phys. Rev. Lett.* **77**, 3865 (1996).
- [143] Schäfler, A., Horn, H., and Ahlrichs, R. *The Journal of Chemical Physics* **97**(4), 2571 (1992).
- [144] Haeusermann, U., Dolg, M., Stoll, H., and Preuss, H. *Mol. Phys.* **78**, 1211–1224 (1993).
- [145] Kuechle, W., Dolg, M., Stoll, H., and Preuss, H. *Journal of Chemical Physics* **100**, 7535 (1994).
- [146] Leininger, T., Nicklass, A., Stoll, H., Dolg, M., and Schwerdtfeger, P. *The Journal of Chemical Physics* **105**(3), 1052–1059 (1996).
- [147] Tomasi, J. and Persico, M. *Chemical Reviews* **94**, 2027 (1994).
- [148] Barone, V. and Cossi, M. *J. Phys. Chem. A* **102**, 1995 (1998).
- [149] VandeVondele, J., Krack, M., Mohamed, F., Parrinello, M., Chassaing, T., and Hutter, J. *Computer Physics Communications* **167**(2), 103–128 April (2005).
- [150] Perdew, J. P., Burke, K., and Wang, Y. *Phys. Rev. B* **54**, 16533 (1996).
- [151] Lippert, G., Hutter, J., and Parrinello, M. *Molecular Physics* **92**(3), 477–488 October (1997).
- [152] Cavallo, L., Correa, A., Costabile, C., and Jacobsen, H. *Journal of Organometallic Chemistry* **690**(24–25), 5407–5413 (2005).
- [153] Magill, A. M., Cavell, K. J., and Yates, B. F. *J. Am. Chem. Soc.* **126**, 8717 (2004).
- [154] Chung, C. K. and Grubbs, R. *Organic Letters* **10**(13), 2693 (2008).
- [155] Tolman, C. A. *Chemical Reviews* **77**(3), 313–348 (1977).
- [156] Galan, B. R., Gembicky, M., Dominiak, P. M., Keister, J. B., and Diver, S. T. *Journal of the American Chemical Society* **127**(45), 15702–3 November (2005).
- [157] Galan, B. R., Pitak, M., Gembicky, M., Keister, J. B., and Diver, S. T. *Journal of the American Chemical Society* **131**(19), 6822–32 May (2009).
- [158] Jazzar, R. F. R., Macgregor, S. A., Mahon, M. F., Richards, S. P., and Whittlesey, M. K. *Journal of the American Chemical Society* **124**(18), 4944–4945 (2002).
- [159] Giunta, D., Höllscher, M., Lehmann, C. W., Mynott, R., Wirtz, C., and Leitner, W. *Adv. Synth. Catal.* **345**, 1139 (2003).
- [160] Abdur-Rashid, K., Fedorkiw, T., Lough, A. J., and Morris, R. H. *Organometallics* **23**(1), 86–94 (2004).
- [161] Dorta, R., Kelly, R. A., and Nolan, S. P. *Advanced Synthesis & Catalysis* **346**(8), 917–920 (2004).
- [162] Scott, N. M., Dorta, R., Stevens, E. D., Correa, A., Cavallo, L., and Nolan, S. P. *Journal of the American Chemical Society* **127**(10), 3516–3526 (2005).
- [163] Hong, S. H., Day, M. W., and Grubbs, R. *Journal of the American Chemical Society* **126**(24), 7414–5 June (2004).
- [164] Ulman, M. and Grubbs, R. *Journal of Organic Chemistry* **64**(19), 7202 (1999).
- [165] Hong, S. H., Wenzel, A. G., Salguero, T. T., Day, M. W., and Grubbs, R. *J. Am. Chem. Soc.* **129**, 7961 (2007).
- [166] Monnier, F., Castillo, D., Derien, S., Toupet, L., and Dixneuf, P. H. *Angewandte Chemie, International Edition in English* **42**, 5474 (2003).
- [167] Peppers, B. P. and Diver, S. T. *Journal of the American Chemical Society* **126**(31), 9524 (2004).
- [168] Kitamura, T., Sato, Y., and Mori, M. *Chem. Comm.* , 1258 (2001).
- [169] Nishiyama, H., Itoh, Y., Matsumoto, H., Park, S.-B., and Itoh, K. *J. Am. Chem. Soc.* **116**, 2223 (1994).
- [170] Anciaux, A. J., Demonceau, A., Noels, A. F., Hubert, A. J., Warin, R., and Teyssie, P. *J. Org. Chem.* **46**, 873 (1981).
- [171] Basato, M., Tubaro, C., Biffis, A., Bonato, M., Buscemi, G., Lighezzolo, F., Lunardi, P., Vianini, C., Benetollo, F., and Del Zotto, A. *Chem. & Eur. J.* **15**, 1516 (2009).

- [172] Adlhart, C., Hinderling, C., Baumann, H., and Chen, P. *Journal of the American Chemical Society* **122**(34), 8204–8214 (2000).
- [173] Webster, C. E. *Journal of the American Chemical Society* **129**(24), 7490 (2007).
- [174] Bieniek, M., Koloda, D., and Grela, K. *Organic Letters* **8**(25), 5689 (2006).
- [175] Sanford, M. S., Ulman, M., and Grubbs, R. *Journal of the American Chemical Society* **123**(4), 749–50 January (2001).
- [176] Kuhne, T. D., Krack, M., Mohamed, F. R., and Parrinello, M. *Phys. Rev. Lett.* **98**, 66401 (2007).
- [177] Car, R. and Parrinello, M. *Phys. Rev. Lett.* **55**, 2471 (1985).
- [178] Parr, R. G., von Szentpaly, L., and Liu, S. *J. Am. Chem. Soc.* **121**, 1922 (1999).
- [179] Geerlings, P., De Proft, F., and Langenaeker, W. *Chem. Rev.* **103**, 1793 (2003).
- [180] Parr, R. G., Donnelly, R. A., Levy, M., and Palke, W. E. *J. Chem. Phys.* **68**, 3801 (1978).
- [181] Parr, R. G. and Pearson, R. G. *J. Am. Chem. Soc.* **105**, 7512 (1983).
- [182] Parr, R. G. and Yang, W. *Density Functional Theory of Atoms and Molecules*. (1989).
- [183] Koopmans, T. *Physica* **1**, 104 (1934).
- [184] Mayer, I. *Chemical Physics Letters* **97**, 270 (1983).
- [185] Mayer, I. *International Journal of Quantum Chemistry* **26**, 151–154 (1984).
- [186] Bridgeman, A. J. *J. Chem. Soc., Dalton Trans.* , 2601 (1996).
- [187] Bridgeman, A. J. *J. Chem. Soc., Dalton Trans.* , 4765 (1997).
- [188] Bridgeman, A. J. *Polyhedron* **17**, 2279 (1998).
- [189] Bridgeman, A. J., Cavigliasso, G., Ireland, L. R., and Rothery, J. *J. Chem. Soc., Dalton Trans.* , 2095 (2001).
- [190] Bridgeman, A. J., Harris, N., and Young, N. A. *Chem. Comm.* , 1241 (2000).
- [191] Bridgeman, A. J. and Nielsen, N. A. *Inorganica Chimica Acta* **303**, 107 (2000).
- [192] Bridgeman, A. J. and Rothery, J. *J. Chem. Soc., Dalton Trans.* , 4077 (1999).
- [193] Bridgeman, A. J. and Rothery, J. *Inorganica Chimica Acta* **288**, 17 (1999).
- [194] Kruszewski, J. and Krygowski, T. M. *Tetrahedron Letters* , 3839 (1972).
- [195] Krassowski, D. W., Nelson, J. H., Broer, K. R., Hauenstein, D., and Jacobson, R. A. *Inorganic chemistry* **27**, 4294–4307 (1988).
- [196] Barnard, C. F. J., Daniels, J. A., Jeffrey, J., and Mawby, R. J. *J. Chem. Soc., Dalton Trans.* , 953 (1976).
- [197] Costas, M., Ribas, X., Poater, A., LoÌApez-Valbuena, J. M., Xifra, R., Company, A., Duran, M., SolaÌA, M., Llobet, A., Corbella, M., UsolA, M. A., Mahia, J., Solans, X., Shan, X. P., and Benet-Buchholz, J. *Inorganic chemistry* **45**, 3569 (2006).
- [198] Jaque, P. and Toro-LabbelA, A. *J. Chem. Phys.* **117**, 3208 (2002).
- [199] Frenking, G., Solà, M., and Vyboishchikov, S. F. *Journal of Organometallic Chemistry* **690**(24-25), 6178–6204 (2005).
- [200] Tang, C. W. and VanSlyke, S. A. *Applied Physics Letters* **51**(12), 913 (1987).
- [201] Burroughes, J. H., Bradley, D. D. C., Brown, A. R., Marks, R. N., Mackay, K., Friend, R. H., Burns, P. L., and Holmes, A. B. *Nature* **347**(6293), 539–541 October (1990).
- [202] Sariciftci, N. S., Smilowitz, L., Heeger, A. J., and Wudl, F. *Science (New York, N.Y.)* **258**(5087), 1474–6 November (1992).
- [203] Dimitrakopoulos, C. D. and Mascaro, D. J. *IBM Journal of Research and Development* **45**(1), 11–27 January (2001).
- [204] Bozano, L. D., Kean, B. W., Deline, V. R., Salem, J. R., and Scott, J. C. *Applied Physics Letters* **84**(4), 607 (2004).
- [205] Varahramyan, K. *IEEE Electron Device Letters* **27**(3), 151–153 March (2006).

- [206] Ouyang, J., Chu, C.-W., Szmanda, C. R., Ma, L., and Yang, Y. *Nature materials* **3**(12), 918–22 December (2004).
- [207] Möller, S., Perlov, C., Jackson, W., Taussig, C., and Forrest, S. R. *Nature* **426**(6963), 166–9 November (2003).
- [208] Koo. (2006).
- [209] Lee, S. W., Mao, C., Flynn, C. E., and Belcher, A. M. *Science* **296**(5569), 892 (2002).
- [210] Borodin, O., Smith, G., Bandyopadhyaya, R., and O. *Macromolecules* **36**(20), 7873–7883 (2003).
- [211] Tseng, R.-H., Baker, C., Shedd, B., and Huang, J. *Applied Physics* **90**(5) (2009).
- [212] Collier, C. P., Wong, E. W., Belohradsky, M., Raymo, F. M., Stoddart, J. F., Kuekes, P. J., Williams, R. S., and Heath, J. R. *Science* **285**(5426), 391 (1999).
- [213] Cai, L., Cabassi, M. A., Yoon, H., Cabarcos, O. M., McGuinness, C. L., Flatt, A. K., Allara, D. L., Tour, J. M., and Mayer, T. S. *Nano Lett* **5**(12), 2365–2372 (2005).
- [214] Chu, C.-W., Ouyang, J., Tseng, R.-H., and Yang, Y. *Advanced Materials* **17**(11), 1440–+ (2005).
- [215] Ling, Q., Song, Y., Ding, S. J., Zhu, C., Chan, D. S. H., Kwong, D. L., Kang, E. T., and Neoh, K. G. *Advanced Materials* **17**(4), 455–459 (2005).
- [216] Tseng, R.-H., Huang, J., Ouyang, J., Kaner, R., and Yang, Y. *Nano Lett* **5**(6), 1077–1080 (2005).
- [217] Daniel, M.-C. and Astruc, D. *Chemical reviews* **104**(1), 293–346 (2004).
- [218] Yang, Y., Ouyang, J., Ma, L., Tseng, R.-H., and Chu, C.-W. *Advanced Functional Materials* **16**(8), 1001–1014 May (2006).
- [219] Billinge, S. J. L. and Levin, I. *Science* **316**(5824), 561 April (2007).
- [220] Jadzinsky, P. D., Calero, G., Ackerson, C. J., Bushnell, D. A., and Kornberg, R. D. *Science (New York, N.Y.)* **318**(5849), 430–3 October (2007).
- [221] Li, G., Huang, X., and Zhang, L. *Journal of the American Chemical Society* **130**(22), 6944–5 (2008).
- [222] Baschnagel, J., Binder, K., Doruker, P., Gusev, A., Hahn, O., Kremer, K., Mattice, W., Müller-Plathe, F., Murat, M., and Paul, W. *Viscoelasticity, atomistic models, statistical chemistry* **152**, 41–156 (2000).
- [223] Müller-Plathe, F. *ChemPhysChem* **3**(9), 754–769 September (2002).
- [224] Theodorou, D. *Chemical Engineering Science* **62**(21), 5697–5714 (2007).
- [225] Vacatello, M. *Macromolecules* **34**(6), 1946–1952 (2001).
- [226] Starr, F., Schrø der, T., and Glotzer, S. C. *Physical Review E* **6402**(2) (2001).
- [227] Starr, F., Schrø der, T., and Glotzer, S. C. *Macromolecules* **35**(11), 4481–4492 (2002).
- [228] Smith, G., Bedrov, D., Li, L., and Bytner, O. *The Journal of Chemical Physics* **117**(20), 9478–9489 (2002).
- [229] Starr, F. W., Douglas, J. F., and Glotzer, S. C. *The Journal of Chemical Physics* **119**(3), 1777–1788 (2003).
- [230] Kairn, T., Davis, P., Ivanov, I., and Bhattacharya, S. *The Journal of chemical physics* **123**(19), 194905 (2005).
- [231] Desai, T., Koblinski, P., and Kumar, S. K. *The Journal of chemical physics* **122**(13), 134910 (2005).
- [232] Sen, S., Thomin, J. D., Kumar, S. K., and Koblinski, P. *Macromolecules* **40**(11), 4059–4067 (2007).
- [233] Vacatello, M. *Macromolecules* **35**(21), 8191–8193 (2002).
- [234] Vacatello, M. *Macromolecular Theory and Simulations* **11**(7), 757–765 (2002).
- [235] Vacatello, M. *Macromolecular Theory and Simulations* **11**(1), 53–57 (2002).
- [236] Vacatello, M. *Macromolecules* **36**(9), 3411–3416 (2003).
- [237] Zhang, Q. and Archer, L. A. *The Journal of chemical physics* **121**(21), 10814–10824 (2004).

- [238] Papakonstantopoulos, G. J., Yoshimoto, K., and Doxastakis, M. *Physical Review E* **72**(3) (2005).
- [239] Allegra, G., Raos, G., and Vacatello, M. *Progress in Polymer Science* **33**(7), 683–731 July (2008).
- [240] Brown, D., Mele, P., Marceau, S., and Alberola, N. D. *Macromolecules* **36**(4), 1395–1406 (2003).
- [241] Barbier, D., Brown, D., Grillet, A., and Neyertz, S. *Macromolecules* **37**(12), 4695–4710 (2004).
- [242] Prout, C. K. and Wheeler, A. G. *Journal of the Chemical Society A: Inorganic, Physical, Theoretical*, 469 (1967).
- [243] Adams, D. M., Brus, L., Chidsey, C. E. D., Creager, S., Creutz, C., Kagan, C. R., Kamat, P. V., Lieberman, M., Lindsay, S., Marcus, R. a., Metzger, R. M., Michel-Beyerle, M. E., Miller, J. R., Newton, M. D., Rolison, D. R., Sankey, O., Schanze, K. S., Yardley, J., and Zhu, X. *The Journal of Physical Chemistry B* **107**(28), 6668–6697 July (2003).
- [244] Ipe, B. I., Thomas, K. G., Barazzouk, S., Hotchandani, S., and Kamat, P. V. *The Journal of Physical Chemistry B* **106**(1), 18–21 January (2002).
- [245] Castellano, E. and Prout, C. K. *Journal of the Chemical Society A: Inorganic, Physical, Theoretical*, 550 (1971).
- [246] Mo, X. *Thin Solid Films* **436**(2), 259–263 July (2003).
- [247] Oyamada, T., Tanaka, H., Matsushige, K., Sasabe, H., and Adachi, C. *Applied Physics Letters* **83**(6), 1252 (2003).
- [248] Milano, G. and Müller-Plathe, F. *The Journal of Physical Chemistry B* **109**(39), 18609–19 October (2005).
- [249] Santangelo, G., Di Matteo, A., Müller-Plathe, F., and Milano, G. *The Journal of Physical Chemistry B* **111**(11), 2765–73 March (2007).
- [250] Haliloglu, T. and Mattice, W. L. *The Journal of Chemical Physics* **108**(16), 6989 (1998).
- [251] Cho, J. and Mattice, W. L. *Macromolecules* **30**(3), 637–644 February (1997).
- [252] Rapold, R. F. and Mattice, W. L. *Journal of the Chemical Society, Faraday Transactions* **91**(16), 2435 (1995).
- [253] Baschnagel, J., Binder, K., Paul, W., Laso, M., Suter, U. W., Batoulis, I., Jilge, W., and Bultrger, T. (1991).
- [254] Paul, W., Binder, K., Kremer, K., and Heermann, D. W. *Macromolecules* **24**(23), 6332–6334 November (1991).
- [255] Carmesin, I. and Kremer, K. *Macromolecules* **21**(9), 2819–2823 September (1988).
- [256] Queyroy, S., Neyertz, S., Brown, D., and Müller-Plathe, F. *Macromolecules* **37**(19), 7338–7350 September (2004).
- [257] Faller, R., Kolb, A., and Müller-Plathe, F. *Physical Chemistry Chemical Physics* **1**(9), 2071–2076 (1999).
- [258] Faller, R., Müller-Plathe, F., and Heuer, A. *Macromolecules* **33**(17), 6602–6610 August (2000).
- [259] Faller, R., Müller-Plathe, F., Doxastakis, M., and Theodorou, D. *Macromolecules* **34**(5), 1436–1448 February (2001).
- [260] Sun, Q. and Faller, R. *Macromolecules* **39**(2), 812–820 January (2006).
- [261] Sun, Q. and Faller, R. *Journal of Chemical Theory and Computation* **2**(3), 607–615 May (2006).
- [262] Harmandaris, V. a., Adhikari, N. P., van der Vegt, N. F. a., and Kremer, K. *Macromolecules* **39**(19), 6708–6719 September (2006).
- [263] Milano, G., Goudeau, S., and Müller-Plathe, F. *Journal of Polymer Science Part B: Polymer Physics* **43**(8), 871–885 April (2005).
- [264] Reith, D., Pütz, M., and Müller-Plathe, F. *Journal of computational chemistry* **24**(13), 1624–36 October (2003).

- [265] Lesk, A. M. *Acta Crystallographica Section A Foundations of Crystallography* **42**(2), 110–113 March (1986).
- [266] KenKnight, C. E. *Acta Crystallographica Section A Foundations of Crystallography* **40**(6), 708–712 November (1984).
- [267] Honzatko, R. B. *Acta Crystallographica Section A Foundations of Crystallography* **42**(3), 172–178 May (1986).
- [268] Kearsley, S. K. *Acta Crystallographica Section A Foundations of Crystallography* **45**(2), 208–210 February (1989).
- [269] Chen, X., Carbone, P., Cavalcanti, W., Milano, G., and Müller-Plathe, F. *Macromolecules* **40**(22), 8087–8095 (2007).
- [270] Spyriouni, T., Tzoumanekas, C., Theodorou, D., Müller-Plathe, F., and Milano, G. *Macromolecules* **40**(10), 3876–3885 (2007).
- [271] Tzoumanekas, C. and Theodorou, D. *Macromolecules* **39**(13), 4592–4604 (2006).
- [272] Berendsen, H. J. C. *Computer Physics Communications* **91**(1-3), 43–56 September (1995).
- [273] Müller-Plathe, F. *Macromolecules* **29**(13), 4782–4791 January (1996).
- [274] Witt, R., Sturz, L., Dölle, A., and Müller-Plathe, F. *The Journal of Physical Chemistry A* **104**(24), 5716–5725 June (2000).
- [275] Schmitz, H. and Müller-Plathe, F. *The Journal of Chemical Physics* **112**(2), 1040 (2000).
- [276] Milano, G., Guerra, G., and Müller-Plathe, F. *Chemistry of Materials* **14**(7), 2977–2982 July (2002).
- [277] Hostetler, M. J., Wingate, J. E., Zhong, C.-J., Harris, J. E., Vachet, R. W., Clark, M. R., Londono, J. D., Green, S. J., Stokes, J. J., Wignall, G. D., Glish, G. L., Porter, M. D., Evans, N. D., and Murray, R. W. *Langmuir* **14**(1), 17–30 January (1998).
- [278] Rai, B., Sathish, P., Malhotra, C. P., Pradip, and Ayappa, K. G. *Langmuir : the ACS journal of surfaces and colloids* **20**(8), 3138–44 April (2004).
- [279] Jorgensen, W. L., Maxwell, D. S., and Tirado-Rives, J. *Journal of the American Chemical Society* **118**(45), 11225–11236 January (1996).
- [280] Smith, J., Bedrov, D., and Smith, G. *Composites Science and Technology* **63**(11), 1599–1605 (2003).